Josephson Junctions with Ferromagnetic Alloy Interlayer

Dissertation

zur Erlangung des Doktorgrades (Dr. rer. nat.)

der Technischen Fakultät

der Christian-Albrechts-Universität zu Kiel

vorgelegt von

Nico Himmel, geb. Ruppelt

aus Neustadt am Rbge.

Kiel

2015

Erster Gutachter:	Prof. Dr. Hermann Kohlstedt
Zweiter Gutachter:	Prof. Dr. Franz Faupel
Mündliche Prüfung:	Kiel, 23. Juli 2015

Abstract

Josephson junctions are used as active devices in superconducting electronics and quantum information technology. Outstanding properties are their distinct non-linear electrical characteristics and a usually sinusoidal relation between the current and the superconducting phase difference across the junction. In general, the insertion of ferromagnetic material in the barrier of a Josephson junction is associated with a suppression of superconducting correlations. But also new phenomena can arise which may allow new circuit layouts and enhance the performance of applications.

This thesis presents a systematic investigation for two concepts to fabricate Josephson junctions with a rather uncommon negative critical current. Such devices exhibit an intrinsic phase slip of π between the electrodes, so they are also known as π junctions. Both studies go well beyond existing experiments and in one system a π junction is shown for the first time. All the thin film junctions are based on superconducting Nb electrodes. In a first approach, barriers made from Si and Fe were investigated with respect to the realisation of π junctions by spin-flip processes. The distribution of Fe in the Si matrix was varied from pure layers to disperse compounds. The systematic fabrication of alloy barriers was facilitated by the development of a novel timing-based combinatorial sputtering technique for planetary deposition systems. An orthogonal gradient approach allowed to create binary layer libraries with independent variations of thickness and composition. Second, $\mathrm{Nb}\,|\,\mathrm{AlO_x}\,|\,\mathrm{Nb}\,|\,\mathrm{Ni_{60}Cu_{40}}\,|\,\mathrm{Nb}$ (SIsFS) double barrier junctions were experimentally studied for the occurrence of proximity effect induced order parameter oscillations. Detailed dependencies of the critical current density on the thickness of s-layer and F-layer were acquired and show a remarkable agreement to existing theoretical predictions. Especially a variation of j_c and $I_\mathrm{c}R_\mathrm{N}$ by the s-layer thickness up to the value of nonmagnetic SIS junctions is notable. Additionally information on the

emergence of superconductivity with the s-layer thickness was acquired.

The introduction of this thesis (Chapter 1) is intended to motivate the experimental efforts and put them into the research context. An account on the evolving field of quantum information processing shall highlight the relevance of performance enhancements of superconducting devices. The chapter also introduces the theories of electron tunneling and effects at Josephson barriers, which are essential to analyse the experimental data. Moreover a description of magnetism along with mechanisms and experiments related to π Josephson junctions are presented.

In the following (Chapter 2) an overview about machines and processes for the fabrication and characterisation of thin film devices is given. The preparation of samples was performed at facilities of the Technical Faculty of the University of Kiel. Also information about the experimental setup are given. A focus is put on the deposition of layers with thickness gradients across the wafer and combinatorial sputtering to achieve independent variations of two layer parameters.

Finally (Chapter 3) experimental data for different types of Josephson junctions are shown. Related theories, relevant publications and a discussion are introduced along with the data.

Zusammenfassung

Josephson Kontakte werden als aktive Bauelemente in supraleitender Elektronikschaltungen und in ersten Versuchen zur Quanten-Informationsverarbeitung eingesetzt. Besondere Eigenschaften sind hierbei ihre hochgradig nicht lineare elektrische Charakteristik und eine meist sinusförmige Beziehung zwischen dem Strom und der Supraleitenden Phasendifferenz über dem Kontakt. Allgemein führt das Einbringen eines Ferromagneten in die Barriere eines Josephson Kontakts zu einer Reduktion der supraleitenden Korrelationen. Allerdings können dadurch auch neue Effekte auftreten, die neue Schaltkreislayouts ermöglichen oder die Leistungsfähigkeiten von Anwendungen erhöhen könnten.

In dieser Thesis werden zwei Ansätze, um Josephson Kontakte mit einem ungewöhnlichen negativen kritischen Strom herzustellen, systematisch untersucht. Diese Bauteile zeichnen sich durch einen intrinsischen Phasensprung von π zwischen den Elektroden aus, daher sind sie auch als π-Kontakte bekannt. Beide Untersuchungen gehen deutlich über bestehende Experimente hinaus und in einem System wurde zum ersten Mal ein π-Kontakt nachgewiesen. Sämtliche Dünnschichtkontakte basieren auf supraleitenden Nb Elektroden. In einem ersten Ansatz wurden Barrieren aus Si und Fe hergestellt und im Hinblick auf das Auftreten von π-Kontakten durch Spin-Flip Prozesse untersucht. Dabei wurde die Verteilung von Fe in einer Si Matrix von reinen Schichten bis zu homogen gemischten Verbindungen variiert. Um die systematische Herstellung von Barrieren aus Legierungen zu erleichtern, wurde eine neuen Zeit-basierte kombinatorische Sputtertechnik für Planetenartige Depositionssysteme entwickelt. Ein orthogonales Gradienten Verfahren ermöglichte die Herstellung von binären Schicht-Bibliotheken in denen die Schichtstärke und -zusammensetzung unabhängig voneinander variiert. In einem zweiten Ansatz wurden $\mathrm{Nb}\,|\,\mathrm{AlO_x}\,|\,\mathrm{Nb}\,|\,\mathrm{Ni_{60}Cu_{40}}\,|\,\mathrm{Nb}$ (SIsFS) Doppel-Barrieren-Kontakte experimentell im Hinblick auf Proximityeffekt bedingte Ordnungsparameter-Oszillationen untersucht. Fein aufgelöste

Abhängigkeiten der kritischen Stromdichte vom der Dicke der s-Schicht und F-Schicht wurden aufgenommen und Sie zeigen eine nennenswerte Übereinstimmung zu bestehenden theoretischen Vorhersagen. Besonders die Variation von j_c und $I_c R_N$ bedingt durch die s-Schicht Dicke, bis hin zu den Werten für nichtmagnetische SIS Kontakte, ist bemerkenswert. Zusätzlich wurden Informationen über das Erscheinen der Supraleitung mit der s-Schicht Dicke gewonnen.

Die Einleitung dieser Thesis (Chapter 1) soll die Bedeutung der experimentellen Arbeiten aufzeigen und eine Einordnung ins wissenschaftliche Umfeld vornehmen. Die Abhandlung über den aufkommenden Forschungsbereich der Quanten-Informationsverarbeitung soll die aktuelle Bedeutung von Leistungssteigerungen von supraleitenden Bauteilen hervorheben. Weiterhin werden in diesem Kapitel die grundlegenden Theorien zum Elektronentunneln und Effekten an Josephson Kontakten eingeführt, soweit sie für die Auswertung der experimentellen Daten nötig sind. Außerdem werden eine Beschreibung von Magnetismus und Mechanismen und Experimenten im Zusammenhang mit π Kontakten präsentiert.

Im nachfolgenden Kapitel (Chapter 2) wird ein Überblick zu den Geräten und Prozessen für die Herstellung und Vermessung von Dünnschicht-Bauelementen vermittelt. Die Herstellung von Proben erfolgte in den Einrichtungen der Technischen Fakultät der Christian-Albrechts-Universität zu Kiel. Darüber hinaus wird der experimentelle Messaufbau vorgestellt. Ein Fokus des Kapitels liegt bei der Lagenabscheidung mit Dickegradienten entlang des Wafers und kombinatorischem Sputtern mit der unabhängigen Variation von zwei Schichtparametern.

Zuletzt (Chapter 3) werden experimentelle Daten zu den verschiedenen Typen von Josephson Kontakten gezeigt. Spezielle Theorien, maßgebliche Publikationen und die Auswertung werden zusammen mit den Messdaten eingeführt.

List of Publications

Two paper about the experiments in this thesis have been published in peer reviewed journals. A third manuscript has been submitted. My contributions are specified below the reference. A complete list of publications can be found in the CV in the back-matter of this thesis.

Publication I

N. Ruppelt, H. Sickinger, R. Menditto, E. Goldobin, D. Koelle, R. Kleiner, O. Vavra, und H. Kohlstedt. "Observation of 0–π transition in SIsFS Josephson junctions", Appl. Phys. Lett. **106**, 022602 (2015).

I fabricated all the Josephson junctions and calibration samples. I also acquired the vast majority of the experimental data and performed the evaluations. Finally I prepared the first draft of the manuscript and supervised the revision process.

Publication II

N. Ruppelt, O. Vavra, H. Sickinger, E. Goldobin, D. Koelle, R. Kleiner, und H. Kohlstedt, "Combinatorial sputtering in planetary type systems for alloy libraries with perpendicular gradients of layer thickness and composition realised by a timing approach", Appl. Phys. A **116**, 229–232 (2014).

I fabricated all the Josephson junctions and calibration samples. I also acquired the experimental data, performed the evaluations and conducted the numerical simulations. Finally I also prepared the first draft of the manuscript and supervised the revision process.

Manuscript

D. M. Heim, N. G. Pugach, M. Y. Kupriyanov, E. Goldobin, D. Koelle, R. Kleiner, N. Ruppelt, M. Weides, und H. Kohlstedt, "The effect of normal metal layers in ferromagnetic Josephson junctions", arXiv:1310.0567v2 [cond-mat.supr-con] (2014).
(submitted to New Journal of Physics)

I supplied experimental data and comments which supports the claims of the manuscript. The data is shown in a graph and commented in the text.

Contents

1 Introduction

The discovery of a promising physical phenomenon usually triggers a lot of effort not only to understand the underlying mechanisms but also to exploit it in technology. Since 50 years ago the superconducting phase, that can occur in materials at low temperatures, is an intensively studied quantum phenomenon. Macroscopically superconductivity manifests as a dissipation free current, which is used for slim high power transmission lines and magnetic field coils. The discovery of Josephson junctions as structures with highly interesting electric and magnetic properties launched the development of a series of applications with unmatched performance in their respective field. The quantum mechanical correlations allowed to built extremely sensitive magnetic field sensors, signal processing devices for astronomy applications and super fast logic circuits. The need for cooling inspired researchers to find materials with higher temperatures T_c of the superconducting phase transition. It turned out however that the significant increase of T_c was accompanied with a severely impeded technological handling which drastically limited the applicability of the new materials. In the last decades quantum systems were evaluated and refined to serve as basis for novel computation algorithms, like simulators of complex systems and for secure communication. Superconducting solid state systems based on superconducting circuits are considered as promising candidates for coupled and integrated quantum systems.

The order arising in conventional superconducting systems contradicts with ferromagnetic order. However, the combination of both can result in interesting physics. One effect is the occurrence of π Josephson junctions, e.g. devices with an intrinsic phase slip of π, which not only offer exciting science but could also enhance existing technology. Given a certain performance they could serve as missing elements for complementary superconducting logic [1] and facilitate the design of quantum bits [2–4]. In contrast to non-magnetic junctions however, most

Josephson junctions with ferromagnetic material in the barrier either have a considerably reduced critical current density j_c or a tiny normal resistance of the barrier. The controlled enhancement of both quantities was the fundamental motivation for experiments in this thesis.

Another application of Josephson junctions are superconducting single flux quantum circuits which achieve clock frequencies of several 100 GHz while the dissipated energy of the circuits is not larger than some mW. The operation of superconducting circuitry is based on the current/flux and the superconducting phase. A compact and versatile phase shifting component would complete the set of basic circuit elements. In analogy to conventional Si electronics a complementary circuit design would lead to enhanced operation parameters and reliability [5–8]. Magnetic Josephson junctions could also serve as integrated, non-volatile superconducting memory devices [9, 10]. Besides the technological compatibility in the fabrication process the device performance is essential for its operation in a circuitry. The RSFQ operation frequency corresponds to the Josephson junction switching time [9, 11, 12]

$$\tau = \frac{\Phi_0}{2\pi I_c R_N} \tag{1.1}$$

with the flux quantum Φ_0. In order to be employed as fast active elements the Josephson junctions need to exhibit a small τ and therefore a maximized $I_c R_N$ product.

The accounts in this chapter are intended to motivate and explain the experimental works that were performed in the frame of this thesis. After a summary about quantum information processing a basic description of superconductivity and the tunneling effect are presented. Then the Josephson effect of superconducting junctions and the influence of ferromagnetic material in the barrier are explained to an extent which is relevant to understand the behaviour of devices. Remarks on the charge transport concentrate on the possible discrimination of different mechanisms in experimental data. Comprehensive and detailed descriptions about Josephson junctions can be found in literature [13–15] which also inspired parts of the following sections.

1.1 Quantum Information Processing

The basic principles of electrical data processing haven't changed since their advent in the early 20^{th} century. The main driving force to enhance computing power has been the miniaturization of semiconducting devices [16]. Although highly advanced, classical transistors made from semiconducting material still serve as the main active elements to process binary data. Novel strategies and concepts promise superior performance in specialized applications or could possibly unlock completely new fields that will not be accessible with today's technology [17]. One example are bio-inspired architectures which could allow to create adaptive electronics for recognition and learning applications [18]. Essential in this field is the development of memristive devices that change their resistance as a function of the current that passed the device [19]. They might serve as the key element for the construction and synaptic-like interconnection of artificial neurons.

Another emerging and intensively studied field is *quantum information processing*. The realisation of universal quantum computation and simulation would allow to solve tasks that are not computable with established approaches. Quantum communication and cryptography may lead to a novel level of security in information transmission channels and data storage. Progress was driven by completely new experimental techniques, e.g. for the read-out of quantum states. The relevance was underlined by the 2012 Nobel price in physics to Serge Haroche and Dave Wineland

> "for ground-breaking experimental methods that enable measuring and manipulation of individual quantum systems".

It is useful to distinguish between devices that show special capabilities due to quantum mechanical effects but communicate via classical channels and systems which contain units that interact via quantum mechanical (QM) correlations. An example for a novel semi-classical circuit is Rapid Single Flux Quantum (RSFQ) logic which implements classical algorithms with Josephson junctions and superconducting lines [20]. Switching frequencies of several hundred GHz can be reached while the dissipated energy per clock cycle is orders of magnitude lower than in conventional Si technology. While quantum effects lead to a highly non-linear $I(V)$ characteristics in a Josephson junctions the actual information propagates

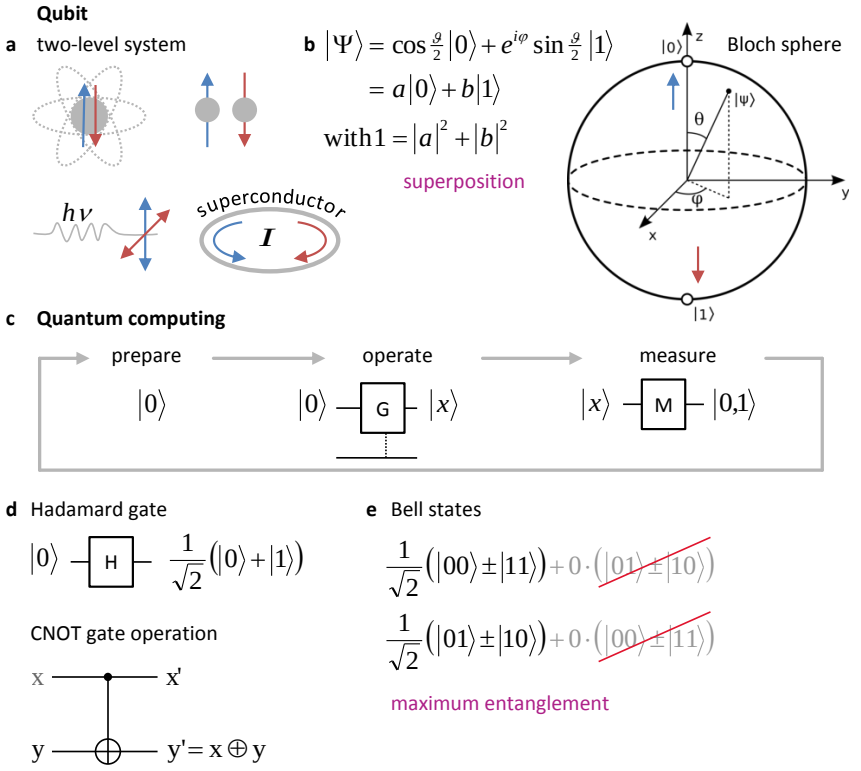

Figure 1.1 Principles of quantum computing. Elemental is the qubit which **a** can be realized with various quantum mechanical two-level systems **b** and is characterized by the linear superposition of two states $|0\rangle$ and $|1\rangle$. Qubits need to exhibit coherence times long enough to perform **c** the quantum computing sequence. After an initialization of the qubits, algorithms can be executed and finally the result is determined by a measurement. **d** Gate operations can act on single (e.g. Hadamard) or multiple qubits (e.g. CNOT Gate). **e** Qubits can be put into a collective state where certain configurations do not occur, which is called entanglement.

via conventional voltage pulse. Despite the advantages in performance, the cryogenic working environment and reliability and integration issues in fabrication render this approach unsuitable as a universal information processing technology.

A fundamental paradigm change arises from controllable correlated quantum systems (Fig. 1.1). They could be used for the implementation of quantum algorithms that promise a drastic speed up of certain mathematical or data-base operations, but would also allow to establish safe communication channels. The basic unit of such a system is the qubit, a QM two-level system. At the current state many rivalling concepts for qubits are investigated, each implementation having their strength and weakness. The investigated systems are diverse and cover photons in a resonator, energy states of isolated atoms, electronic and nuclear spins, and mesoscopic superconducting circuits [21]. For a feasible implementation a trade-off has to be made between temporal quantum coherence (data retention), external control, intra-qubit interaction and integration density.

The flux qubit [22] is a design for a solid state qubit which makes use of the flux quantization in a superconducting ring. Built with classical Josephson junctions the structure requires an external flux bias of $\Phi_0/2$ to form two states associated to currents circulating in opposite directions. This bias may be applied by external field coils, permanent magnets or trapped fields which disturb the system by noise and may influence neighbouring devices by stray fields. Alternative self-biased layouts with π shifting Josephson junctions [23] would not only eliminate sources of noise but also reduce the size, stray fields and complexity of the qubit which facilitates their integration.

The innovative operation modes of quantum circuits are based on two essential principles, called superposition and entanglement. The internal state of a qubit can be regarded as a superposition of the two observable states which manifest when a measurement is performed. Entanglement can be achieved by interactions between multiple qubits resulting in a collective quantum state. If the state of one system from such an entangled ensemble is determined by a measurement, some information about the other systems can be obtained as well. In the extreme case of two qubits, that are in one of the maximally entangled Bell states, the

measurement of one qubit also completely characterises the state of the other qubit.

The entanglement of qubits is the foundation for the implementation of powerful quantum algorithms and essential to establish quantum communication channels. Their security is not based on a sophisticated encryption mechanism but rather on an inherent property of quantum systems, which prevents an undiscovered access to the transmitted data and fundamentally forbids the duplication of a quantum state.

A universal quantum computer [24] would be able to handle every quantum algorithm. For the understanding of specific quantum systems however it might be sufficient to construct a quantum simulator [25]. Such a machine could work as a controllable model system to study quantum effects that, due to the complexity of mathematical modelling, cannot be represented with conventional logic circuits.

1.2 Superconductivity

The phenomenon of superconductivity is a mesoscopic quantum effect. As already described by its name, the most obvious manifestation of the superconducting state is a dissipation-free direct current through a material. Despite a quantum mechanical theoretical framework superconducting correlations can span across macroscopic length scales. The applications of superconductivity are summarized in Fig. 1.2. Magnetic resonance imaging and high-energy particle accelerators are made possible because of the availability of zero resistance magnetic field coils. In addition the quantum nature of the superconducting state allows the construction of highly sensitive magnetometers (SQUIDS) and superconducting elements in microelectronics.

First observations of superconductivity on metals in 1911 by Kammelingh Onnes [26] followed the first liquefaction of helium. Cooled below a material specific critical temperature T_c the dc resistance of mercury, lead and tin drops to zero. Another striking manifestation of superconductivity is perfect diamagnetism called Meissner effect [27]. A phenomenological description of the electromagnetic properties was published by F. and H. London in 1935 [28].

J. Bardeen, L. N. Cooper and J. R. Schrieffer were the first to provide

a complete microscopic theory of superconductivity known as the *BCS theory* [29]. They claimed that in the superconducting state electrons pair via interactions with the lattice and form a superconducting condensate. The attractive interaction between the electrons makes the formation of the Cooper pair energetically favourable. Therefore an energy gap arises within an energy of $\pm\Delta$ around the Fermi energy.

A few years earlier the macroscopic *Ginzburg-Landau theory* (GL) [30] already combined all manifestations of superconductivity and provided a mathematical description using a collective electron wavefunction

$$\Psi(x,t) = \sqrt{n(x,t)} \cdot e^{i\varphi(x,t)} \tag{1.2}$$

with the Cooper pair density n and the superconducting phase φ. The non locality of this entity prevents single electrons from being scattered at the lattice or at defects leading to a vanishing resistance. The GL picture is well suited to describe the effects at superconducting junctions and their behaviour in the frame of this thesis.

High-temperature superconductors (high T_c) The elemental superconductors exhibit rather low critical temperatures, with a maximum value of $T_c^{\text{bulk}} = 9.2\,\text{K}$ for Nb (at standard pressure). Some binary compounds where found to have T_c up to 30 K. The hunt for higher critical temperatures was revived in 1986 when Bednorz and Müller found superconductivity in complex ceramic materials formed by copper oxide planes, which exhibit T_c of about 90 K [32]. In the following years other crystals from this new class of cuprate superconductors were found with T_c ranging well above 100 K which allows cooling with liquid nitrogen (Fig. 1.3). Compared to conventional superconductors the origin of electronic correlations is more exotic. Despite their robust superconducting properties their usage in technology is limited due to difficult fabrication and processing procedures and short coherence length. Nonetheless a lot of research effort revealed interesting material properties and mechanisms.

Exciting new physics can be expected from iron based superconductors which were discovered in 2006 [33,34]. These new compounds, made from layers of Fe and a pnictide (typically As; also N, P, Sb, Bi), significantly differ from cuprates and may follow a non-BCS theory that still has to

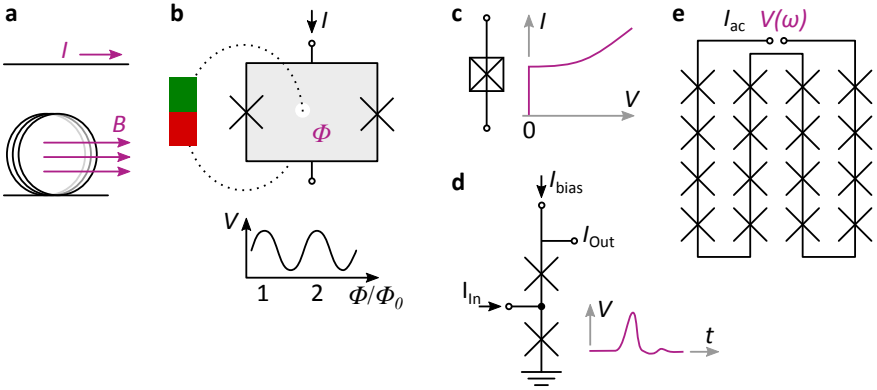

Figure 1.2 Applications of superconductivity in bulk materials or in Josephson junctions ($\times$) cover **a** transport of electrical current I or generation of large magnetic fields B, **b** extremely sensitive detection of magnetic flux Φ with a superconducting quantum interference device (SQUID), **c** highly non-linear $I(V)$ characteristics for mixers in radio telescopes, **d** superconducting circuitry like rapid single flux quantum logic (RSFQ) and **e** time-based voltage standard due to $V(\omega)$.

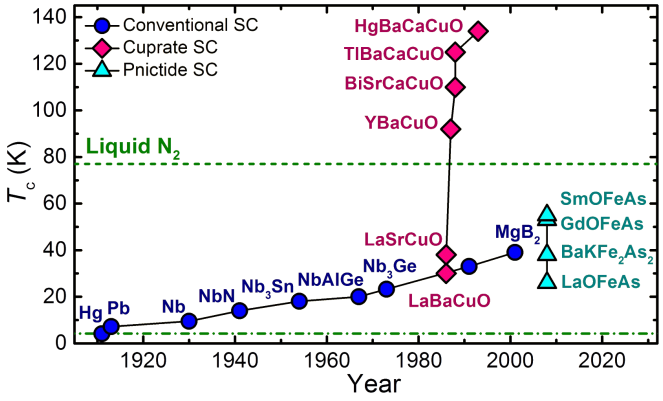

Figure 1.3 Temperature of superconducting transition T_c versus year of experimental verification. The superconductors are classified into elemental or compound materials (●), ceramics based on CuO planes (◆) and Fe based pnictides (▲). [adapted with permission from [31]]

be developed [35].

Phenomena of Superconductivity

The microscopic framework of the BCS theory yields a fundamental description of superconductivity for equilibrium bulk superconductors with constant energy gaps and excitation spectra. However, for spatially inhomogeneous or dynamic problems a BCS solution is difficult to achieve. Many phenomena at interfaces and the vortex state of type II superconductors are readily explained by the *Ginzburg-Landau theory* (GL). It turned out to be better suited for the treatment of the macroscopic quantum-mechanical nature of the superconducting state. At the same time GL delivers an appropriate picture for the electro-magnetic properties and dynamics. GL concentrates on the superconducting electrons and introduces a pseudo-wavefunction Ψ which is linked to the Cooper pair density via

$$n_{\mathrm{s}}(x) = |\Psi(x)|^2. \tag{1.3}$$

Important solutions that are obtained by minimizing the free energy with a variational principle are summarized below. Several connections and analogies to the BCS theory exist and close to the critical temperature the GL mathematically follows as a limiting case of BCS [36].

An important feature that emphasizes the non-locality of the superconducting correlations of electrons is their *coherence length*. Without an intolerable energy pay off the wavefunction can only slowly change with the position. It is connected to the free path length of electrons in a material. While typical coherence length of elemental superconductors are in the range of 35 nm for Nb and up to several 100 nm for others the high T_{c} materials stay in the order of Å. The coherence length diverges with temperature just below T_{c} according to

$$\xi(T) \propto \frac{1}{\sqrt{1-\frac{T}{T_{\mathrm{c}}}}} \tag{1.4}$$

and well below T_{c} it resembles the result from the microscopic theory for

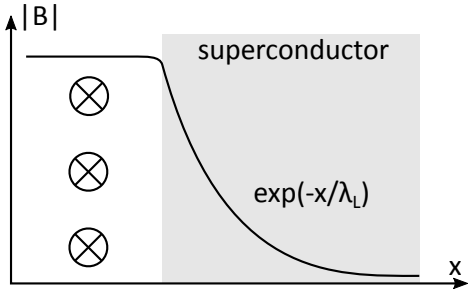

Figure 1.4 Magnetic fields B decay exponentially into a superconductor with a decay length, called London penetration depth λ_L

pure metals

$$\xi_0 = 0.18 \frac{\hbar v_\mathrm{F}}{k_\mathrm{B} T_\mathrm{c}} \tag{1.5}$$

with the Fermi velocity v_F. As a result, ξ_0 is the maximum distance over which an attractive interaction between electrons can be mediated by the lattice.

A characteristic feature of a bulk superconducting material is perfect diamagnetism, which is exploited for levitation experiments and applications. Magnetic fields decay exponentially into the superconductor on a lengthscale, called London penetration depth λ_L (Fig. 1.4).

Another striking result of the macroscopic quantum nature of superconductivity is the *flux quantisation* [15,37]. The magnitude of the complex superconducting order parameter Ψ is requirement for a single-valued. Therefore the phase φ may only change by multiples of 2π along a closed path through the superconducting material, i.e.

$$\oint \boldsymbol{\nabla \varphi} \cdot \mathrm{d}\boldsymbol{l} = 2\pi \mathrm{n}. \tag{1.6}$$

For the special case of a superconducting ring that is threaded by a magnetic field the phase gradient $\nabla\varphi$ can be expressed by the supercurrent

density $\boldsymbol{J}$ and the vector potential $\boldsymbol{A}$ as

$$\boldsymbol{\nabla\varphi} = \frac{2\pi}{\Phi_0}\left(\boldsymbol{A} + \frac{m}{2e^2 n_\mathrm{s}}\boldsymbol{J}\right). \tag{1.7}$$

Substitution into (1.6) yields

$$\frac{2\pi}{\Phi_0}\left(\oint \boldsymbol{A}\cdot \mathrm{d}\boldsymbol{x} + \oint \frac{m}{2e^2 n_\mathrm{s}}\boldsymbol{J}\cdot \mathrm{d}\boldsymbol{l}\right) = 2\pi \mathrm{n} \tag{1.8}$$

and via Stokes rule and $\boldsymbol{B} = \nabla \times A$ results in

$$\underbrace{\iint \boldsymbol{B}\cdot \mathrm{d}\boldsymbol{\sigma}}_{\Phi_\mathrm{ext}} + \frac{m}{2e^2 n_\mathrm{s}}\oint \boldsymbol{J}\cdot \mathrm{d}\boldsymbol{l} = \mathrm{n}\cdot\Phi_0. \tag{1.9}$$

Therefore the flux through the ring takes multiples of the flux quantum

$$\Phi_0 = \frac{h}{2e} = 2.068\times 10^{-15}\ \mathrm{Vs}. \tag{1.10}$$

and is composed of the sum of externally applied flux Φ_ext and the field, generated by the supercurrent in the loop. Depending on the external field $\boldsymbol{B}$, a supercurrent is induced in the ring to maintain an integer multiple of Φ_0. The quantisation condition can be compared to the quantized path of an electron in the shell of an atom.

1.3 Electron Tunneling

As a consequence of quantum mechanics, small particles show a finite probability for the transmission through thin barriers of potential energy V which is larger than the particle energy E (Fig. 1.5). The wavefunction of the particle does not abruptly vanish at the edge of the barrier but decays into the barrier. In particular electrons may be exchanged between metallic electrodes across a thin insulator layer, called tunneling junction [38]. Tunnel junctions are for example fabricated by the vacuum deposition of two metal thin films and the formation of a thin oxide barrier in between. For a considerable tunneling current the barrier

thickness shouldn't be larger than a few nm and the current also changes with the material specific barrier height. The quantum tunneling through tunnel junctions results in a non-vanishing conductance in normal metal structures and the Josephson effects at structures with superconducting electrodes [14]. The rate at which these tunnel processes occur can be estimated from the Wentzel-Kramers-Brillouin (WKB) approximation [39]. The tunnel probability $|\mathcal{T}|^2$ of an incident wave can be described by

$$|\mathcal{T}|^2 = \exp\{-2K\} \tag{1.11}$$

with an integration along the tunnel path through the barrier

$$K = \int_{x_1}^{x_2} \sqrt{\frac{2m*}{\hbar^2}\left[V(x) - E_x\right]}\,\mathrm{d}x, \tag{1.12}$$

where $m*$ is the electronic mass. Without an applied voltage across the barrier, the tunneling currents in both directions cancel and overall no current is observed in this dynamic equilibrium. If a voltage $V \neq 0$ is applied, the Fermi energies of both electrodes are shifted with respect to each other and a net current may be observed. The tunneling current depends not only on the transmission probability through the barrier but also contains detailled information about the electronic structure of the electrodes. Usually elastic tunneling dominates the tunneling current and is related to the density of states ρ of the two electrodes. Signatures from ρ can be found in the derivative of the $I(V)$ curve according to

$$\frac{\mathrm{d}I}{\mathrm{d}V}(V) \approx \rho_{\mathrm{E1}}(E_{\mathrm{F}} - \mathrm{e}V) \cdot \rho_{\mathrm{E2}}(E_{\mathrm{F}}), \tag{1.13}$$

where the negative potential is applied to electrode E1. Especially the characteristic BCS density of states of a superconductor with an energy gap and a large density of states above the gap energy can be probed by tunneling structures.

A lot of information about the electronic structure of materials and molecules can be acquired by inelastic electron tunneling spectroscopy (IETS) [39]. The tunneling electrons may interact with a variety of excitations like vibrations of the atomic lattice (phonons) or rotational

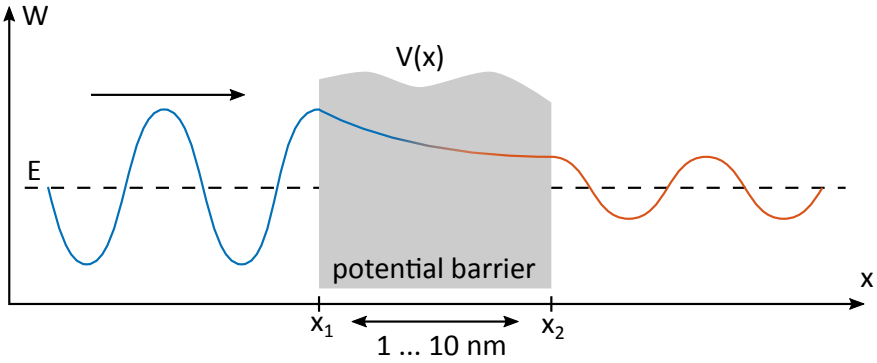

Figure 1.5 Schematics of tunneling process which allows a particle with energy E at the left to cross a potential barrier $V > E$ and is found with finite probability amplitude at the right side.

and vibrational modes of molecules near the barrier. If the energy of a tunneling electron exceeds the characteristic energy eV of an excitation it may scatter inelastically which changes the conductance of the barrier. The onset of such an additional inelastic tunneling channel manifests as a peak in the

$$\frac{\mathrm{d}^2 I}{\mathrm{d}V^2}(\mathrm{e}V) \tag{1.14}$$

dependence. The second derivative of $I(V)$ can be recorded by the lock-in technique with high resolution, sensitivity and excellent selectivity against noise [40]. Compared to other optical or X-Ray probe techniques, very small amounts of material can be spectroscopically analysed by IETS. Fundamental information about superconductivity and the phonon structure of materials can be acquired by tunneling studies [41]. In particular, tunneling experiments allow to determine the electron–phonon spectral function $\alpha^2 F(\omega)$ (Eliashberg function) and therefore the energies and energetic width of superconducting correlations.

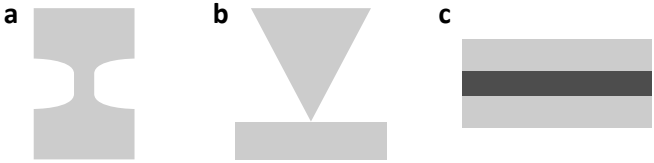

Figure 1.6 Types of Josephson junctions. The barrier is realized by **a** constriction in the superconductor, **b** point contact or **c** a thin film stack.

1.4 Josephson Effects

If two superconductors exchange Cooper pairs via any kind of barrier this interface is called a Josephson junction (JJ). A variety of structures with this general geometry follow the principles that Brian Josephson predicted in 1962 [42]. In the theoretical publication he showed that a zero voltage supercurrent

$$I = I_\mathrm{c} \cdot \sin(\Delta\varphi) \tag{1.15}$$

can flow between two superconducting electrodes separated by a thin insulating tunnelling barrier. The current of Cooper pairs across the junction depends on the phase difference $\Delta\varphi$ of the GL wavefunctions in the two electrodes and is limited by the critical current I_c.

The second essential finding was that a voltage difference V across the junction changes the phase difference $\Delta\varphi$ according to

$$\frac{\mathrm{d}(\Delta\varphi)}{\mathrm{d}t} = \frac{2\mathrm{e}V}{\hbar} \tag{1.16}$$

with the electron charge e. Via (1.15) this leads to an alternating super-current with the amplitude I_c where the associated quantum energy $h\nu$ matches the energy change $2\mathrm{e}V$ of a Cooper pair when it crosses the junction. Such an alternating current without any DC component is true for an ideal junction, but not sufficient to describe the experiments. A model for the electrical behaviour of a real junction at finite voltages requires to consider additional parasitic capacitance and resistance (cp. sec. 1.4).

Both equations have been confirmed not only for the originally proposed tunnel barriers, called SIS junctions (S: superconductor, I: insulator), but also for other types of barriers or *weak links* in general. In the case of a normal metal (N) barrier the structure is called SNS Josephson junction, geometrical constrictions in a superconductor (c) are referred to as ScS (Fig. 1.6).

In the following the intrinsic properties of a Josephson junction and its response to external excitations will be further characterized. The energy which is stored in a junction is calculated by integration of the electrical work that needs to be applied to achieve a certain phase difference between the electrodes $\Delta\varphi$. The free energy becomes

$$F = \text{const.} - E_\text{J} \cdot \cos\Delta\varphi \qquad \text{with} \quad E_\text{J} = \frac{I_\text{c}\Phi_0}{2\pi}, \tag{1.17}$$

having a minimum for $\Delta\varphi = 0$ which is the energetically favourable ground state. The Josephson energy E_J and the critical current I_c are a measure of how strongly the phases of the two superconducting banks couple together through the junction. They depend on many factors, like the materials used for the barrier and the superconductors, their interfaces, the geometry of the weak link structure and the temperature.

To eliminate the influence of junction geometry in the evaluation of data, the area-independent $I_\text{c}R_\text{N}$ product can be used. R_N is the resistance of the junction in the normal state. The Ambegaokar-Baratoff [43] theory establishes a direct link to the superconducting gap Δ. A simplified result for symmetric tunnel barriers at $T = 0\,\text{K}$ is

$$I_\text{c}R_\text{N} = \frac{\pi\Delta}{2e}. \tag{1.18}$$

IV curve

Throughout the thesis the $I(V)$ curve of a Josephson junction will be used as a central measurement to deduce characteristic parameters like the critical current I_c. An overview of the main features, that appear for tunneling structures and semiconducting barriers, will be given in the following. Unless otherwise stated the electrical measurements in this thesis were performed with a current source.

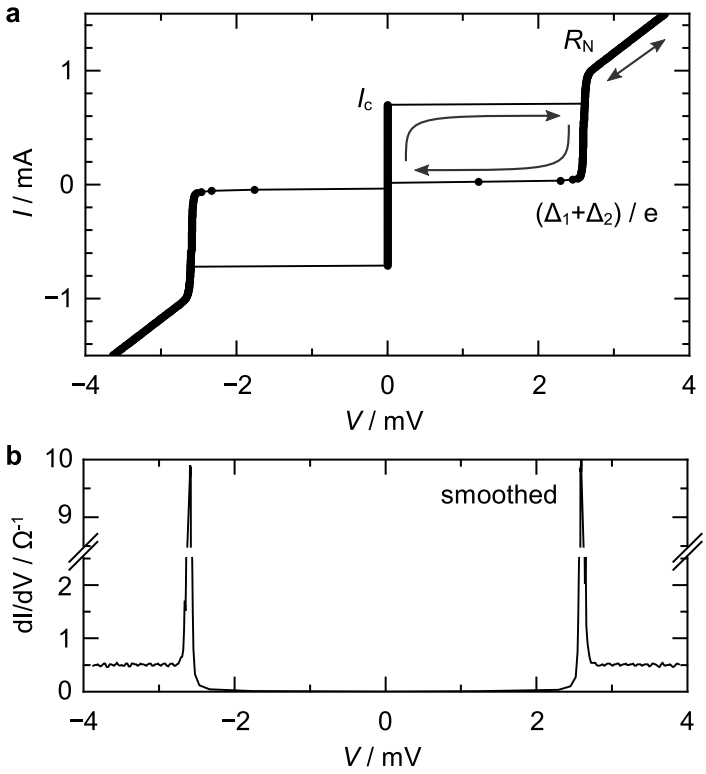

Figure 1.7 Experimental data for a high quality Nb | Al | AlO_x | Nb Josephson junction **a** directly measured $I(V)$ reveals critical current I_c, sum of the superconducting gap of the two electrodes $\Delta_1 + \Delta_2$ and normal resistance R_N; the arrows indicate direction of sweep for the current driven measurement. **b** numerically derived $\mathrm{d}I/\mathrm{d}V$ curve is related to the density of states of the superconducting electrodes [c01^{id}]

The distinctive energy gap 2Δ that arises around the Fermi energy in a superconducting material can electronically be detected by measurements of the $I(V)$ dependence over a superconductor–insulator–superconductor (SIS) structure [38]. The tunneling current depends on the density of states (DOS) of the electrodes. So BCS shaped DOS in a superconductor can introduce a discontinuous jump into the $I(V)$ curve of a SIS junction. The $\mathrm{d}I/\mathrm{d}V$ dependence also provides valuable information about the density of states of the quasi particle excitations in the superconducting electrodes [39]. Especially, peaks in the $\mathrm{d}I/\mathrm{d}V$ correspond to maxima in the density of states.

An SIS junction type $I(V)$ is depicted in Fig. 1.7. Starting at $I = 0$ a finite Cooper pair current can be send through the junction without a voltage drop. According to (1.15), the current is associated with a phase difference between the two electrodes. If the current exceeds a certain value, the critical current I_c, single electrons (quasiparticles) contribute to the current. Due to the energy gaps Δ_1 and Δ_2 in the two superconducting electrodes, direct tunneling can only occur for a junction voltage of $(\Delta_1 + \Delta_2)/\mathrm{e}$ and larger. A certain amount of current can be supported by the BCS-type peaks in the DOS at the edges of the superconducting gap. For larger currents the $I(V)$ curve approaches the ohmic behaviour of the normal state with a conductivity $1/R_\mathrm{N}$. If the current is reduced from the resistive state, the junction current is determined by the quasiparticle excitations in the superconducting gap and at a certain return current, the junction returns to the zero voltage state. Fig. 1.7 shows a highly hysteretic junction. This behaviour is typical for an underdamped contact where the free evolution of the Josephson phase in the voltage state, once started, persists down to low currents. In contrast overdamped junctions would provide a single valued $I(V)$ curve.

A knee feature at the transition between gap voltage and resistive branch may occur as a consequence of a normal metal layer next to the tunnel barrier in gas oxidized $\mathrm{Nb}\,|\,\mathrm{AlO_x}\,|\,\mathrm{Nb}$ junctions [44, 45].

RCSJ

A common equivalent circuit for a physical Josephson junction is the resistively and capacitively shunted junction (RCSJ) model. It is suited

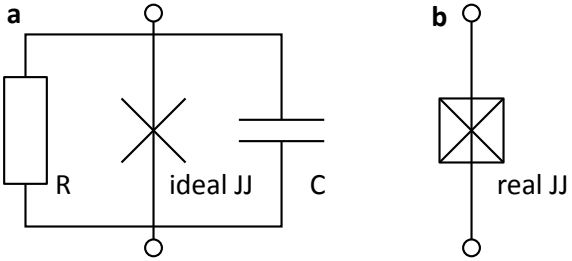

Figure 1.8 Schematics of RCSJ model where the real junction is described by **a** an ideal Josephson junction (×) which is shunted by a parallel resistor (R) and capacitor (C) and **b** the integrated symbol for such an RCSJ junction.

to explain the dynamics of a real junction in the voltage state where the ideal Josephson equations (1.15) and (1.16) alone are not sufficient. Specifically in RCSJ the ideal junction is shunted by a resistance R and a capacitance C (Fig. 1.8). They account for dissipative currents through the junction and the geometric capacitance between the two electrodes, respectively. A good estimate for the magnitude of R at large voltage is the normal state resistance R_N. A significant deviation from this rule applies to tunnel barriers for voltages $V < V_\mathrm{gap} = {}^{2\Delta}/_{e}$. Tunneling characteristics can be incorporated in the RSCJ model by a voltage dependent resistance $R(V)$ to account for a different resistance of quasi-particle excitations within the superconducting energy gap and for electronic states at larger energies [39]. Within this superconducting gap the quasi particles freeze out leading to a divergence of the resistance

$$R_\mathrm{SIS} = R_\mathrm{N} \cdot \exp\left(\frac{\Delta}{k_B T}\right) \quad \text{for } V < V_\mathrm{gap}. \tag{1.19}$$

The overall current through the three circuit elements can be expressed as

$$I = I_\mathrm{c} \cdot \sin(\Delta\varphi) + \frac{V}{R} + C\frac{\mathrm{d}V}{\mathrm{d}t}. \tag{1.20}$$

For the ideal Josephson junction, as described by the first term, the second Josephson equation (1.16) holds. So we can drop V in favour of

Table 1.1 Analogy between the electrical quantities in the RSCJ model for a Josephson junction and a mechanical driven pendulum

Josephson junction		mechanical pendulum
DC current	I	applied torque
capacitance	C	moment of inertia
conductance	$1/R$	damping coefficient
critical current	I_c	maximum gravity torque
phase difference	$\Delta\varphi$	angle from the vertical

the phase difference $\Delta\varphi$. The resulting differential equation describes the dynamics of a physical Josephson junction,

$$\frac{\mathrm{d}^2(\Delta\varphi)}{\mathrm{d}\tau^2} + \frac{1}{Q}\frac{\mathrm{d}(\Delta\varphi)}{\mathrm{d}\tau} + \sin(\Delta\varphi) = \frac{I}{I_\mathrm{c}} \tag{1.21}$$

with the time variable

$$\tau = \omega_\mathrm{p} t \qquad \text{where} \quad \omega_\mathrm{p} = \sqrt{\frac{2eI_{\mathrm{c}0}}{\hbar C}} \tag{1.22}$$

is the plasma frequency and a quality factor

$$Q = \omega_\mathrm{p} RC \quad \left(= \sqrt{\beta_\mathrm{c}}\right). \tag{1.23}$$

The influence of this damping term was investigated by Stewart and McCumber [46,47] and their parameter β_c became common to distinguish between different regimes of junction dynamics. In the *overdamped* ($\beta_\mathrm{c} \ll 1$) case $\Delta\varphi$ closely follows the external driving voltage leading to a single valued current–voltage curve. This $I(V)$ converges from above to the straight line, which is defined by the normal resistance R_N. In contrast, an *underdamped* ($\beta_\mathrm{c} \gg 1$) junction exhibits a more volatile phase evolution which manifests itself in a hysteretic IV dependence.

To intuitively understand the evolution of the phase difference $\Delta\varphi$ the system can be compared to mechanical analogues which obey the same type of ordinary differential equation (1.21), namely a driven pendulum

(Table 1.1) or the motion of a particle in a tilted washboard potential. A pendulum at rest follows gravity and points vertically downwards. If a constant torque is applied, the pendulum moves sideways until the tangential gravity component balances the driving torque. Once the external torque is strong enough to align the pendulum horizontally, it will set the pendulum into a continuous rotation. This perpetual change of the angle corresponds to an evolution of the electrical $\Delta\varphi$ and therefore indicates the voltage state of a Josephson junction. The pendulum's dynamics and the return into an oscillatory motion and static state are governed by parameters like moment of inertia and damping. A similar influence for Josephson junctions is assigned to the shunting capacitance C and conductance $1/R$, respectively.

Ic(B) - Magnetic Field

The key to work out the response of a Josephson junction to a magnetic field $\boldsymbol{B}$ is the replacement of $\Delta\varphi$ by a gauge invariant phase difference

$$\gamma = \Delta\varphi - \left(\frac{2\pi}{\Phi_0}\right) \int_{\mathrm{E1}}^{\mathrm{E2}} \boldsymbol{A} \cdot \mathrm{d}\boldsymbol{s} \tag{1.24}$$

where the path integral over the vector potential $\boldsymbol{A}$ extends from one electrode (E1) to the other (E2). Without magnetic fields involved, γ reduces to $\Delta\varphi$ so that the preceding discussions stay valid.

Important structural aspects about the Josephson junction can be deduced from the dependence of the critical current I_c on an applied magnetic field. In particular, this pattern contains information about the current density distribution inside the junction and geometrical dimensions.

This description focuses on an experimental setup where an external homogeneous magnetic field is applied in the junction plane aligned parallel to one edge of a rectangular junction (Fig. 1.9). The superconducting electrodes are not substantially affected since they are thicker than λ_L and the field is much smaller than the critical field that would be needed to suppress superconductivity completely. Also at this point the critical current is considered to be low enough to neglect field screening and self fields, so that the external flux threads the whole structure. The

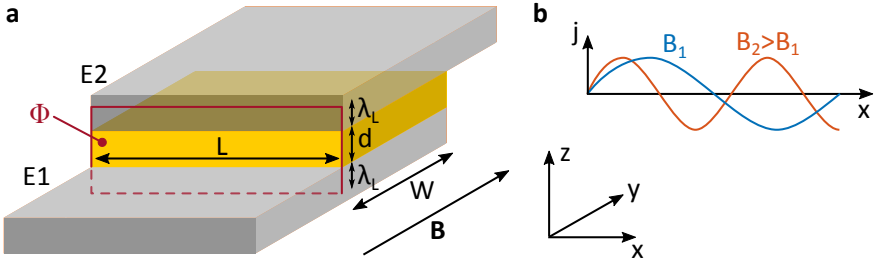

Figure 1.9 Thin film tunnel barrier with an in-plane magnetic field B. **a** The field penetrates the junction over the length of the barrier L, thickness d and also a distance λ_L into both electrodes (E1,E2). **b** The current density $j(x)$ varies along the x direction.

magnetic field lets the phase difference vary over the junction plane xy leading to a local current density

$$j(x, y) = j_c \cdot \sin \gamma(x, y). \tag{1.25}$$

In the case of a rectangular junction with a homogeneous critical current density all over the junction area the current density oscillates sinusoidally in the direction perpendicular to the applied field. The number of periods across the junction depends on the flux that penetrates the junction region of width L and thickness $2\lambda_L + d$. For every multiple of Φ_0 an integer number of periods appears over L and the total Josephson current cancels to 0. For a magnetic field B the maximum super-current through the junction becomes

$$I_c(\Phi) = \left| \frac{\sin(\pi\Phi/\Phi_0)}{\pi\Phi/\Phi_0} \right|, \qquad \text{with} \quad \Phi = B \cdot (2\lambda_L + d) \cdot L \tag{1.26}$$

which resembles the diffraction pattern amplitude of an optical single slit and is therefore also called *Fraunhofer diffraction pattern.*

A more general treatment includes spacial inhomogeneous critical current densities, arbitrary junctions shapes and variations in the local flux density which affects $\gamma(x, y)$. The integration of the current density

(1.25) over the whole junction

$$I(B, \Delta\varphi) = \iint_{\mathrm{W\,L}} j_\mathrm{c} \cdot \sin\gamma(x, y)\ \mathrm{d}x\,\mathrm{d}y \tag{1.27}$$

yields the total supercurrent versus the magnetic field. Maximized with respect to variations of $\Delta\varphi$ this term results in a $I_\mathrm{c}(B)$ pattern which is the Fourier transform of the lateral critical current density distribution in the direction perpendicular to the field. A variety of examples and illustrations that facilitate the determination of critical current density profiles from $I_\mathrm{c}(B)$ patterns can be found in the book from Barone [15].

A further generalization which drops the requirement of negligible self fields by considering the electro dynamics of the current comes to the conclusion that the DC Josephson current is confined near the edges of a junction within a length scale of the Josephson penetration depth

$$\lambda_\mathrm{J} = \sqrt{\frac{c\,\Phi_0}{8\pi^2 I_\mathrm{c}(2\lambda_\mathrm{L} + d)}}. \tag{1.28}$$

The previous descriptions stay valid in the regime of *small* junctions ($L < \lambda_\mathrm{J}$). Large critical currents or wide junctions dimensions however can lead to an intermediate or *large* junction ($L \gtrsim \lambda_\mathrm{J}$). First sign of the emerging influence of the self fields are shift and deformation of the maxima and for clearly large junctions the magnetic field dependence of the critical current becomes the envelope of a series of overlapping triangles. An extensive study for the in-line geometry was performed by Owen and Scalapino [48]. However, we restrict ourselves to recognize and avoid long junctions since they obscure the impact of the functional barriers that are going to be studied in this thesis.

1.5 Charge Transport Mechanisms in Josephson Tunnel Barriers

The electronic structure of a Josephson barrier can have a significant effect on the current transport. This is especially interesting for $\mathrm{Si}_{1-\delta}\mathrm{Fe}_\delta$ alloys with variable doping of Fe into the Si matrix at low temperatures

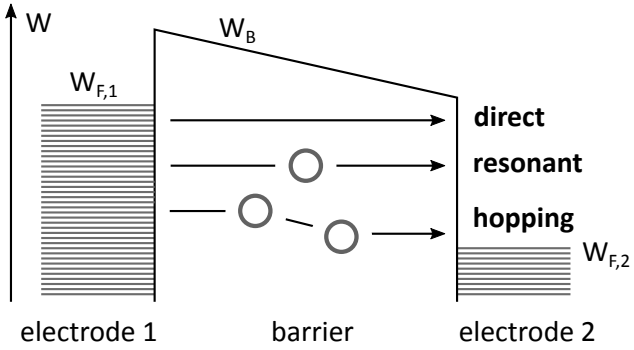

Figure 1.10 Schematic band diagram of a tunnel barrier showing different conductivity mechanisms through the barrier. The Fermi energies W_F are shifted due to an applied voltage. Electrons may tunnel **directly** between the electrodes while keeping their energy, tunnel in a two step process via an intermediate **resonant** state or travel with the help of a larger number of intermediate **hopping** states.

(sec. 3.2). At low temperatures a fundamentally different conductance behaviour can be expected for pure Si in comparison to metallic Fe. With increased metallic doping into Si additional electronic states are available in the barrier which impacts the mechanisms of charge transport [49]. At low concentrations δ, Fe may form localized states that serve as hopping centers for electrons [50, 51]. The magnetic impact of Fe which also influences superconducting correlations is disregarded in this section.

The conductance G of a thin insulating barrier has been analysed in detail and can be considered as a composition of different conductivity mechanisms [52, 53],

$$G(T) = \underbrace{G_0}_{\text{direct}} + \underbrace{G_1 + \delta G_1(T)}_{\text{resonant}} + \underbrace{\sum_{N\geq 2} G_N(T)}_{\text{hopping}} \qquad (1.29)$$

with direct elastic tunneling G_0, resonant tunneling via a localized state G_1 including a temperature correction $\delta G_1(T)$ and hopping along linear chains of N states G_N. A sketch of the band diagram of a tunnel barrier

which visualizes the different charge transport mechanisms is shown in Fig. 1.10.

Rather than describing the different mechanisms one after the other a summary on their detection in experimental data will be presented. Information on the dominating conductance mechanisms of a sample may be acquired from experimental dependencies of the conductance G on barrier thickness d, applied voltage V and temperature T [52].

Low temperature measurements of the normal current conductivity in tunnel junctions for increasing barrier thickness d may show the transition from a region with direct tunneling

$$G_0 \approx e^{-2\alpha d} \tag{1.30}$$

into a region dominated by resonant tunneling [54, 55]

$$G_1 \approx e^{-\alpha d}. \tag{1.31}$$

In a logarithmic plot of $G(d)$ this transition would manifest as a kink between lines which differ in slope by a factor of two. The localization length α^{-1} depends on material and barrier properties. It was found that resonant tunneling dominantly occurs via states in the middle of the barrier [52].

The voltage dependence of the conductivity also reveals information about the charge transport. Close to $V = 0$ the dependence $G(V)$ is linear. For larger barrier thickness and larger voltage however, non-linear behaviour is observed which allows conclusions on the current transport. At low barrier thickness the direct tunneling contributes with integer powers of the voltages as $G_0 \approx a + b \cdot V + c \cdot V^2$ with coefficients a, b, c [56, 57]. For thicker barriers, hopping over one dimensional chains of localised states may become more likely. In the case of two hopping centers Glazmann and Metveev [58] showed a dependence

$$G_2 \approx V^{4/3}. \tag{1.32}$$

With increasing thickness, larger chains with N hopping centers can

dominate the conductance according to the generalized expression

$$G_{\mathrm{N}} \approx V^{\mathrm{N}-(2/[\mathrm{N}+1])}. \tag{1.33}$$

Many transport mechanisms require a correction due to a finite junction temperature. These terms are mainly $\propto T^2$ accounting for the broadening of the Fermi statistics involved in direct tunneling [53,59] and for inelastic transport processes due to electron–phonon interactions in resonant tunneling [52]. For $\mathrm{N} \geq 2$ the conductance is proportional to non-integer powers of T

$$G_{\mathrm{N}} \approx T^{\mathrm{N}-(2/[\mathrm{N}+1])}. \tag{1.34}$$

This expression is analogous to the voltage dependence of such chains.

For thicker barriers and in the limit of bulk samples a variable range hopping model finds the preferred hopping distance as a trade-off between the overlap of localized states and their energy difference, which favour short and long separations, respectively. The result is also called Mott hopping [60] and shows a temperature dependence

$$G \approx e^{-\left(\frac{T*}{T}\right)^{1/4}} \tag{1.35}$$

where the parameter $T*$ depends on barrier parameters. If the density of states around the Fermi energy is not constant but reduced a similar derivation leads to the Shklovskii-Efros law [61]

$$G(T) \approx e^{-\left(\frac{T*}{T}\right)^{1/2}}. \tag{1.36}$$

1.6 Ferromagnetic Barriers

So far, an overview about the physics and electrical characteristics of a classical Josephson junction has been given. In this chapter the description is extended towards junctions that incorporate ferromagnetic material in the barrier. Under certain conditions these junctions can exhibit a ground state with a phase difference of π between the superconducting electrodes. Such a device is called a π Josephson junction [62].

We will discuss the origins and consequences of this particular state. The section will end with an overview about predicted and experimentally realized types of π junctions. They provided valuable motivation for the development of junctions in the frame of this thesis.

Other effects are beyond the scope of this work. The insertion of magnetic material in the junction allows magnetic superconducting memory cells working with an intrinsic magnetic bias [9] or based on junctions with an intrinsic phase difference between 0 and π, called φ junction [10]. Other topics of research are the competing order phenomena of ferromagnetism with parallel spin order and superconductivity with antiferromagnetic spin order which may lead to spin triplet superconductivity [63].

1.6.1 Ferromagnetism

An atom may exhibit a magnetic moment $\boldsymbol{\mu}$ which arises from the intrinsic spin and the angular momentum of its valence electrons. In general a magnetic moment is generated by a circulating current. In an ensemble, several of these magnetic moments can couple to each other which may lead to a long range order and a collective orientation in a spontaneous direction. A material with an intrinsic parallel alignment of $\boldsymbol{\mu}$ which causes a finite global magnetization $\boldsymbol{M}$ is called a ferromagnet. The coupling induced order is disturbed by thermal excitations and vanishes above a material specific Curie temperature T_{Curie}. Large T_{Curie} correspond to a strong coupling and low values indicate a weak coupling.

The classical electrostatic dipole–dipole interaction of two electrons in a solid corresponds only to a temperature in the range of 0.01 K, orders of magnitude smaller than the values which occur in real ferromagnets [64]. A stronger coupling follows from a QM treatment of two electrons. The overlap of the wave functions results in two possible configurations. In the singlet state the electron spins align antiparallel with an energy $E_{\uparrow\downarrow}$. In the triplet state the spins are aligned parallel leading to an energy $E_{\uparrow\uparrow}$. If the electrostatic exchange energy

$$E_{\mathrm{ex}} = E_{\uparrow\downarrow} - E_{\uparrow\uparrow} \tag{1.37}$$

is larger than zero, a parallel spin ordering can reduce the potential energy of the system. However, due to the Pauli principle the ordering

also affects the kinetic energy. An electronic state can be occupied by two Fermions with antiparallel spin. If a parallel spin orientation shall be realized one electron needs to increase its energy above the Fermi energy E_F which enhances the total energy of the system. A many particle system that satisfies the Stoner criterion [65]

$$J \cdot N(E_\mathrm{F}) \geq 1 \tag{1.38}$$

can be ferromagnetic. It represents the trade-off between the gain of electrostatic exchange energy, as expressed by the Stoner coupling factor J, and the enhancement of kinetic energy, which inversely depends on the density of states at the Fermi energy $N(E_\mathrm{F})$. The criterion is fulfilled for the metals Fe, Co and Ni and nearly reached for Pd and Mn.

The magnetic field $\boldsymbol{B}$ acts on moving charges by the Lorentz force and influences superconducting correlations. In a material it is composed by

$$\boldsymbol{B} = \mu_0(\boldsymbol{H} + \boldsymbol{M}) \tag{1.39}$$

an externally applied field $\boldsymbol{H}$, e.g. produced by a magnetic coil, and an internal magnetization of the material $\boldsymbol{M}$, which may arise as a response on $\boldsymbol{H}$ or from a collective order of magnetic moments. It is important to note that throughout this thesis the magnetic field $\boldsymbol{B}$ is presented synonymous for the externally applied field. While this convention is correct for non magnetic barriers, the finite $\boldsymbol{M}$ of ferromagnetic barriers can introduce an offset on $\boldsymbol{B}$. Moreover the external field may also change the configuration of microscopic moments and therefore modify $\boldsymbol{M}$. This effect is commented at the relevant parts of the experimental section.

1.6.2 π Josephson Junctions

A Josephson junction with a negative critical current $-I_\mathrm{c}$ may arise from magnetic material in the barrier. As a convention the magnitude of I_c is positive. It is worth to recap the relations for conventional Josephson junctions and study the impact of the negative critical current. The

negative critical current causes a negative Josephson energy

$$E_{\mathrm{J}}^{\pi} = -\frac{I_{\mathrm{c}}\Phi_0}{2\pi} = -E_{\mathrm{J}}. \tag{1.40}$$

Insertion into the expression for the free energy of a Josephson junction (1.17) results in

$$F^{\pi} = \text{const.} + E_{\mathrm{J}} \cdot \cos(\Delta\varphi) \tag{1.41}$$

with energetic minima at $\Delta\varphi \bmod 2\pi = \pm\pi$. This ground state clearly differs from the conventional junction by the formation of an intrinsic phase shift of π. The consequences for a single device are subtle, but they become significant for superconducting circuits that are sensitive to the current phase relation (CPR) which, according to (1.15), writes as

$$I_{\mathrm{s}} = -I_{\mathrm{c}} \cdot \sin(\Delta\varphi) = I_{\mathrm{c}} \cdot \sin(\Delta\varphi + \pi). \tag{1.42}$$

A conventional junction is also referred to as 0 Josephson junction, owing to a ground state phase difference of zero. The $I(V)$ and $I_{\mathrm{c}}(B)$ measurements of a π junction do not differ from a conventional Josephson junction. So both measurements, and all electrical experiments at the individual junction in general, are insufficient to reveal the negative critical current or any sign of a π junction.

However, several detection schemes can be used to identify the π state. A direct method is to incorporate the junction into a superconducting circuit which behaves different depending on the CPR relation of the junction used [66, 67]. The basic phase sensitive experiments are to incorporate the junction into a superconducting loop or SQUID or to manufacture a junction with facets of 0 and π parts [68–70]. The downside of this approach are the technological difficulties and additional complexity needed in fabrication and measurement procedures. An indirect method makes use of the fact that certain variations in the junction parameters or measurement conditions can lead to a transition from the 0 regime to a π junction. This transition is accompanied by a vanishing critical current. As explained in the following section, the thickness of a ferromagnetic barrier or the junction thickness are such parameters that can lead to a 0–π transition. In experiments an array of

several individual junctions which monotonously differ in their barrier properties (thickness of ferromagnetic layer, alloy composition) can be characterized and allow to identify critical values for the transition. For junctions that are close to the transition thickness $d_{0-\pi}$ a temperature induced transition from one to the other regime is also possible.

In this work the thickness induced 0–π transition will be studied intensively. Details on the physical mechanisms and experimental realisations will be presented in the following.

1.6.3 Origin of π Junctions

If a supercurrent is flowing through an inductance it will experience a phase shift which is proportional to the inductance of the device and the current itself [71]. An example for a non linear current–phase relation is the first Josephson relation which describes weak links between superconductors. All cases have in common that in the ground state, without a current, no phase gradients exist in the superconductor.

In contrast a rather uncommon intrinsic phase difference of π can occur in Josephson junctions with ferromagnetic barriers. The competing orders of Cooper pairs with anti-parallel spins and ferromagnetism with a favour for a parallel spin alignment lead to interesting physics if both phenomena are combined. Especially at the interfaces between a superconductor (S) and a ferromagnet (F) both effects can coexist. This section describes how the mentioned π shift can appear over barriers made from a ferromagnetic metal or ferromagnetic insulator.

Proximity Effect

The non-local nature of the superconducting state results in a phenomenon called proximity effect. Since the collective wavefunction of the Cooper pairs is continuous, it's amplitude can not instantly drop to zero at the boundary of a superconductor. Considering an interface between a superconductor (S) and a normal metal (N) both sides are affected. Close to the boundary the superconducting order parameter is suppressed in S and superconducting correlations are induced into N [72]. If a normal metal layer sandwiched between two superconducting electrodes is sufficiently thin, it is able to support a super-current which

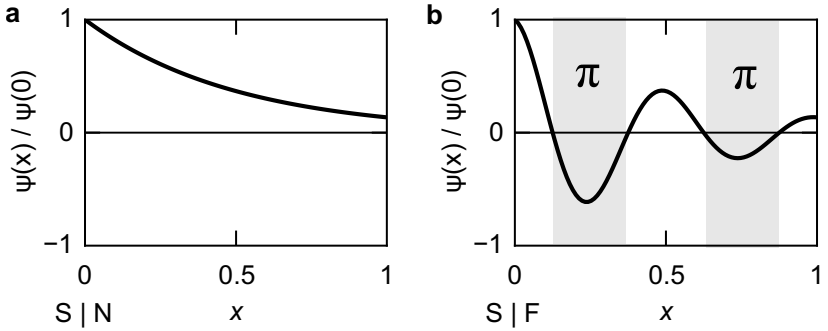

Figure 1.11 Order parameter Ψ decaying into a metal as a function of the distance x from the superconductor | metal interface due to proximity effect **a** monotonic decay into a normal metal (N) and **b** oscillatory decay in a ferromagnet (F) with regions where, compared to the bulk value, a relative phase shift of π occurs

satisfies the Josephson relations. The decay of the bulk superconducting order parameter Ψ_{bulk} into the normal metal (N) is usually exponential (Fig. 1.11a)

$$\Psi(x) = \Psi(0)\, e^{-\frac{x}{\xi_{\mathrm{N}}}} \tag{1.43}$$

with a decay constant ξ_{N}, also called coherence length. The microscopic origin for the proximity effect has been described by Andreev reflection [73–75], which explains how Cooper pairs are converted into a pair of a single electron and a hole at an SN interface and vice versa. If an electron from the N layer with an energy within the superconducting gap hits the interface to the S layer it can only be transmitted as a Cooper pair. The conservation of charge, spin and momentum results in the reflection of a hole back into the N layer.

This picture needs to be extended if ferromagnetic metals (F) are considered. In a conventional superconductor a Cooper pair consists of two electrons with opposite spin and momentum $(+\boldsymbol{k}\uparrow, -\boldsymbol{k}\downarrow)$ and zero net momentum. In the absence of currents and electric and magnetic fields, the order parameter in such a system is isotropic and constant in

magnitude. The additional presence of a magnetic exchange field can cause a spin dependent shift of electron energies and momenta at the Fermi energy. Stable solutions for this situation that still allow pairing have been found by Fulde and Ferrel [76] and Larkin and Ovchinnikov [77]. Such an FFLO state is characterized by spatial oscillations of the superconducting order parameter where a phase change of π occurs at the nodes. The energy difference between the two spin directions leads to a finite net momentum of the Cooper pairs accompanied by a variation of the order parameter [78]. The two electrons of a Cooper pair experience an opposite shift of the potential energy by $\pm E_{\mathrm{ex}}$, depending on their individual spin orientation. Due to energy conservation the kinetic energy is balanced accordingly. One electron gains energy and increases its momentum by

$$\delta k \sim \frac{E_{\mathrm{ex}}}{v_{\mathrm{F}}} \tag{1.44}$$

and the other one compensates the energy loss by decreasing the magnitude of its momentum by $-\delta k$. Since the momentum vectors of the two pair electrons oppose each other they acquire a collective momentum of $2\delta k$ or $-2\delta k$ depending on the two possible configurations for the spin singlet of the Cooper pair ($\uparrow\downarrow$, $\downarrow\uparrow$). The finite momentum enters into the phase term of the wavefunction. Both spin configurations are realized and the superposition of their order parameters yields a collective wavefunction $\Psi(x)$ that oscillates with the position coordinate x (Fig. 1.11b),

$$\begin{aligned}\Psi(x) &\sim \Psi_{\uparrow\downarrow}(x) + \Psi_{\downarrow\uparrow}(x) \\ &\sim e^{i(\varphi(t)+2\delta k x)} + e^{i(\varphi(t)-2\delta k x)} \\ &\sim \cos(2\delta k x).\end{aligned} \tag{1.45}$$

At a superconductor (S) | ferromagnet (F) interface the Cooper pairs diffuse into F with a decaying order parameter caused by pair breaking due to magnetic and impurity scattering. Superimposed, the exchange field in the ferromagnetic metal causes FFLO like oscillations with nodes where the phase changes by π [78]. Both effects can be combined in a

complex coherence length

$$\frac{1}{\xi_{\mathrm{F}}} = \frac{1}{\xi_{\mathrm{F1}}} + i\,\frac{1}{\xi_{\mathrm{F2}}} \tag{1.46}$$

which is composed from the order parameter decay length ξ_{F1} and the oscillatory period $2\pi\xi_{\mathrm{F2}}$ which enters into the imaginary part. They are defined as

$$\xi_{\mathrm{F1,F2}} = \sqrt{\frac{\hbar D}{\sqrt{(\pi \mathrm{k_B} T)^2 + E_{\mathrm{ex}}^2} \pm \pi \mathrm{k_B} T}}. \tag{1.47}$$

A sketch of an S | N and an S | F interface where the proximity effect occurs with real or complex values, respectively, is shown in Fig. 1.11. For $T = 0$ or large exchange energies and negligible magnetic scattering in a diffusive magnetic layer the two characteristic lengths become equal [79]

$$\xi_{\mathrm{F1}} = \xi_{\mathrm{F2}} = \sqrt{\frac{\hbar D}{E_{\mathrm{ex}}}} \tag{1.48}$$

where D is the electron diffusion coefficient.

The oscillating order parameter at SF interfaces also influences the Josephson effect, e.g. at SFS junctions. Depending on the thickness d_{F} of the F barrier the Josephson critical current oscillates and reduces to zero when it changes sign. Buzdin theoretically predicted the oscillatory behaviour of the critical current in the clean limit [80] and later also for diffusive junctions [81]. If d_{F} is not too large the oscillating wavefunctions that penetrate F from the two S electrodes overlap. Depending on the thickness d_{F} their superposition leads to a ground state that couples the bulk electrodes either with the same phase or with a phase difference of π.

Spin Flip

The first theoretical proposal for a π Josephson junction was based on a tunnel barrier that contains magnetic impurities and originates in 1977 [62]. It was claimed that magnetic impurities in the barrier can flip

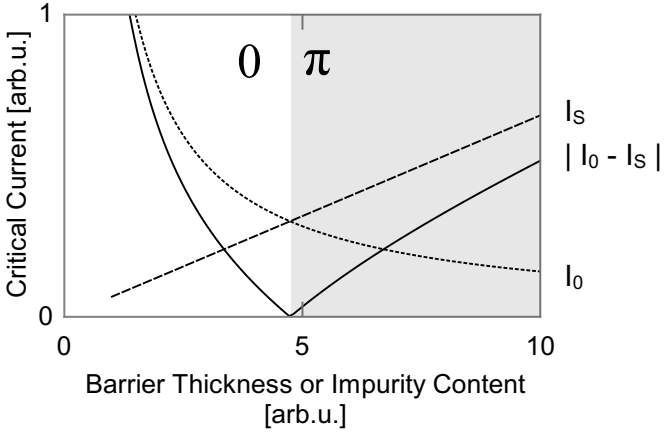

Figure 1.12 Qualitative sketch of critical current contributions through a Josephson junction with FI barrier in dependence on barrier thickness or content of magnetic impurities. The current I_S experiences a spin-flip and the current I_0 doesn't. The sign of the difference of these two currents promotes a ground state phase difference of either 0 or π.

the spin of electrons during the tunnelling process. A π coupling was expected to arise if the transmission probability with a spin-flip becomes the dominant conductance channel.

In a very simple picture (Fig. 1.12) the total current is composed of two parts, one where a quasi particle experiences a spin-flip I_S and another where it crosses the barrier without a spin flip event I_0. The current I_0 decreases exponentially with the barrier thickness d or is suppressed similarly by an increased density of magnetic impurities δ. The spin-flip current I_S however depends on the scattering probability which rises linearly with the number of impurities in the barrier, which is proportional to d and δ. A phase shift of π in the ground state can occur if I_S exceeds I_0 [62].

Over the years ferromagnetic insulating and ferromagnetic semiconducting barriers have been investigated as possible candidates for a π junction [82, 83]. Despite the various theoretical predictions only a few experimental hints have been published. In a S(FI)S junction with a

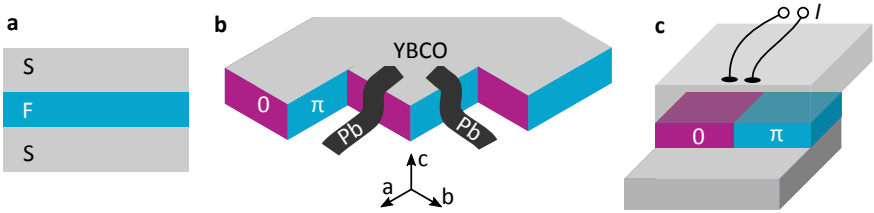

Figure 1.13 Experimental realisations of π Josephson junctions by **a** ferromagnetic thin film junction, **b** YBCO facet junction or **c** inhomogeneous current injection into the barrier creating steps of π in the Josephson phase [85].

ferromagnetic insulator (FI) a temperature induced excess of tunnelling with a phase shift of π has been reported [84].

1.6.4 Experimental Realization of π Junctions

Since the first theoretical prediction for the occurrence of a ground state phase shift of π in Josephson junctions quite a few experiments successfully demonstrated this coupling in reality (Fig. 1.13). Already the fabrication of conventional 0 Josephson junctions with high quality is only possible for a limited number of materials. To manufacture magnetic junctions the requirement for a precise control over thickness, roughness and magnetism poses additional challenges to the experimentalist. Additionally the complexity of experiments is enhanced by the fact that the detection of a π junction requires extra effort (sec. 1.6.2).

So the first experimental proof for a ground state phase shift of π between the electrodes of a Josephson junction came from the community of high T_c superconductivity [86, 87]. In Yttrium-Barium-Copper-Oxide (YBCO) crystals the superconducting order parameter is not isotropic but d-wave like. In the experiment Pb contacts were attached to the facets of the YBCO crystal in the direction of the a- and b-axis, respectively. The two Josephson junctions formed where contacted in parallel and it was shown that a phase shift of π occurs between them. As a result one junction is a conventional 0 JJ and the other a π JJ.

In 2001 the π coupling was also found in planar low T_c junctions.

Temperature induced transitions between 0 and π were demonstrated for Nb | NiCu | Nb structures [88], which belong to the class of superconductor | ferromagnet | superconductor (SFS) junctions. The use of $Ni_\delta Cu_{1-\delta}$ alloys allows to change the magnetism of the barrier by controlling the Ni content δ. For $\delta \geq 0.44$ ferromagnetism establishes and the magnetic moment linearly increases with the Ni concentration. A challenge for the measurement setup is the absence of an insulating barrier in SFS which leads to a tiny normal resistance of the junction and requires the sensing of nV. To trace the $I(V)$ curve and identify the critical current SQUID-based amplifiers are used.

Later the F-layer thickness induced transition into the π state was experimentally demonstrated on superconductor | insulator | ferromagnet | superconductor (SIFS) junctions [89]. These samples consisted of Nb electrodes (S) which embrace a double layer made from an aluminium oxide tunnel barrier (I) and an adjacent layer of PdNi (F). A series of junctions with different thickness d_F of the ferromagnetic F-layer was fabricated and electrically characterized. With increasing d_F the critical current first ceases to zero and recovers again. The vanishing critical current indicates the layer thickness where the critical current changes sign and marks the transition between 0 and π coupling. The alloy PdNi becomes an itinerant ferromagnet starting at low Ni concentrations (12 % in the mentioned experiment). Compared to SFS structures the additional layer of insulating Al_2O_3 scarcely affects the order parameter oscillation periode and advent of the π coupling. However, it significantly facilitates the measurement, because it shifts the normal resistance and relevant voltages into a regime where they are easy to detect. Additionally the maximum critical current is limited which otherwise not only varies by orders of magnitude with d_F but can also take huge values if the magnetic pair breaking becomes negligible for thin F layers in SFS structures.

Several publications have confirmed and studied planar π junctions with ferromagnetic barriers covering the range from strong elemental ferromagnets to diluted and weak magnetic alloys. Furthermore they differ in layer sequence, material and composition. However, the experiments are consistent, fulfill the theoretical expectations and provide insight into the complex magnetic coherence length ξ_F and transport phenomena. A π coupling has been reported for barriers, formed with

pure 3d transition metals like Fe [90], Co [91] and Ni [91–93]. In these materials a strong exchange interaction occurs which causes short order parameter oscillation periods in the range of Å to nm. Furthermore diluted ferromagnetic alloys like NiCu [67,88,94,95] and PdNi [89,96,97] have been used successfully. Some experiments employ additional insulating tunnel barriers or multilayers that weaken the magnetism, but these configurations are not discussed any further here.

The existing experiments suggest that for the fabrication of π junctions a tradeoff between large critical current densities j_c and high normal resistance R_N in the voltage state needs to be made (comparison in Tab. 3.2). In contrast to conventional non-magnetic Josephson junctions the device parameter range is rather limited and especially restricted to low values of $I_c R_N$. To achieve equivalent performance and compatibility to conventional Josephson junctions the current junction designs seem inappropriate. Some ideas exist to increase the critical current density of π junctions. The use of a clean ferromagnet with small exchange energy would have the advantage of a long decay length ξ_{F1} which potentially also leads to large critical currents in the π state. A work on Ni_3Al barriers indicates the advantage of such clean materials in SIFS junctions [98]. Nonetheless the reliable fabrication of the desired π junction might turn out to be difficult due to a thick magnetic dead layer and rather short oscillation period of the superconducting order parameter.

2 Fabrication and Characterisation of Josephson Junctions

All thin film devices which were investigated in the frame of this thesis have been fabricated at the Technical Faculty of the Christian-Albrechts-University of Kiel. The facilities include all the necessary equipment for deposition, etching, lithography, monitoring and processing of the junctions. A cleanroom on campus provides the environment for lithography and wet-chemical treatments. The description of technology represents the local methods and machine configurations and is not a complete overview over the field. However, if not stated otherwise the approaches follow common community practice.

Fabrication parameters and instructions for specific Josephson junctions are mentioned along with the experimental data (Chapter 3). A step by step fabrication recipe and detailed machine parameters for the Josephson junctions can also be found in Appendix A.2.

Thin Film Technology

Layers with a thickness below a few micrometers are called thin films. Applied as coating on the surface of objects, such layers can provide mechanical and chemical protection from environmental impact. Dielectric (multi-)layers with thickness in the order of the impinging radiation become optically active and can form high quality mirrors with reflection coefficients very close to unity. For other applications like in microelectronics the thin film technology allows high integration of functional interfaces. While a controlled miniaturization of lateral dimensions down to the nanometer scale requires greatest effort, the layer thickness can

be adjusted with sub-nanometer resolution. The availability of nanometer scale barriers makes thin film devices also interesting for tunneling experiments. A grid containing many junctions can be fabricated on one wafer. So lots of structures that may differ in geometry by design, are produced within one run.

The Josephson effect occurs at the interface between two superconductors. Therefore the controlled fabrication of Josephson junctions (JJ) requires a precise control of the interface morphology, layer materials and dimensions. As a rule of thumb, the electrode layers do resemble bulk superconducting properties and keep them under not too large magnetic fields if they are thicker than twice the magnetic penetration depth λ_L. If composed by several sublayers, the individual layers should not be smaller than the superconducting coherence length ξ_S. Otherwise superconducting gap voltages may be reduced. For sputter deposited Nb thin films the coherence length is around $\xi_S = 40\,\text{nm}$. With increasing layer thickness the polycrystalline growth of Nb results in a surface roughness which is unfavourable for JJ fabrication. The careful adjustment of thin film fabrication parameters and design is therefore essential for the junction performance.

2.1 Sample Preparation Technology

The following account covers the different techniques, machines and materials that were used for the fabrication of thin film junctions. The samples are based on crystalline Si substrates that are covered with a thermally grown oxide of about 400 nm thickness. A Leybold Univex 450b sputtering system (Fig. 2.1) provides 8 sputter deposition stages equipped with circular $4''$ targets, an oxidisation chamber, a sample storage chamber and a load lock.

The plasma processes for the growth and etching of thin films on the wafer are conducted in vacuum. At ambient pressure (1013 mbar) an effective plasma generation and particle transport from and to the substrate is not possible. Also for a controlled and clean film growth the incorporation of impurities and oxidisation processes have to be minimized. To reduce the gas particle density in a volume different vacuum pumps exist [99]. A high vacuum, with pressures as low as

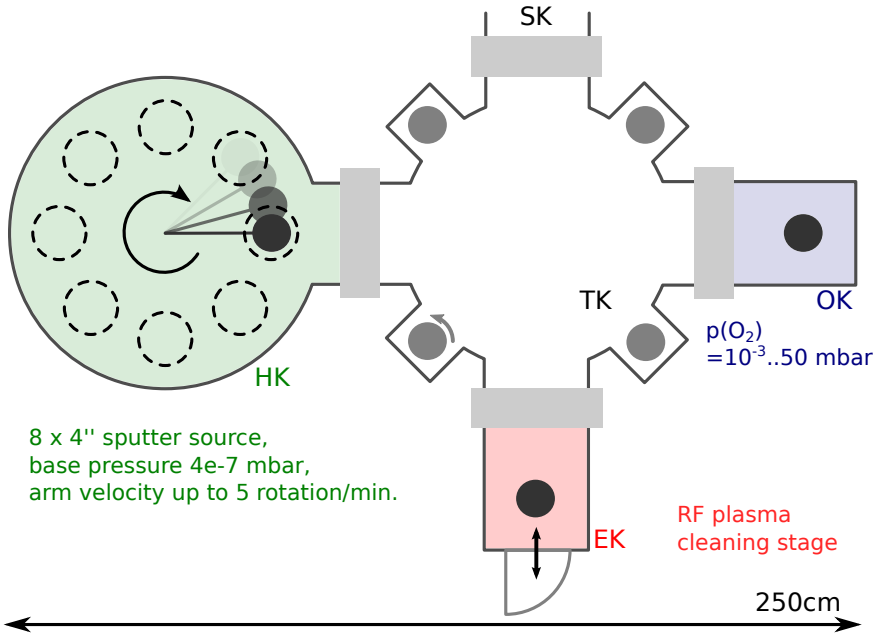

Figure 2.1 Schematic top view onto the Univex 450B sputtering system showing the different vacuum chambers connected by gate valves. **HK** main sputter chamber with 8 sputter sources and a rotation arm for substrate positioning **EK** load lock for sample holder loading **OK** oxidisation chamber **TK** storage chamber with rotation stage **SK** separate sputter chamber

4×10^{-7} mbar, is created in the Univex by cascades, consisting of a roughening pump which creates a vacuum in the sub mbar range and a turbo molecular pump.

2.1.1 Sputter deposition

The term *sputtering* describes a process where a particle hits the surface of a solid material (target), transfers momentum to the lattice atoms and makes them overcome the binding energy of the bulk. The released particles may settle on another surface and contribute to the growth of

a thin film. A directed acceleration of particles can be achieved by ions that are generated and accelerated in a plasma by means of an electric field. Usually an inert noble gas like Argon (Ar) is used as a process gas and the reactor volume is evacuated to avoid contamination and provide suitable conditions for the plasma and particle propagation. The physical effect to eject material into the gas phase is used in various processes.

For deposition purpose the source material (target) is mounted into a sputtering gun facing the substrate that shall be coated. A negative voltage applied at the sputter target attracts cations from a plasma. The kinetic energy of the cations vaporizes surface atoms from the target which then travel through the vacuum and may be deposited on the substrate surface. The same electric field that drives the cations, also accelerates free electrons which provide ionization events and stabilize the plasma. An array of magnets in the sputter gun creates a dome of magnetic field lines that forces the electrons on helical path which leads to an increased ionisation yield and finally a higher sputter rate. A backside water cooling removes heat from the target which is dissipated during the sputtering process. Two modes of operation are common. For conductive targets a negative DC voltage may directly be applied to the sputter target. When the target is not conductive a capacitively coupled radio frequency (RF) power supply is used instead. Subject to a proper matching of the impedance (provided by an LC matching circuit) the RF of 13.56 MHz creates a plasma in the vicinity of the target. The lightweight free electrons in the plasma have a higher mobility than the heavy ions and are absorbed by the surrounding surfaces. If they hit the grounded chamber walls they are lost for the sputter process. If they accumulate at the isolated target however, they built up a negative charge that attracts ions from the plasma and start the sputtering process. The sputtered material can condense at the surface of substrates that are placed in the vicinity of the target. By the adjustment of gas flow, chamber pressure, sputter power and substrate temperature different deposition conditions can be achieved. Especially the deposition rate and the energy of the sputtered target atoms have to be adapted to the particular deposition task. Typical sputter rates are up to a few nm/s.

The layer growth and rate are reproducible, provided that the deposition conditions like the geometry between target and sample, the

vacuum, the electrical parameters and the substrate temperature are kept constant. Therefore an in-situ monitoring of the thickness is not used. Instead a calibration after modifications or extensive use is performed. Chunks with dimensions of roughly $15 \times 5\,\mathrm{mm}^2$ are placed on the substrate holder and covered with material. The resulting layer thickness may be determined with X-Ray diffraction (XRR, cp. section 2.1.5) or anodization spectroscopy (cp. sec. 2.1.3). Alternatively lithographically defined layer edges may be scanned with an atomic force microscope or a profilometer.

2.1.2 Lithography

Most processing tools have an effect on the whole wafer surface. To pattern structures and restrict the impact of a processing step to specific areas of a substrate a protective polymer (resist) can be used. The liquid polymer is placed in the centre of the substrate and homogeneously spread by rotating the wafer in a spin coater. By selective irradiation with ultraviolet light (UV) through a mask it is possible to discriminates two types of regions. At the end of the whole process only one region will be covered with resist. The light modifies the polymers either by breaking molecular chains and therefore weakening the structure (positive resist) or by providing energy for cross-linking which enhances the robustness of the film (negative resist). A subsequent bath in a development liquid clears the previously defined areas from resist. The procedure borrows its name lithography (greek for “write with stone”) from the old technique of producing print copies with the help of a carved stone relief. The achievable resolution scales with the wavelength used. The technology described above is sufficient for structures with dimensions larger than one micrometer, like for this thesis. The state of the art industry technology however uses extreme ultraviolet light sources 13.2 nm which require mirror based optics and sophisticated irradiation processes to achieve smallest feature sizes of less than 100 nm.

For small areas with limited complexity and rapid prototyping a different approach provides a very high spatial resolution. In an electron beam lithography process the chemical resist modifications are written with the beam of an electron microscope.

2.1.3 Anodic Oxidisation

The electrolytic passivation of a metal surface by the transformation into its oxide is called *Anodizing*. Besides being used as a surface treatment for protection and colorization, it has become a successful method to define the active junction area of Nb-based Josephson junctions and insulate the stacked thin film electrodes from each other. After the deposition of the trilayer (bottom electrode | barrier | electrode capping) on the wafer, the junction area is protected by resist. Subsequently a conductive contact to the layer is made. Care should be taken that the layer is electrically insulated from the bulk wafer. Then the wafer and a gold-passivated counter electrode are connected as anode and cathode, respectively, and placed in an electrolyte bath. A common electrolyte [100] consists of

156 g	ammonium pentaborate,
1124 ml	ethylene glycol and
760 ml	water.

When a current is applied, the metal surface is transformed into an oxide. The oxidisation process starts at the metal surface and moves into the material. For a constant current, the voltage V rises with increasing oxide thickness at a rate $\mathrm{d}V/\mathrm{d}t$ that depends on the material at the anodization front which propagates into the layer. Both quantities plotted against each other provide a fingerprint of the consumed layers yielding information about thickness and materials. Extensive studies of these electrical anodization profiles [101–103] identified prerequisites for high quality tunneling barriers. Good junctions with aluminium oxide barriers show a distinct double peak at the tunnel barrier.

Parallel current paths, as occurring from electrical connections between the thin film structures and the bulk wafer, may drastically suppress the anodization process. Also some materials, like Si and Fe, form an effective barrier layer and prevent a further propagation of the oxide.

2.1.4 (Reactive) Ion Beam Etching

The mechanism of material ablation by sputtering can be used to remove surface layers from a substrate. In ion beam etching (IBE) systems, a beam of Ar atoms is accelerated onto the substrate surface and provides

the kinetic energy for the process. To avoid redeposition at steps and sidewalls of resist structures, the incident angle is tilted by e.g. 30° from the surface normal and the sample is rotating on its mount. In the beam source Ar is ionised to form a plasma, accelerated by an electrical field and then actively neutralized by travelling through a cloud of electrons. It is possible to get information about the etched species by using a secondary ion mass spectrometer (SIMS) which analyses the gas constituents in the chamber. Besides giving information about the layer materials it can be used as an end-point-detection for the etching process. The ion beam etching is characterized by the physical ablation of material by ion bombardment. A selectivity for specific materials can be introduced into the etching process by the addition of a reactive component as done by reactive ion etching (RIE). In this process a precursor gas, usually containing F or Cl compounds, is dissociated in a plasma and guided to the substrate. Ideally the ionisation of the reactant gas occurs in a separate chamber from where the radicals shower onto the substrate and etch chemically with very low kinetic energy leading to little surface damage.

2.1.5 X-Ray Diffraction

X-Ray Diffraction (XRD) is a tool to obtain detailed information about the bulk structure of crystalline and polycrystalline samples and in particular the layer thickness. The X-Ray reflectivity (XRR) mode is well suited to measure the thickness of layers in the range between 10 nm and 100 nm. It works by exposing the sample to a collimated beam of monochromatic X-Rays under small incident angles and counting the specular reflected photons with a detector in a $\theta/2\theta$ alignment (Bragg geometry) [104].

The elastic scattering of photons (and subatomic particles) at a regular lattice, like a crystal, can be understood by the superposition of all possible scattering events. If the wavefunctions which describe the different path of the particle interfere constructively for a given direction, there is a finite probability for this scattering event. No scattering occurs in directions where the wave amplitudes cancel. For a regular crystal lattice with a 3-dimensional structure and lattice plane spacing d the

scattering angles θ_n follow Bragg's law [105]

$$n\lambda = 2d \sin\theta_n \tag{2.1}$$

for a photon wavelength λ and n being the integer wavenumber difference between two paths via neighbouring lattice planes. If many planes contribute to the process the scattering angles are defined sharp and appear as peaks in a plot of intensity versus deflection angle. The other extreme case is a single layer grown on a substrate where only the two interfaces, air | layer and layer | substrate, participate as scattering planes. An intensity versus scattering angle 2θ plot is shown in the experimental section (Fig. 3.16). Superimposed over a background of incoherently scattered photons a periodic modulation is visible with local minima at θ_n where destructive interference suppresses scattering. The minima also follow from (2.1) with $n \in \{ {}^1\!/_2, {}^3\!/_2, {}^5\!/_2, \dots \}$. From the data the spacing of the reflective interfaces can be determined, which is equivalent to the layer thickness. Instead of finding a series $(n_0, n_0+1, \dots, n_0+N)$ that satisfies (2.1) for the angles $(\theta_0, \dots, \theta_N)$ and results in a constant d, it is useful to rearrange the equation and work with the constant oscillation period $\Delta 2\theta$ instead. The difference between two Bragg peaks with n_i and n_j which satisfy (2.1) is

$$\begin{aligned}
& (n_\mathrm{i} - n_\mathrm{j})\ \lambda = 2d\ (\sin\theta_\mathrm{i} - \sin\theta_\mathrm{j}) \\
\Rightarrow \qquad & \Delta n\ \lambda = 2d\ \frac{\pi}{180^\circ}\ (\theta_\mathrm{i} - \theta_\mathrm{j}) \\
\Rightarrow \qquad & d = \frac{180^\circ \cdot \lambda}{\pi}\ \frac{\Delta n}{(2\theta_\mathrm{i} - 2\theta_\mathrm{j})} \\
\Rightarrow \qquad & d = 8.8\,\mathrm{nm} \frac{\Delta n}{\Delta(2\theta)/^\circ}
\end{aligned} \tag{2.2}$$

were a first order Taylor expansion has been used and the transition wavelength Cu-K_α with $\lambda = 0.154\,\mathrm{nm}$ that passes the monochromator of the X-Ray source. The error for the linearisation of sin is negligible for experimentally interesting angles below 5°.

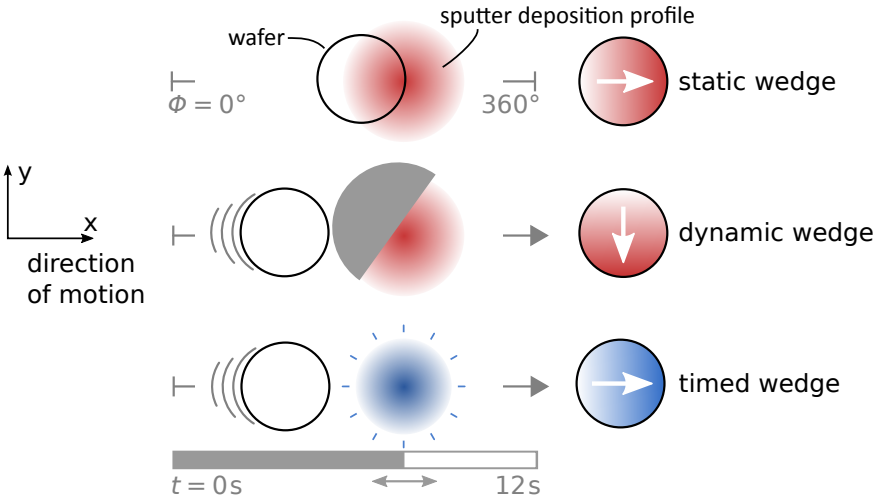

Figure 2.2 Wedge deposition techniques (left) and resulting directions of the thickness gradient on the wafer (right). The circular path of the wafer in the deposition chamber is shown as a straight line. Deposition of a **static wedge** by an off-centered placement of the wafer with respect to the target, a **dynamic wedge** by a constantly moving wafer which passes a target with a shaped deposition profile and a **timed wedge** by a constantly moving wafer, the target power supply is deactivated when the wafer is in the sputter region.

2.2 Thickness Gradients in Sputtered Films

In the fabrication of microelectronic devices and circuits it is usually crucial to have well defined, reproducible and homogeneous process conditions across the wafer. The design of a sputter source is therefore optimised to provide a uniform deposition rate. So geometrical variations of devices across a wafer are restricted to adjustments of the lateral dimensions, as defined by lithography. Difference in the layer thickness across a wafer are uncommon within a single fabrication step of standard deposition processes.

For this work however, a series of planar Josephson junctions (cp. A.1) with gradually changing barrier layer properties had to be made. One

possibility to achieve layers with different thicknesses along the surface normal is to process several wafers and change the barrier thickness between them. This approach might introduce errors due to run-to-run variations in the processing steps. Another method is to realise a thickness wedge of the deposited layer across the wafer. If the deposition rate changes monotonically along a line across the wafer, a series of junctions with systematically varying layer thickness can be fabricated. These allow the study of thickness induced effects on the device behaviour. For the Leybold Univex 450b cluster deposition system several techniques were implemented to deposit material wedges with different directions on the sample holder (Fig. 2.2). Two directions, along and perpendicular to the direction of substrate motion were realised. The different techniques are explained below.

The possibility to combine wedges from different materials with perpendicular orientation to create alloy libraries with different thickness and composition on a single wafer are described in section 2.3.

Static Wedge

The circular 4 inch (10 cm) sputter sources provide a constant deposition rate only within a radius of about 2.5 cm around the centre. Further out the sputter yield decreases linearly by about 10 % points every 1 cm and the last 10 % points slowly fade out. Therefore a drop of the layer thickness towards the edges of a 4 inch wafer by about 25 % cannot be avoided with a static deposition.

To create a thickness wedges in a planetary type system with fixed sputter sources (sec. 2.1.1) the substrate may be shifted sideways out of the target centre. The substrate's degree of freedom is restricted to a one dimensional motion where the center of the substrate holder follows a circular path with a radius $r = 27\,\mathrm{cm}$. A change of the holder position angle leads to a lateral shift according to $0.47\,^{\mathrm{cm}}/^{\circ}$. Stripe like samples can be positioned along the radial direction of the target deposition profile to deposit material as a wedge. For more square shaped samples the thickness gradient direction is not constant over the wafer but rotates according to the radial distribution of the deposition rate. To reduce the curvature in a static deposition, the wafer can be shifted further off the center axis of the target.

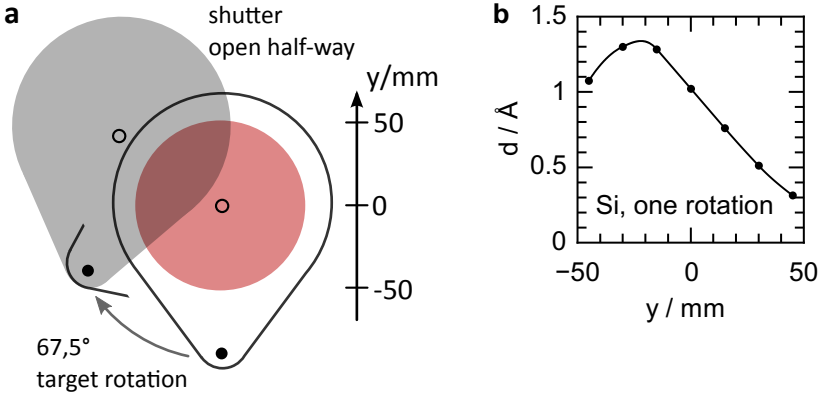

Figure 2.3 Rotation wedge with quasi linear rate gradient achieved by **a** shutter rotated and half-open. **b** Resulting deposition profile of Si target (100 W, 5 min^{-1}) perpendicular to the direction of substrate motion.

To manipulate the alignment of the thickness wedge on the substrate the sample can be be transferred to a rotation stage. Thus layer stacks with different directions and magnitudes of the thickness gradient can be formed consecutively.

Dynamic Wedge

The static deposition from 4 inch targets onto 4 inch wafers results in a significant drop of the rate towards the wafer edge. An additional smoothing of a layer during sputter deposition can be achieved when the substrate is moved straight through the region below a sputter target with a constant velocity. Along lines parallel to the direction of motion the thickness of the collected material is homogenised because every point on the substrate sees the same sputtering conditions just with a time delay. This method leads to a layer thickness with a parabolic shape along the direction of motion. The profile is symmetric, centered on the sample holder and shows a 15 % increase at a distance of 5 cm from the middle. The rate increase is attributed to transient plasma effects at the edge of the sample holder due to changes in the electric field configuration by the presence of the sample holder. The effect was similarly observed

for sample holder rotations in the chamber at frequencies of $1\,\mathrm{min}^{-1}$ and $5\,\mathrm{min}^{-1}$.

The deposition with rotation can also be used to create a wedge perpendicular to the direction of substrate motion. A geometric modification of the target shutter allows to manipulate the circular deposition profile. The partial coverage of the sputter target with a suitably shaped shutter can provide a monotonic, quasi linear gradient in the layer thickness along the direction perpendicular to the wafer motion (Fig. 2.3). To achieve the presented thickness profile the target was rotated by 67.5° and the attached shutter was opened half way.

Timed wedge

A wedge along the x direction (Fig. 2.2) can also be deposited when the substrate is moved into the sputter region of a target and the target power supply is subsequently deactivated. At this moment the leading edge of the sample has collected more material than the trailing edge which causes a thickness gradient across the wafer. Figure 2.4 shows a simulation process to estimate the layer thickness distribution. Calibration data for the radial dependence of the rate r of a circular target (Fe, 50 W, 20 sccm Ar) was acquired by deposition on lithographically structured wafer pieces that were placed along a radial line of the deposition zone. The calibration pieces were then analysed with a profilometer resulting in the layer thickness profile. A linear extrapolation of the data to zero resulted in a trendline that served as the basis for the visualisation of the 2-dimensional rate profile. The coordinate system (x,y) is centered at the Fe sputter target and the x-axis points in the direction of substrate motion. A numerical integration of the rate profile according to

$$d(X,Y) = \frac{d_{\mathrm{calib.}}(x',y')}{\sum\limits_{x<x'} r(x,y')} \cdot \sum_{x<X} r(x,Y) \tag{2.3}$$

results in a map of the layer thickness d, collected during the horizontal movement of the substrate into the sputter region of the target. The coordinate (X,Y) denotes the position of a point at the moment of the target shutdown and $d_{\mathrm{calib.}}$ is the measured thickness from a calibration point (x',y') of an actual timed wedge deposition sequence.

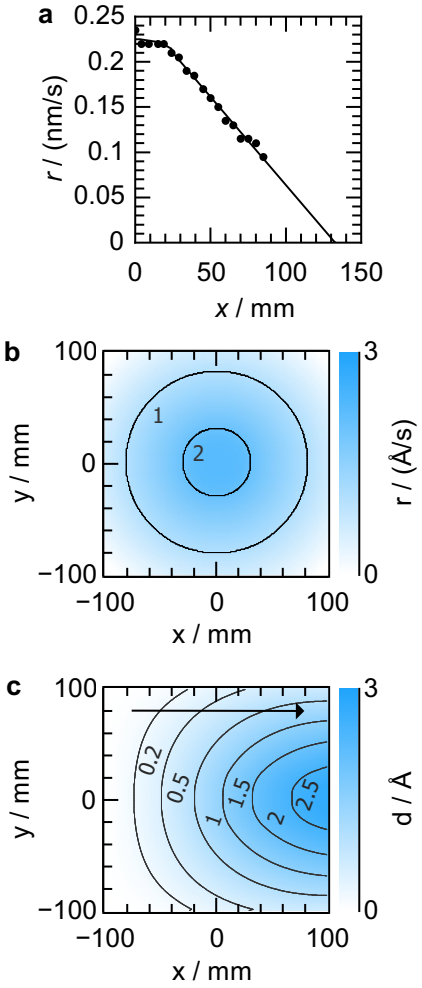

Figure 2.4 Nummerical simulation of the film thickness produced by the timed wedge approach. **a** Measurements of the deposition rate r of the circular Fe sputter target (50 W, 20 sccm Ar) were extrapolated and allowed to visualize **b** a 2D map of the Fe sputter rate in coordinates relative to the center of the sputter target which serves as basis for **c** the Fe layer thickness according to (2.3). The arrow indicates the direction of wafer motion.

The Univex 450B control unit alone was considered inappropriate for this procedure. So an external power supply circuit was used (App. C). The Univex control unit only provides a constant circular motion of the sample holder arm and a defined Ar gas atmosphere. When the holder passes a certain reference position in the chamber a switch is activated. This event triggers a timer circuit which powers the target for a fixed period of time τ. By variations of τ the shape of the thickness wedge on the wafer can be controlled. The angular position φ of the sample holder arm at the moment of target shutdown translates into a time interval by

$$\tau = \frac{\varphi/^\circ + 3}{360} \cdot \hat{t} \tag{2.4}$$

with the arm rotation periode $\hat{t}$, which is 12 s for all samples in this thesis. The layer thickness may be scaled by the target power and the number of repetitions.

2.3 Combinatorial Sputtering with Orthogonal Parameter Gradients

Parts of this section have been published in [106] and are presented in agreement to copyright regulations of Applied Physics A (Springer).

Experiments that are intended to study samples with respect to variations of two design parameters can profit from an *orthogonal gradient* approach in fabrication. For example, if the thickness of a layer (A) changes in a certain direction the lines of constant thickness are aligned perpendicular to this gradient. A second layer (B) is then deposited to exhibit a thickness gradient along the lines of constant thickness for A. As a result the influence of a material property A(B) can be studied independent by the other parameter by following lines of constant B(A). On a single wafer the non collinear wedges provide an array for the independent and systematic study of thickness effects for both layer A and B. In reality it is likely that the individual gradients change in magnitude and direction accross the wafer. Although the approach only requires a non-parallel orientation of the two gradients, the angle should be close to perpendicular for a feasible experimental realisation.

Combinatorial Sputtering

The deposition of alloys can occur from stoichiometric targets that contain the elements in the desired portion. If the quantities are not known in advance or a variety of compositions shall be investigated it is useful to deposit the individual elements from separate sources. On the substrate they will mix in-situ and may form the desired alloy. The probably most intuitive deposition technique is the off-axis sputtering from several targets. Multiple sputter sources which all aim at the substrate surface are operated at the same time and the different materials may intimately mix before settling at the surface. This geometry has already been used 50 years ago with evaporation sources [107] and later for sputter deposition [108]. By design the alignment of target and substrate planes is tilted which leads to thickness wedges of the individually deposited materials and finally to a wafer with varying layer composition and thickness. This approach is well suited to create an alloy library which covers a wide range of material ratios. But it also restricts the chamber application due to the special target alignment.

Alloy Deposition from Individual Targets

With the emergence of multi source sputtering systems a planetary type chamber geometry (section 2.1.1) became common. Trimmed for homogeneous layer growth over the wafer the top down alignment with facing target and substrate surface planes only allows the deposition from one target at a time. In this alignment, alloys may be formed by the subsequent deposition of the constituents in alternating layers of sub-monolayer thickness. To produce alloys with a thickness of several nanometers quite a number of layers is necessary. A series of continuous revolutions with a constant velocity can be combined with wedge deposition techniques (cp. 2.2). During a complete cycle of 360° one thin layer of each constituent is deposited. Without manipulations of the targets an alloy with rather homogeneous thickness and composition is deposited across the wafer.

Additional complexity is introduced if an alloy library shall be fabricated. A perpendicular gradient approach can lead to an alloy layer which exhibits non-collinear gradients of thickness and composition. The

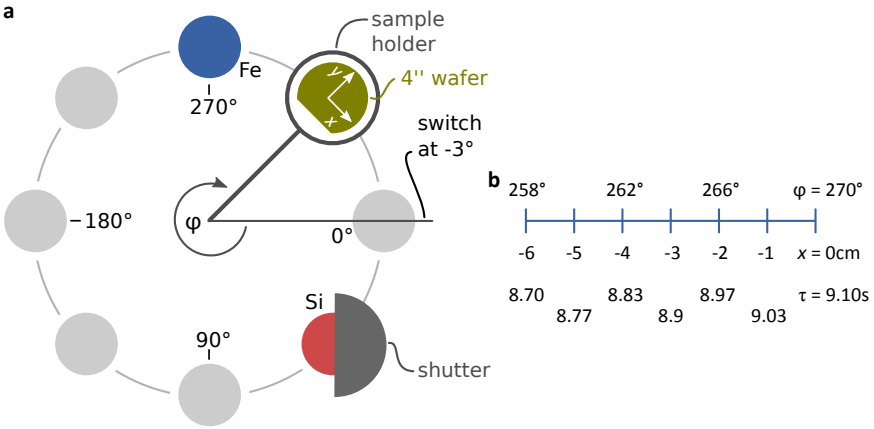

Figure 2.5 Combinatorial sputtering sequence **a** top-view of the sputtering chamber with the active elements during the clockwise sample movement **b** relation between sample holder angle φ, target position x and power supply timing τ

wedge deposition is introduced into the steady motion of the substrate so that different materials are deposited in an alternating fashion. A thickness wedge perpendicular to the direction of motion can be achieved by a dynamic wedge with a suitably shaped deposition mask between target and substrate (sec. 2.2). A mechanical solution that uses only this wedge deposition method and rotates the sample between the deposition of the different materials by a desired angle has been published [109]. However, structural modifications are necessary in the vacuum chamber which interfere with the standard machine operation modes. We avoid a mechanical solution by the implementation of a second wedge direction. The timed wedge approach breaks the rotation symmetry of the set-up and leads to a thickness gradient along the direction of motion.

A description of the combinatorial deposition process with non-parallel gradients follows. The alloy $Si_{1-\delta}Fe_{\delta}$ has been deposited by co-sputtering from a Si and a Fe target. For fabrication, the Si target shutter[1] is half open and the target is rotated by 67.5° leading to a dynamic wedge

[1] AJA 4 inch sputter deposition head

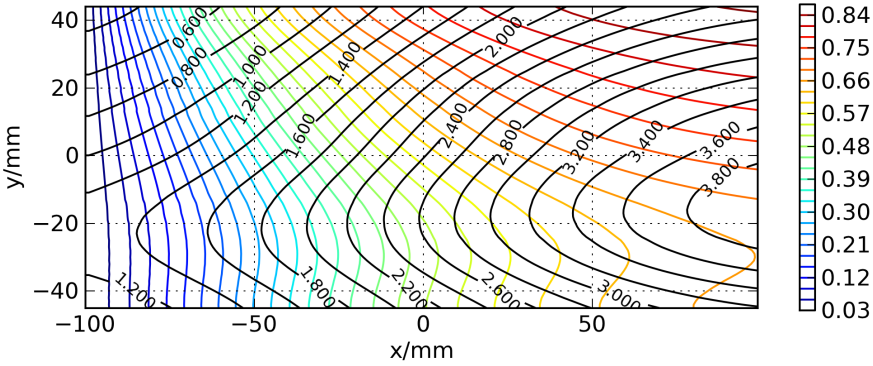

Figure 2.6 Calculated map of $Si_{1-\delta}Fe_{\delta}$ film parameters showing lines of constant thickness (black) and lines of constant Fe content (colourbar). Data is superposition from dynamic wedge of Si (100 W, cp. Fig. 2.3) and timed wedge of Fe (50 W, cp. Fig. 2.4). The coordinates x and y define the separation from the Fe target center at the moment of target shut-down.

$d_{\mathrm{Si}}(y)$ with a gradient along the y direction (shown in Fig. 2.3). During one revolution of the sample in the chamber (Fig. 2.5) such a Si layer is combined with a timed Fe wedge (shown in Fig. 2.4), leading to a thickness d_{Fe} which mainly varies along the x axis. The numerical combination of both quantities yields a map of the $Si_{1-\delta}Fe_{\delta}$ layer properties (Fig. 2.6) showing lines of the thickness, as defined by the sum $d_{\mathrm{Si}} + d_{\mathrm{Fe}}$, and the Fe content, as defined by $d_{\mathrm{Fe}}/(d_{\mathrm{Si}} + d_{\mathrm{Fe}})$. In the region $-10\,\mathrm{mm} < y < 40\,\mathrm{mm}$ the gradients of thickness and composition meet nearly orthogonally, as intended. The simulation is a first check for the effects of the chosen fabrication parameters and it allows to identify regions that deliver interesting film parameters for the fabrication of Josephson junctions (sec. 3.2.3).

2.4 Electrical Characterisation Setup

To investigate the phenomena of superconductivity in films and devices low temperature environments and suitable electrical and magnetic shielding are required. For experiments with Nb-based Josephson junctions

a dewar filled with liquid helium can provide a thermal bath. If the junction is placed in the liquid helium a minimum temperature of 4.2 K is reached which roughly corresponds to half of the superconducting transition temperature of Nb electrodes. Higher temperatures are more difficult to stabilize but can be realized by a controlled heating of the sample or by careful placement of the sample in the gas phase above the liquid helium level. The undisturbed gas exhibits a temperature gradient normal to the liquid surface and slowly lifting the sample allows to increase its temperature monotonously.

A dipstick is used to position the sample within the helium dewar and to provide electrical contacts for signal and control wires. Besides being a mechanical mount for the superconducting device, it is equipped with a variety of elements that allow an extensive characterisation of the sample. The wafer piece, which carries the junctions, is glued to a circuit board which can be plugged into a 16 pin socket at the tip of the dipstick. Electrical contacts on the chip are wire bonded to copper lines on the board and forwarded through the socket into wires, which lead to the external equipment. The 16 lines are guided through the stick as twisted pairs to reduce crosstalk to other wire pairs. To connect a Josephson junction in a four point arrangement each superconducting electrode is contacted twice, resulting in four wires per junction and four fully connected junctions per chip holder. All wires that exit the full metal casing formed by helium can and dipstick are passing T-filters that shall damp high frequency noise which could heat the sample and disturb the measurements. The high sensitivity of superconducting devices against magnetic fields requires a proper shielding from environmental fields which is achieved by an enclosing cup of cryoperm®[2]. This alloy, made from Ni, Cu, Mo, Fe and Mn, is optimized to have a high permeability at low temperatures. On the other hand, magnetic fields are a valuable probe since they can influence the current transport through superconducting junctions in a non-trivial way (sec. 1.4). A long coil, which is embracing the sample holder, can be used to produce a homogeneous, uni-axial magnetic field along the stick direction. In the standard alignment the field threads the junction in-plane parallel to the leads of the superconducting electrodes. Furthermore

[2]VACUUMSCHMELZE GmbH & Co. KG

a Cernox™ temperature sensor[3] is located close to the chip and allows temperature readings between 4.2 K and room temperature.

Electrical measurements on Josephson junctions require an equipment which is able to operate over a wide current range from several µA up to tens of mA, while the load resistance can become very low and reduces to a tiny lead resistance when the junction is in the zero voltage state (junction current smaller than the critical current). At the same time, voltages in the µV to several mV range need to be detected with high accuracy. The community addresses their needs with specifically designed bi-polar current sources and voltmeters. We control and read the feedback of these units with a personal computer equipped with a National Instruments DA/AD converter card and the software GoldExi[4]. GoldExi is a software designed for the characterisation of Josephson junctions, which has capabilities that clearly exceed the automatic acquisition of current-voltage curves. It rather represents a complete solution for the measurement, control and determination of Josephson junction parameters. Various advanced routines and operation modes allow automatized measurements of e.g. the dependence of the critical current on temperature or magnetic field.

[3]Lake Shore Cryotronics, Inc.
[4]designed by E. Goldobin

3 Experiment and Discussion

This chapter covers experiments on thin film Josephson junctions focusing on the realisation of ferromagnetic π junctions with large critical current densities and critical voltages. Niobium is used as the only electrode material throughout this thesis. Starting with an account on SIS Josephson junctions, an overview on the technology basis and quality parameters of our $\mathrm{Nb}\,|\,\mathrm{AlO_x}\,|\,\mathrm{Nb}$ Josephson junctions is given. Then junctions with Si based barriers are presented. The section is dominated by studies on the influence of additional Fe layers and Fe impurities on the critical current density. $\mathrm{Si}_{1-\delta}\mathrm{Fe}_{\delta}$ layers were fabricated by combinatorial sputtering and their conductance mechanisms were compared to previous works. Finally the existing SIFS technology on the basis of $\mathrm{AlO_x(I)}\,|\,\mathrm{Ni_{60}Cu_{40}(F)}$ barriers is extended into an SIsFS technology by insertion of an additional Nb s-layer. So far only a theoretical concept, these junctions were fabricated and studied for various thickness of the s-layer and F-layer. Ferromagnetic junctions with a striking enhancement of j_c at constant R_N were found. The SIsFS technology also allowed to fabricate π Josephson junctions.

The critical current $j_\mathrm{c} = I_\mathrm{c}/A$ represents an area independent quantity which closely represents the experimentally acquired data. It is well suited to compare samples with similar values of normal resistance R_N and is used for presentations in this thesis. For a universal benchmarking of junction parameters however, the critical voltage $I_\mathrm{c}R_\mathrm{N}$ is calculated and compared to other publications. Experimental data can be linked to physical samples by the identification code of the wafer, as indicated by a tag, e.g. [s32$^{\mathrm{id}}$] , and summarized in the Table of Wafers (p. 103).

3.1 SIS Tunnel Junctions

Thin film Josephson junctions with a superconductor | insulator | superconductor (SIS) layer sequence can be fabricated from several superconducting elements. High quality junctions made from Pb [110] or Sn [111] and their respective oxides ($\sim$2 nm) as barriers have been reported, but these soft materials suffer during thermal cycling and are mechanically sensitive. Nb in contrast is a refractory metal which renders junctions robust against deterioration and promises facilitated handling and measurement with liquid helium due to its high T_c. However, the fabrication of all Nb junctions leads to a poor junction performance since the barrier is damaged by the deposition of the Nb counter electrode.

The key to fabricate high quality Josephson junction with Nb electrodes was the idea to use a barrier made from aluminium oxide [112,113]. Thin film stacks of Nb | Al | AlO_x | Nb sequence have become the quasi standard technology to fabricate conventional Josephson junctions. They combine favourable handling, reliability and performance in a way that makes them superior to all the alternatives investigated so far. Among the high quality properties are features like small leakage in the subgap voltage region, sharp gap voltage and controllability of the critical Josephson current over a wide range. Since the 1980s serious effort has been put into the characterisation and optimization of this junction type [114–117]. A combination of several mechanisms has been identified to be responsible for the outstanding performance of JJs made from Nb and AlO_x. Knowing these helps to optimise the fabrication technology and adapt the junction parameters according to individual requirements. Nb based Josephson junctions are commonly deposited in multi source sputter systems that allow to deposit the whole SIS sequence in situ without breaking the vacuum. To create high quality junctions the amount of impurities should be reduced to a minimum. Already small contaminations can weaken or destroy superconductivity and interfere uncontrollably with the tunnelling process through the barrier.

The ground electrode, as the basis for the whole junction, serves two purpose. First it should have a well developed superconducting gap which is achieved by proper sputtering conditions. The superconductivity benefits from a sufficient sputter rate of more than 2 $^{nm}/_{s}$ and care has to be taken that the argon pressure is optimized with respect to a

minimum stress in the Nb layer. Second the bottom electrode should provide a smooth and flat surface for the subsequent barrier deposition and formation. It is know that sputter deposited Nb grows in a polycrystalline fashion with a surface roughness that increases with growing layer thickness. For a reliable Nb electrode a compromise needs to be found between a thickness above the pair coherence length, including a possible margin for etching processes, and the size of the grains which interfere with the barrier formation. As explained in the following paragraph, Al or $\mathrm{Al}\,|\,\mathrm{AlO_x}$ layers have the ability to even out the roughness of a Nb layer and interrupt the propagation of grain boundaries [118]. Due to the proximity effect, thin layers of Al can be incorporated in the bottom electrode without a drastic degradation of the electrode's superconducting properties. Instead the procedure increases the homogeneity of the barrier topology [119].

The next fabrication step is the deposition of an aluminium layer that is oxidized afterwards to form a tunnel barrier. As it turned out, the roughness of the Nb surface is dressed by the aluminium layer and the oxidisation in O_2 atmosphere can yield excellent tunnelling barriers with very few defects. Studies about the $\mathrm{Nb}\,|\,\mathrm{Al}$ interface reveal that Al layers as thin as 1 nm can wet the Nb surface completely and that parts of the Al layer may diffuse into grain boundaries or alloy with Nb [120]. Particular attention should be paid to the temperature of the Nb substrate since it significantly affects the growth of aluminium during deposition. While the reduced mobility of adatoms at room temperature and below leads to closed layers already for several monolayers of Al and thicker layers stay at the surface, higher temperatures can support island formation and Al diffusion into Nb [114, 116, 121]. Once the Al layer is deposited, an oxide layer can be formed by exposure to oxygen gas. Compared to an exposure to ambient air, a controlled high purity O_2 atmosphere in the vacuum system is less subject to impurity contamination and more flexible in the choice of process parameters. An evaluation of various kindred oxidisation experiments reveals a universal dependence of the Josephson critical current j_c to the oxygen exposure $E = p \cdot t$, which is the product of the oxygen partial pressure p and exposure time t [122]. Two distinct regimes of *low* and *high* exposure were identified. The authors attribute large critical current densities in the low exposure

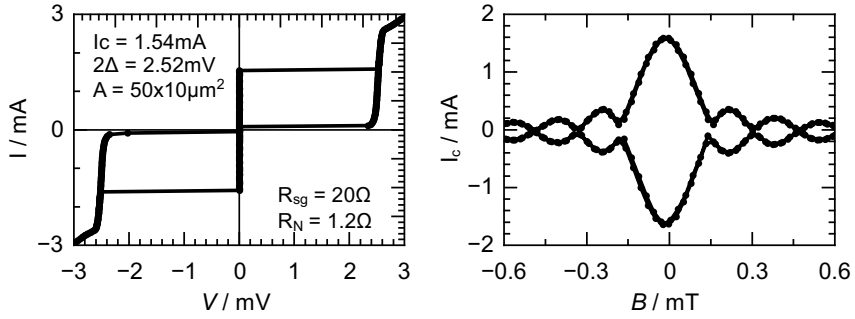

Figure 3.1 Rectangular SIS Josephson junctions in Nb | Al | AlO_x | Nb technology with a hysteretic $I(V)$ curve and a Fraunhofer $I_c(B)$ dependence. [ref5.3[id]]

range to metallic conduction channels in the barrier (pinhole defects) whose density decreases with the completion of the first monolayers of AlO_x. In the high exposure regime the critical current is governed by tunneling through the insulating barrier and mainly depends on the thickness. The gas oxidisation of aluminium is self limiting and several authors report a maximum AlO_x thickness of 2 to 3 nm [103, 118, 120]. To achieve such a thick barrier the oxidisation process may be assisted by plasma ionisation of O_2, UV irradiation of the sample or thermal activation. It is advisable to use an excess of aluminium to supply sufficient material for the AlO_x growth, i.e. a not oxidised layer of Al will remain between the Nb and the oxide. However, the transport properties of the junction are only weakly affected because a few nm of Al will become superconducting due to the proximity effect with the adjacent Nb electrode (sec. 1.6.3).

After the tunnel barrier has been formed the junction is terminated by a Nb cap which acts as the counter electrode. The thickness of the cap should be chosen larger than the superconducting coherence length in order to avoid weakening of the bulk superconducting properties [123]. Despite all efforts, close to the barrier the T_c of the counter electrode will be reduced by the non-ideal interface [115].

This fundamental SIS structure is incorporated into a variety of devices.

Table 3.1 Oxidisation parameters for AlO_x barrier, (*) electrical characteristics in Fig. 3.1

O_2 pressure p/mbar	time t/s	critical current density j_c/kA/cm²
0.01	1800	7.0
0.1	1800	1.2
1	1800	0.7
5	1800	0.37 *
50	1800	0.12

They range from single junctions for research, signal detectors and mixers up to more complex integrated superconducting circuits. It is widely used in laboratories, like for this work, and to some extent at the industrial scale [124, 125].

For reference purpose a variety of SIS Josephson junctions have been fabricated. An example for the electrical characteristics of a high quality junction is shown in Fig. 3.1. This junction exhibits a rather thick AlO_x barrier. By variations of the chamber oxygen pressure and exposure time, the oxidisation process can be modified leading to a variation of the barrier thickness and therefore the critical current density j_c. Barriers with good quality and yield could be achieved, e.g. with the parameters mentioned in Table 3.1. Tunnel layers with large critical current densities are advantageous for experiments where additionally ferromagnetic material is inserted into the barrier leading to a strong suppression of the Josephson current. Junctions with $j_c \geq 10\,\mathrm{kA/cm^2}$ were fabricated, but they are more susceptible to defects in the barrier, pinhole currents and flux trapping in the barrier.

3.2 S(FI)S – Si and Fe Based Barriers

The possibility to achieve π Josephson junctions with barriers made from ferromagnetic insulators (FI) was investigated with the alloy $Si_{1-\delta}Fe_\delta$. The quasi particles that cross the barrier can experience a spin flip at

magnetic impurities. A phase shift of π in the ground state might be achieved by a certain range of composition and thickness of $Si_{1-\delta}Fe_{\delta}$ compounds (sec. 1.6.3). In analogy to proximity effect π junctions , a 0–π transition due to spin-flip events should cause a kink to zero in the $j_c(d)$ and $j_c(\delta)$ dependencies.

Nb based Josephson junctions with several types of Si/Fe barriers have been fabricated and studied with the focus on the evolution of junction properties with the barrier thickness and composition. Layer sequences with

Nb | (Al |) Si | Nb	pure insulator,
Nb | (AlO_x |) Si | Fe | Nb	sandwich of Si and Fe,
Nb | (AlO_x |) Si | Fe | Si | Nb	Fe in the center of a Si barrier and
Nb | (AlO_x |) SiFe | Nb	Fe dispersed in Si

have been prepared. The barriers differ in the distribution of Fe along the normal direction. The Fe impurities are homogeneously distributed within the barrier in the case of a $Si_{1-\delta}Fe_{\delta}$ barrier or located in the middle of the barrier for Si \| Fe \| Si structures. Additional AlO_x tunnel barriers were employed where necessary to facilitate the measurement process by increasing the normal resistance and provide a constant resistance baseline.

3.2.1 Pure Si Barrier

Josephson junctions with amorphous Si (a-Si) barriers have served as model systems to study the influence of localized electron states on the current transport. The small barrier height of less than 0.3 eV allows experimentally feasible critical Josephson currents for barrier thickness up to 10 nm [126, 127]. In comparison, common oxide barriers show the same tunneling current for thinner barriers of a few nanometer. The extended thickness of the Si barrier facilitates local modifications of the barrier properties. A hydrogenation of a thin layer in the centre of the barrier yields highly insulating barriers at low T and good quality junctions by saturating dangling Si bonds that support the resonant tunnelling process [128]. A study on the position of a thin SiO_2 layer in the Si barrier also highlighted the relevance of states located at the centre of the barrier for the barrier conductance [127].

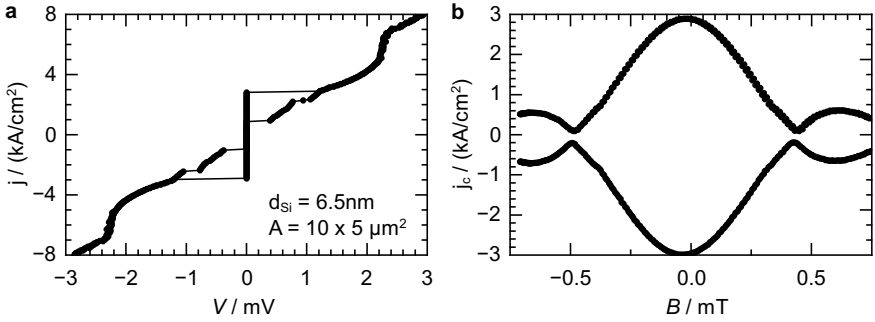

Figure 3.2 Electrical characteristics of a Nb | Al | $Si^{6.5\,nm}$ | Nb Josephson junction at $T = 4.2\,K$, the $I_c(B)$ shows a Fraunhofer like modulation. [si5id]

For this work, junctions with magnetron sputtered non-hydrogenated Si barriers have been studied. The Si thickness d_{Si} was varied between 5 nm and 9 nm. Figure 3.2 shows the IV characteristics for a sample with d_{Si}= 6.5 nm and a critical current density $j_c = 2.8\,\mathrm{kA/cm^2}$. Compared to good AlO_x tunnel barriers with the same j_c, the superconducting gap voltage is reduced and the subgap resistance is significantly enhanced. The slight knee structure above 2 mV stems from the proximity effect present in an amorphous Nb layer that forms at the interface between Si barrier and upper electrode during fabrication. The $I_c(B)$ dependence is Fraunhofer shaped, which indicates a homogeneous current density distribution and the absence of pinholes. Variations of the Si thickness do not significantly modify the shape of the $I(V)$ as shown in a normalized comparison (Fig. 3.3). Only for thin barriers, which lead to large current densities, the superconducting gap voltage is reduced.

Some information about the structure of the barrier region can be acquired from the differential conductance $\mathrm{d}I/\mathrm{d}V$. Specific peaks may be attributed to the sum $(\Delta_1 + \Delta_2)/e$ and the difference $|\Delta_1 - \Delta_2|/e$ of the superconducting gap voltage for upper Δ_1 and lower electrode Δ_2 [129]. Figure 3.4 shows a spectrum for $d_{Si} = 8.5\,nm$, which was acquired by numerical derivation of the $I(V)$-curve. The symmetric positions of the peaks are highlighted and basic maths allows to extract values for the individual energy gap $2\Delta_1$ and $2\Delta_2$. Using this method the

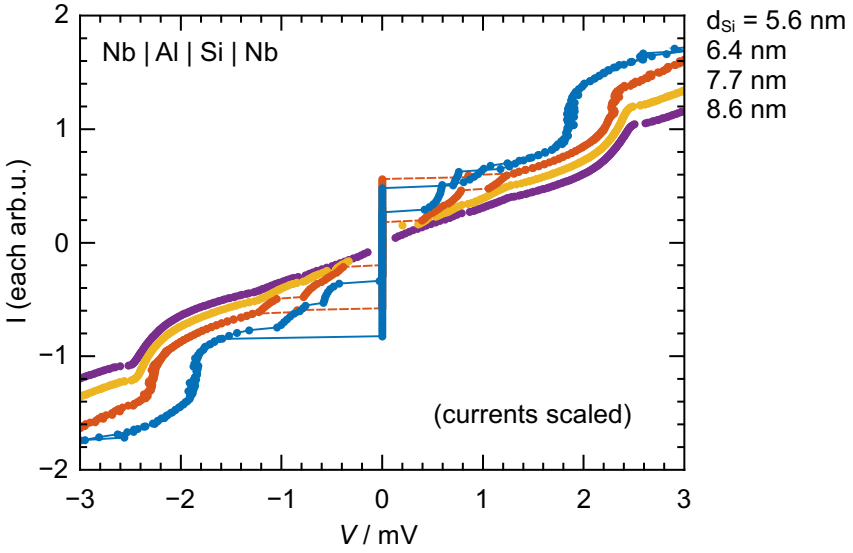

Figure 3.3 $I(V)$ curves of Nb | Al | Si | Nb Josephson junctions with varying thickness of the Si barrier d_{Si}, currents normalized to compare gap voltage and subgap characteristics. All curves are hysteretic. [si5^{id}]

energy gaps have been traced for temperatures in the range from 4.2 K to 9 K. Especially for temperatures in the interval of about 1 K below T_c the determined gaps are smaller than a fit to the BCS theory would suggest. The anomalous deviation in Δ_2 is explained by a proximity effect model for the amorphous Nb layer which is formed at the upper Si | Nb interface during fabrication [44, 129]. Low values of Δ_1 can be explained by the proximity effect in the Al buffer layer at the lower Nb | Al | Si interface [45].

In addition, the temperature dependence of the critical current $I_c(T)$ was determined above liquid helium temperature and found to decrease linearly from 4.2 K to 8 K (Fig. 3.5). Instead of a convex curvature, which would follow from a BCS density of states in the electrodes via the Ambegaokar-Baratoff dependence, a proximity effect model is better suited to describe the data [130].

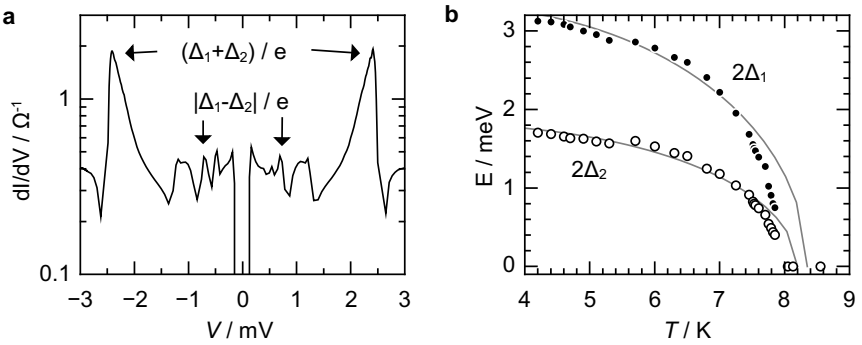

Figure 3.4 Spectroscopic data for Nb | Al | Si | Nb junctions **a** $\mathrm{d}I/\mathrm{d}V$ by numerical derivation of $I(V)$ acquired at $T = 4.2\,\mathrm{K}$ for $d_{\mathrm{Si}} = 8.5\,\mathrm{nm}$. The highlighted peaks are used to calculate **b** the evolution of the superconducting gap 2Δ with junction temperature T, BCS dependencies for $T_{\mathrm{c}} = 8.2\,\mathrm{K}$ and $8.3\,\mathrm{K}$ are shown as line. [si5/F$^{\mathrm{id}}$]

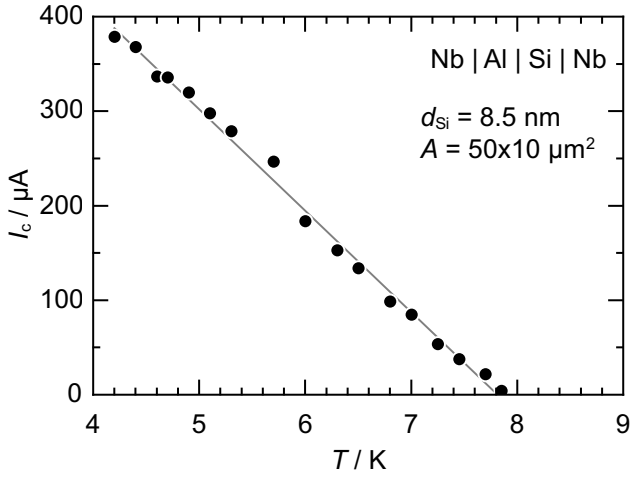

Figure 3.5 Critical current I_{c} versus temperature for a Nb | Al | Si | Nb Josephson junction. [si5/F$^{\mathrm{id}}$]

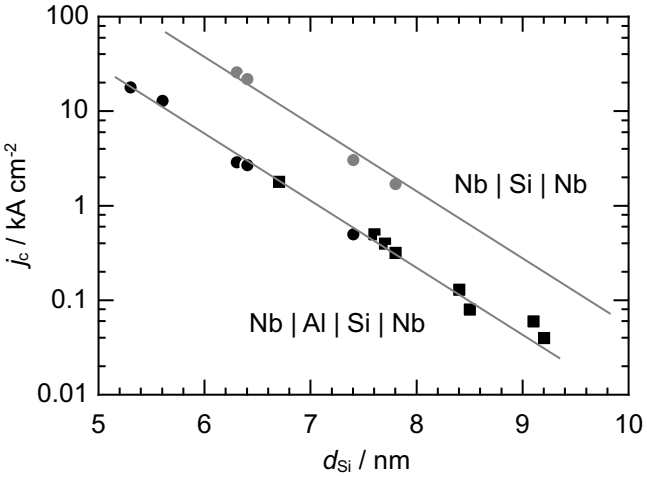

Figure 3.6 Critical current density j_c versus Si thickness d_{Si} in Nb (| Al) | Si | Nb Josephson junctions for junction areas $50 \times 10\,\mu m^2$ (●) and $10 \times 10\,\mu m^2$ (■). [si5^{id}] [si6^{id}]

Finally, several junctions with different Si barrier thickness d_{Si} have been characterized and the critical current was found to cease exponentially between 5 nm and 9 nm (Fig. 3.6) [131]. It is evident, that the aluminium buffer between the bottom Nb electrode and the Si barrier shifts the $j_c(d_{Si})$ dependence. The Al may planarises the interface, which leads to an increase in the effective barrier thickness of about 1 nm.

In summary, the Josephson junctions with silicon barrier, as fabricated for this thesis, show properties that are in good agreement with previously published results. The fabrication parameters served as the basis for the fabrication of junctions with ferromagnetic barriers.

3.2.2 Multilayer

The elements Fe and Si can be combined in various ways to form a Josephson junction barrier. While the incorporation of small Fe clusters into a matrix of Si is investigated in section 3.2.3, the following account focuses on multilayer structures. Two cases for the insertion of an Fe

layer into Si are presented. The first is a bilayer Si | Fe and the second buries the Fe layer in the middle of the Si layer, splitting it in two layer of equal thickness, thus forming a Si | Fe | Si sequence.

The SIFS bilayer barrier is popular for experiments on ferromagnetic Josephson junctions. Built with a layer of pure ferromagnet, the coherence length of Cooper pairs is short due to the large magnetic exchange energy. Data from AlO_x | Fe junctions shows a strong suppression of the Josephson current by the Fe layer (Fig. 3.7). Up to relatively thin $d_{Fe} = 2.5\,nm$, the critical current density ceases while maintaining Fraunhofer-like $I_c(B)$ pattern. For thicker Fe-layers, critical currents with non-systematic amplitude reappear, but do not modulate significantly with an applied magnetic field. Phenomenologically, these currents can be attributed to localised pinholes which are possibly created by Fe clusters that punctuate the AlO_x barrier. For Si | Fe barriers with d_{Si} of 5 nm and 8 nm the $j_c(d_F)$ dependence shows similarities to AlO_x | Fe junctions. The critical current is heavily suppressed by the Fe layer with larger d_{Fe}. Depending on d_{Si}, I_c either vanishes at $d_{Fe} = 2\,nm$ ($d_{Si} = 8\,nm$) or shows significant values up to $d_{Fe} = 3\,nm$ ($d_{Si} = 5\,nm$). In the latter case, the residual I_c is again likely to be caused by pinholes.

Junctions with the barrier sequence Si | Fe | Si concentrate Fe in the middle of the barrier, opposed to a homogeneously mixed $Si_{1-\delta}Fe_\delta$ layer. It is known that impurities in a tunnel barrier that are positioned halfway between the electrodes promote the current transport via resonant tunneling. At this location they are also expected to effectively cause spin-flip events which may lead to a π coupling. Series of junctions were fabricated where Fe was deposited either by timed or by static wedge deposition. Qualitatively, the $j_c(d_F)$ of all junctions resemble the case of Si | Fe with thin d_{Si} (Fig. 3.8). Although the calibration of d_{Fe} is reliable with respect to monotonicity, the calibration might not correctly reflect local changes in the slope of the wedge. This means that a series of junctions along the wedge direction across the wafer do strictly increase or decrease in layer thickness. The thickness axis however might exhibit an offset or non-uniform scaling which depends on the method used for deposition.

The different wafer series concordantly show a certain threshold of d_{Fe} at which j_c is strongly suppressed and a significant magnetization of the Fe layer can be assumed. For larger d_{Fe} the Josephson current

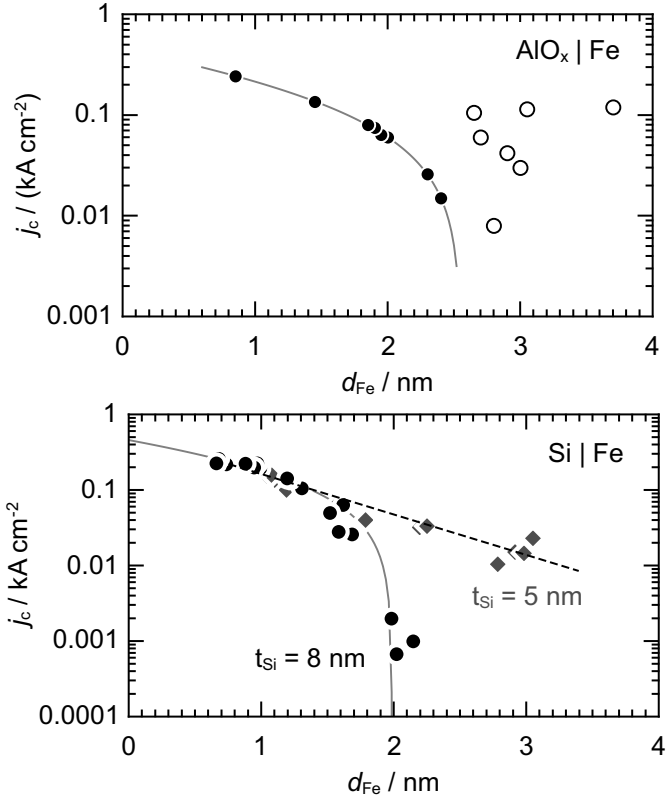

Figure 3.7 Critical current density j_c versus thickness of Fe layer d_{Fe} in Nb | AlO_x | Fe | Nb [Fe1id] and Nb | Al | Si | Fe | Nb Josephson junctions [s04id] [s07id] .

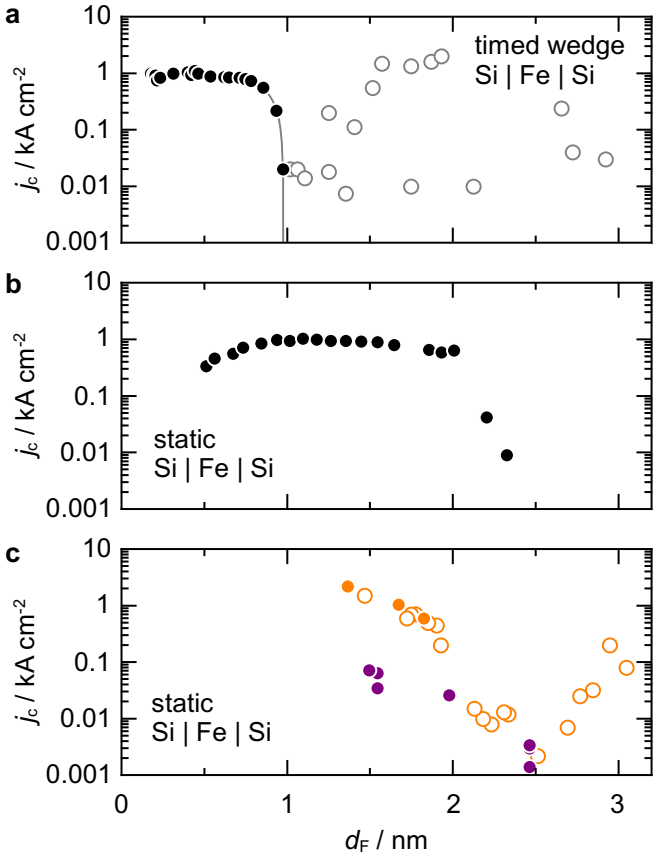

Figure 3.8 Critical current density j_c versus thickness of ferromagnetic layer d_F for Nb | Al | Si | Fe | Si | Nb Josephson junctions. **a** Fe deposited with a timed wedge approach. **b** and **c** deposited with a static wedge approach. The data points distinguish between Fraunhofer-shaped $I_c(B)$ patterns (filled •) and non-Fraunhofer shaped patterns (open ○). [s01^{id}] [s03^{id}] [s06^{id}]

becomes non deterministic and the $I_c(B)$ doesn't show clear modulations. In this regime the dominating contribution to the current is expected to originate from pinholes.

3.2.3 $Si_{1-\delta}Fe_{\delta}$ Alloy

The deposition of $Si_{1-\delta}Fe_{\delta}$ layers with non-parallel gradients of thickness d and composition δ was performed by combinatorial sputtering (sec. 2.3). Si and Fe are deposited as alternating layers with submonolayer thickness. Due to the high reactivity between the two materials at room temperature, the process is expected to form a homogeneous alloy [132]. To get information about the layer properties with respect to the position on the wafer, a two dimensional calibration of d and δ is required. A destructive direct study of the barrier layer of individual Josephson junctions, which would require the accurate determination of buried layers in the nanometer range, was discarded. Analysis techniques, like transmission electron microscopy (TEM) with high resolution and analysis modes like energy-dispersive X-Ray spectroscopy (EDX) or electron energy loss spectroscopy (EELS) were considered not feasible for an extensive two dimensional calibration map.

In this work, a combined calibration approach is used for $Si_{1-\delta}Fe_{\delta}$ layers that are deposited by combinatorial sputtering. First, the $Si_{1-\delta}Fe_{\delta}$ thickness profile is directly measured and used to deduce the individual thickness profiles of Si and Fe, based on assumptions about the wedge directions. From these profiles the alloy composition is calculated and verified by comparison to simulations of the combinatorial sputtering process (cp. 2.3) and further experimental data.

For investigation purpose, a $Si_{1-\delta}Fe_{\delta}$ layer, several times thicker than an actual barrier, was deposited by combinatorial sputtering on $5 \times 15\,mm^2$ $Si\,|\,SiO_2$ wafer pieces which were distributed across the wafer holder. These substrates were subsequently investigated by X-Ray reflectivity (XRR), resulting in a map of $Si_{1-\delta}Fe_{\delta}$ thickness (Fig. 3.9a). The layer thickness increases from the upper left side of the sample holder towards the lower left. The possibility of redepositing Si and Fe individually and measure their respective thickness ruled out particularly

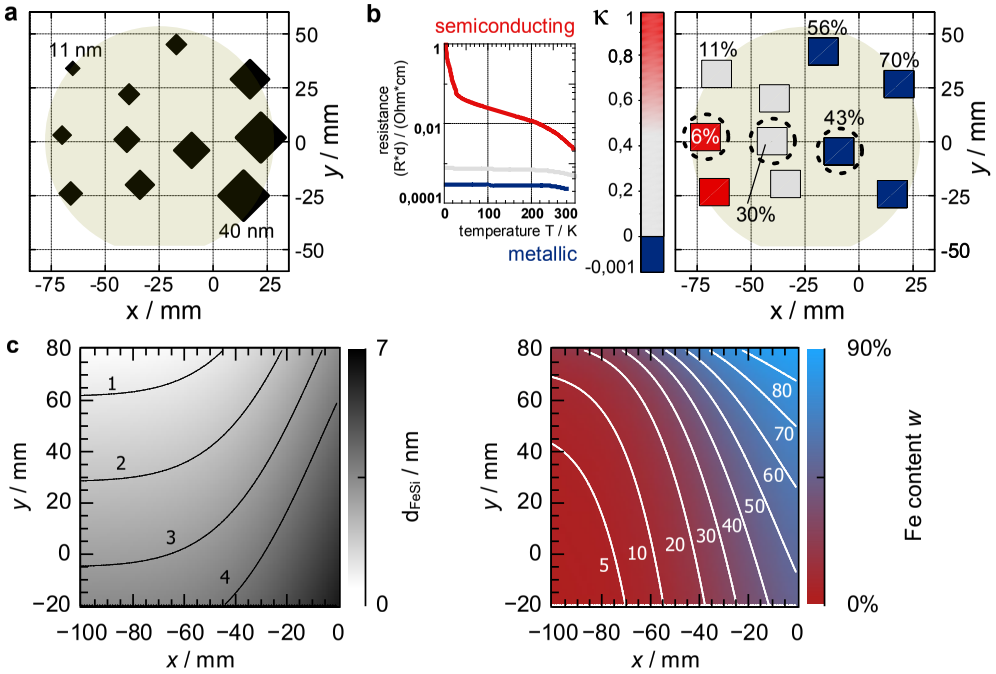

Figure 3.9 $Si_{1-\delta}Fe_{\delta}$ calibration from measurement points distributed across a 4 inch wafer showing **a** thickness as determined by XRR and **b** conductivity coefficient κ as determined from $R(T)$ curves (more data in Fig. 3.10), Fe content in % **c** similar sections of the deduced calibration maps for layer thickness and Fe content, coordinates (x, y) are relative to sputter target center (partially adapted from [106])

for regions with a low Fe content

$$\delta \ll 1 - \delta \tag{3.1}$$

that would lead to very thin Fe films. So the thickness contributions of Fe d_{Fe} and Si d_{Si} were extracted from the measured alloy thickness d_{SiFe} based on the assumption

$$d_{\mathrm{SiFe}}(x, y) = d_{\mathrm{Fe}}(x) + d_{\mathrm{Si}}(y), \tag{3.2}$$

that the thickness of the individual Fe and Si layers only changes along the x and y direction, respectively. As a second quantity, the composition δ had to be determined. Direct measurements by Rutherford backscattering (RBS) were discarded due to the low sample thickness and limited analysis capacity. So the composition δ is determined from the ratio of layer thickness

$$\delta = \frac{d_{\mathrm{Fe}}}{d_{\mathrm{Si}} + d_{\mathrm{Fe}}}. \tag{3.3}$$

A qualitative verification was achieved by measurements of the sheet resistance. The $R(T)$ behaviour (Fig. 3.9b) identifies semiconducting (Si rich) and metallic (Fe rich) calibration samples. The resistance coefficient

$$\kappa = \frac{R(8\,\mathrm{K}) - R(150\,\mathrm{K})}{R(8\,\mathrm{K}) + R(150\,\mathrm{K})} \tag{3.4}$$

is introduced to quantify the change in resistance and compare different samples.

The constraint (3.2) allowed to determine d_{Fe} and d_{Si} for the datapoints in Fig. 3.9a by hand. After a linear interpolation of datapoints, calibration maps of $d_{\mathrm{SiFe}}(x, y)$ and $\delta(x, y)$ could be visualized (Fig. 3.9c). The thickness is scaled to represent the barrier layer as actually deposited for Josephson junctions. Obviously perpendicular parameter gradients could not be achieved all over the wafer. But the isolated influence of one parameter on the junction properties without significant changes of the other parameter can still be studied. Nearly orthogonal angles between the two gradients are only found for $\delta \leq 20\,\%$, for larger δ the

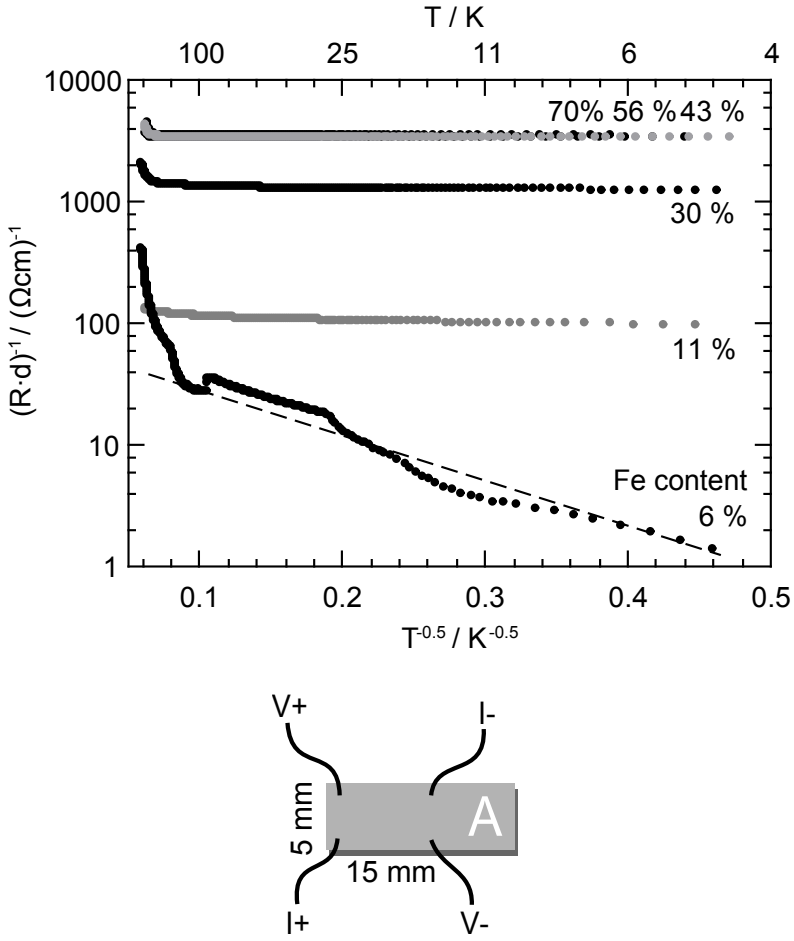

Figure 3.10 $R(T)$ data for $Si_{1-\delta}Fe_{\delta}$ thin films presented in Arrhenius like coordinates. In the temperature range between 4.2 K and 100 K and for an Fe concentration of 6 % hopping dominates the conductance according to equation (1.36). Samples with $\geq 11\,\%$ Fe behave metallic. The samples are the same as in Fig. 3.9 and can be identified via the Fe content. Small scale features in the curve are related to measurement artefacts. Sketch shows a calibration wafer piece with lithographically defined label and 4-point wiring for $R(T)$ measurement.

angles approach values around 45°. Deviations between the calibration and simulations of the alloy film based on measured linear profile of the static rate for Si and Fe (Fig. 2.6) occur. For $x \leq -50\,\mathrm{mm}$ both sets of data show good agreement. At $x \geq -50\,\mathrm{mm}$ the gradient direction in the calibration maps clearly deviate from the simulation.

A more detailed analysis of the conductivity mechanisms in $Si_{1-\delta}Fe_{\delta}$ films is based on $R(T)$ measurements. The degree of Fe doping into sputtered or evaporated amorphous Si has an influence on the conductivity. Studies on the temperature dependence of the conductivity for various Fe concentrations [133] show a clear activation character in the conductivity for low concentrations and low temperatures. Especially for Fe concentrations below 11 % and a temperature interval between 4.2 K and 100 K a Shklovskii-Efros dependence (1.36) for variable range hopping was found. $R(T)$ measurements (Fig. 3.10) reveal the Shklovskii-Efros activation type character of the hopping process for thin films with 6 % Fe in the temperature range between 4.2 K and 100 K. Samples with larger Fe concentrations show orders of magnitudes larger conductance and are nearly temperature independent, which indicates metallic conduction. The geometry for the determination of the sheet resistance was the same for all samples under investigation. The resistance value was multiplied by the layer thickness as extracted from XRR measurements to normalize the results. It must be noted, that the inverse resistance in Fig. 3.10 can only qualitatively be compared to conductivity data in other publications. The resistance measurements were inspired by the van der Pauw [134] geometry, but they did not strictly follow the measurement and evaluation procedure.

Josephson Junctions with $Si_{1-\delta}Fe_{\delta}$ barrier

As discussed in the preceding section, small fractions of Fe drastically enhance the low temperature conductivity of Si. $Nb\,|\,AlO_x\,|\,Si_{1-\delta}Fe_{\delta}\,|\,Nb$ Josephson junctions, that exhibit a $Si_{1-\delta}Fe_{\delta}$ layer of various thickness d_{SiFe} and Fe content δ, have been fabricated by combinatorial sputtering (sec. 2.3). The constant AlO_x tunnel barrier shall establish a resistance baseline for the comparison of individual junctions. Using the combinatorial deposition technique, $Si_{1-\delta}Fe_{\delta}$ layers with quasi constant d_{FeSi} and varying δ have been fabricated. The values of d_{SiFe} and δ were extracted

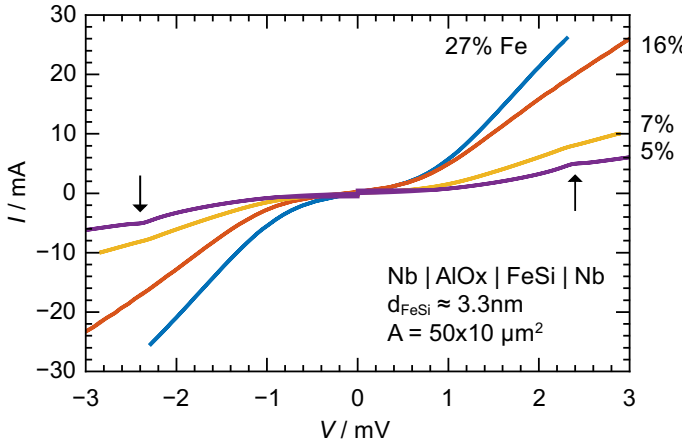

Figure 3.11 Current–voltage curves of Nb | AlO_x | $Si_{1-\delta}Fe_\delta$ | Nb Josephson junctions for various Fe concentrations δ. The arrows indicate the superconducting gap. [FeSi9id]

from calibration data (Fig. 3.9c). The cross-section of a junction was analysed with a transmission electron microscope by V. Hrkac (Appendix B). TEM images show a flat and well defined interface between a polycrystalline Al layer and the barrier. The $Si_{1-\delta}Fe_\delta$ alloy is homogeneous in thickness and well mixed as indicated by EDX measurements.

Electrical $I(V)$ data of the junctions are shown in Fig. 3.11. An increase of the Fe doping into the Si barrier decreases the barrier resistance. For low Fe concentrations the superconducting gap can be identified. Also the damping is low, such that the curve becomes hysteretic for small voltage. Already for junctions with $\delta = 7\,\%$ the gap starts to vanish, I_c is reduced and an increased damping leads to a single valued $I(V)$. A study of the critical current density j_c with the Fe content δ shows a quasi exponential decrease (Fig. 3.12). For larger layer thickness d_{FeSi} the decrease becomes stronger. The volatility of the points is attributed to the non-ideal calibration of $Si_{1-\delta}Fe_\delta$ properties. Although the junctions are placed along a line across the wafer which should exhibit a rather constant d_{FeSi} it is possible and likely, that small variations in the thickness occur.

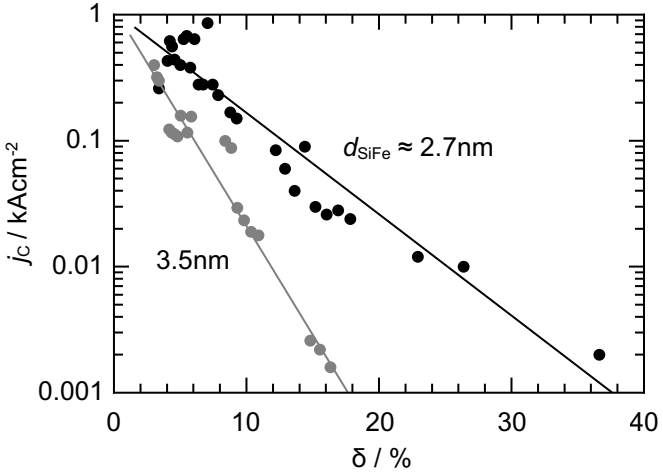

Figure 3.12 Critical current density j_c vs. Fe content δ of $Nb\,|\,AlO_x\,|\,Si_{1-\delta}Fe_\delta\,|\,Nb$ junctions for two different layer thickness d_{FeSi}. Lines are guides to the eye. [FeSi8^{id}] [FeSi9^{id}]

A different $Nb\,|\,AlO_x\,|\,Si_{1-\delta}Fe_\delta\,|\,Nb$ wafer with a very thin AlO_x barrier was fabricated and junctions along lines of constant d_{SiFe} and along constant δ were characterised (Fig. 3.13). For a thickness of about $d_{FeSi} = 4.5\,\text{nm}$ an exponential decrease of j_c up to $\delta = 45\,\%$ is observed. At larger δ the $I_c(B)$ dependencies become irregular, which was already observed for $Si\,|\,Fe\,|\,Si$ barriers (sec. 3.2.2). Interestingly, j_c drops to zero at the same total amount of Fe in the barrier for both types of junctions. This suggests the conclusion, that the distribution of Fe in the barrier does not severely influence j_c. For $\delta = 30\,\%$ the $j_c(d_{FeSi})$ dependence shows an exponential decrease of the critical current density between $d_{FeSi} = 2.5\,\text{nm}$ and $5\,\text{nm}$. A small bump around $4\,\text{nm}$ is not bounded by sharp cusp-like dips to $j_c = 0$ which would indicate a 0–π transition. In fact, the constant property in the measurements might also be subject to a variation which is not covered by the calibration. In particular for consecutive junctions, that are linearly aligned on a wafer, such imperfections may manifest in steady variations of j_c and modest curvatures in the graph, as observed in the data.

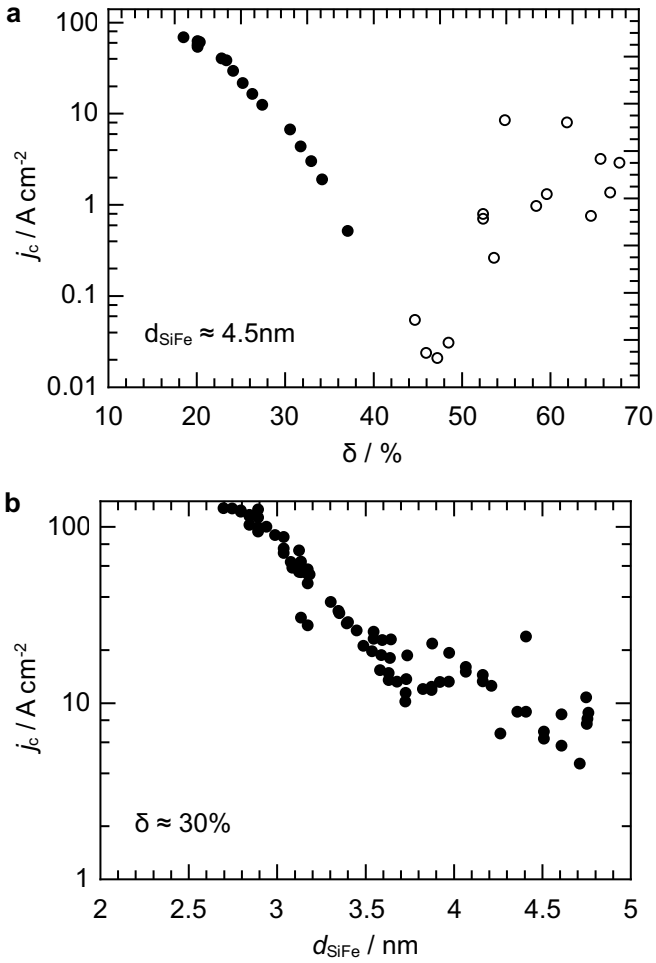

Figure 3.13 Critical current density j_c of Nb | AlO_x | $Si_{1-\delta}Fe_\delta$ | Nb junctions for varying **a** Fe content δ and **b** thickness d_{FeSi}. The $I_c(B)$ of the samples are either Fraunhofer modulated (filled •) or flat and irregular (open ○). (data acquisition H. Sickinger) [FeSi10[id]]

3.2.4 Conclusion

Due to its intimate connection to conventional CMOS technology, Si is a desirable candidate also to be used for quantum circuitry. In the past, Josephson junctions made with pure Si barriers of several nm achieved reasonable performance and allowed to study charge-transport mechanisms. However, Si can also serve as an insulating matrix for the embedding of ferromagnetic particles. At low temperatures, this functionalisation results in a ferromagnetic insulator. A possible realization of π Josephson junctions by spin-flip at ferromagnetic impurities was investigated with Si and Fe. Junctions with diverse barriers types, covering multilayers and combinatorially sputtered alloys with various compositions and thickness, were fabricated. Experimental data shows that structures that contain pure Fe layers yield reliable Josephson junctions up to $d_\mathrm{F} \approx 2\,\mathrm{nm}$. For larger d_F a massive increase of pinhole probability and a strong magnetic influence on the junction behaviour is observed. By the implementation of a novel combinatorial sputtering technique $\mathrm{Si}_{1-\delta}\mathrm{Fe}_\delta$ layers could be deposited from individual targets. A perpendicular gradient approach allowed to create layers with systematic and independent variations of layer thickness and composition. Josephson junctions with $\mathrm{Si}_{1-\delta}\mathrm{Fe}_\delta$ barriers exhibit a suppression of the critical current with increasing thickness and composition. The data suggests that j_c is dominated by the total amount of Fe in the barrier independent from the distribution along the surface normal direction. Despite these various approaches no indication for a 0–π transition with Si and Fe based barriers could be found.

3.3 SIFS – $\mathrm{Ni}_{60}\mathrm{Cu}_{40}$ Barrier

Josephson junctions, comprising silicon barriers of several nm thickness, can exhibit a high transparency and therefore large critical current densities (cp. section 3.2). Their applicability as an insulating barrier for $\mathrm{Ni}_{60}\mathrm{Cu}_{40}$-based π Josephson junctions of SIFS type has been investigated. Two series of SIFS junctions with I-layers, either made of 8 nm silicon or formed by an $\mathrm{AlO_x}$ barrier, and a $\mathrm{Ni}_{60}\mathrm{Cu}_{40}$ F-layer with various thickness d_F have been fabricated. A comparison of $j_\mathrm{c}(d_\mathrm{F})$ curves for both barrier materials is shown in Fig. 3.14. In case of the $\mathrm{Nb}\,|\,\mathrm{Si}\,|\,\mathrm{Ni}_{60}\mathrm{Cu}_{40}\,|\,\mathrm{Nb}$

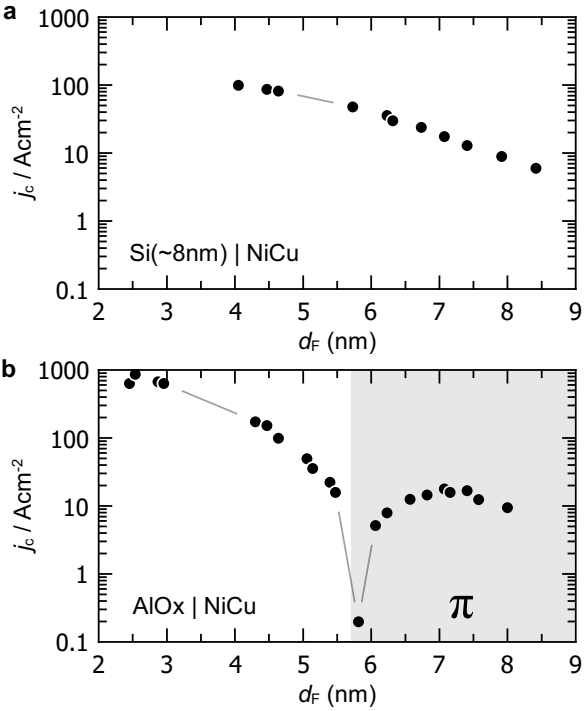

Figure 3.14 $I_c(d_F)$ dependencies for **a** Nb | Si | $Ni_{60}Cu_{40}$ | Nb junctions [nr03[id]] and **b** Nb | AlO_x | $Ni_{60}Cu_{40}$ | Nb junctions [nr02[id]] which show a 0–π transition close to $d_F = 6$ nm

junctions a monotonic decrease of j_c is observed with d_F increasing from 4 nm to 8 nm. In contrast, the Nb | AlO_x | $Ni_{60}Cu_{40}$ | Nb junctions show a distinct cusp-like dip at 5.8 nm, which is characteristic for a 0–π transition of a Josephson junction (cp. section 1.6.2).

Both $j_c(d_F)$ dependencies have a similar envelope for $d_F > 4$ nm governed by an exponential decay that is defined by the coherence length in the $Ni_{60}Cu_{40}$ layer. This is despite the fact that at $d_F = 0$ nm the critical current for these particular junctions with AlO_x would be more than one order of magnitude larger than for the Si barrier junctions.

Moreover, for $AlO_x \,|\, Ni_{60}Cu_{40}$ junctions the existence and position of the transition from 0 to a π ground state confirms former measurements at this system [95]. A reason for the striking absence of a 0–π transition for the junctions with a Si barrier cannot be given. However, the result consistently fits to the lack of a 0–π signature in barriers based on Si and Fe as investigated in section 3.2.

3.4 SIsFS – $Ni_{60}Cu_{40}$ Barrier

Essential results and figures in this section have been published [135] and are presented in agreement to the copyright regulations of the American Institute of Physics (Applied Physics Letters).

Recently, the concept of an SIsFS junction with a tunnel barrier (I) and a ferromagnetic layer (F) separated by a layer of superconductor (s) has been presented. First experimental results compared an SIsS and an SIsFS junction and presented similar values of j_c and $I(V)$ curves with only a minor influence of the F-layer on the subgap characteristics [136]. Probably for the same junction an $I_c(T)$ dependence was also published [137]. In contrast to the few individual experimental realisations, a comprehensive theoretical study has been performed on these SIsFS junctions [138, 139]. The F-layer was made from the alloy $Pd_{99}Fe_1$ which is magnetically soft and therefore allows a reliable switching of the magnetisation direction by the application of an external magnetic field.

The SIsFS approach promises junction parameters that are comparable to conventional non-magnetic Josephson junctions and technological compatibility to existing superconducting circuits. However, exceeding the mere use as magnetic bias or source of a spin polarized current, the ferromagnetic layer can also lead to a Josephson junction which exhibits a phase difference of π between the electrodes in its ground state (cp. sec. 1.6.3). Suffering from the same problems like magnetic superconducting memory it is still not possible to built π Josephson junctions with the same range of parameters and reproducibility as conventional SIS junctions. The SIsFS approach could allow the developement of π junctions with an I_cR_N product that is large enough, so that the switching frequency is applicable for RSFQ logic [136].

Being relieved from the requisite of easy remagnetization of the ferromagnetic layer, the following experiments are done with the ferromagnetic alloy $Ni_{60}Cu_{40}$. Barriers comprising this ferromagnet have reliably been used for the fabrication of SIFS structures that form π Josephson junctions with reasonably high critical current densities and normal resistance [95]. An extensive, systematic experimental study on the electrical characteristics of SIsFS junctions for various thickness of the s- and F-layer will be presented in the following.

3.4.1 Theoretical Predictions

As presented before, SIS junctions with critical current densities above a few $10\,{}^{\mathrm{kA}}/_{\mathrm{cm}^2}$ are difficult to fabricate reliably. On the contrary, double barrier structures of SINIS and SIS'IS type can result in intrinsically shunted junctions that exhibit overdamped RSJ like characteristics with reproducible and very large j_c in the range of $100\,{}^{\mathrm{kA}}/_{\mathrm{cm}^2}$ [140, 141]. The latter property arises from the fact that the impact of pinhole defects on the device performance, as occurring in very thin tunnel barriers (I), is minimized by the presence of two barriers.

In the case of ferromagnetic barriers (F), the transition from a SIFS junction to SIsFS can also have a drastic effect on j_c. A theoretical study, which is consistent with first experiments, has been published for the sequence $\mathrm{Nb}\,|\,\mathrm{AlO_x}\,|\,\mathrm{Nb}\,|\,\mathrm{Pd_{99}Fe_1}\,|\,\mathrm{Nb}$ [138]. The alloy $Pd_{99}Fe_1$ was studied due to its soft magnetic properties that make it appealing for a magnetic switching of the Josephson current [142]. The theory classifies SIsFS junctions into three different regimes, depending on the thicknesses of the s-layer (d_s). Junctions with a small d_s shall behave like an SIFS junction. They shall exhibit a heavily F-layer thickness (d_F) dependent damping of j_c and superimposed oscillations which are associated to 0–π transitions [80]. For similar SInFS structures with a normal metal n-layer of 2 nm thickness such transitions have already been observed in experiments [95]. When d_s becomes larger, superconductivity shall evolve in the interlayer and the damping of j_c by the ferromagnet decreases. Finally ,for d_s in the range and above the superconducting coherence length ξ_s, the SIs and sFS barriers can be considered to be separated. In this case, the overall j_c of the junction is governed by the barrier which has the lower value. In particular 0 and π parts with the same maximal

j_c should exist adjacent to the first 0–π transition. An important fact is that in calculations the transition from 0 to π exists for the whole range of interlayer thickness with only a marginal shift towards larger d_F while d_s increases.

The experimental verification of the latter aspect would provide an enormous increase in the critical voltage $I_c R_N$ of π Josephson junctions and facilitate their application in circuitry.

3.4.2 F-Layer Thickness (F-wedge)

A systematic experimental study on SIsFS junction about the influence of the layer thickness of s-layer (d_s) and F-layer (d_F) on the electrical characteristics is presented in the following. Nb' | AlO_x | Nb | $Ni_{60}Cu_{40}$ | Nb junctions were fabricated with various $Ni_{60}Cu_{40}$ layer thicknesses d_F on a single wafer by a static wedge approach (cp. sec. 2.2). The deposition rate r at the border of a circular sputter target is known to cease monotonically with increasing distance from the target center x. A calibration of the $Ni_{60}Cu_{40}$ deposition rate at different points across the wafer was determined from X-Ray reflectivity measurements of the layer thickness as shown in Fig. 3.16. The deposition rates varied between 0.5 Å/s and 4.5 Å/s. So junctions with d_F between 1 and 9 nm in steps of 0.08 nm were produced in parallel on a single wafer. At first, the low roughness Nb' bottom electrode was deposited as the sequence 3×[Nb(40 nm) | Al(30 nm)] | Nb(40 nm) | Al(7 nm) [119]. Then the I-barrier was formed by oxidisation of the top Al layer in a pure oxygen atmosphere at 10^{-2} mbar for 30 min. The resulting AlO_x layer leads to SIS junctions with $j_c = 7\,\mathrm{kA/cm^2}$ at 4.2 K. A Nb s-layer, a $Ni_{60}Cu_{40}$ F-layer and 40 nm Nb completed the sandwich structure. Detailed fabrication parameters of the sequence are shown in Appendix A.2. Several wafers with variations in the Nb spacer layer thickness d_s were processed, keeping all other parameters constant. Especially the F-layer wedge is the same for all wafers. Therefore a series of junctions from one of these wafers is denoted as *F-wedge* in the following (Fig. 3.15).

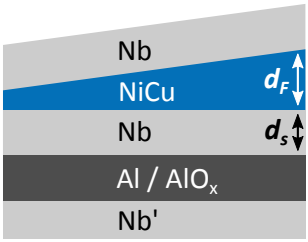

Figure 3.15 Layer sequence of F-wedge wafer

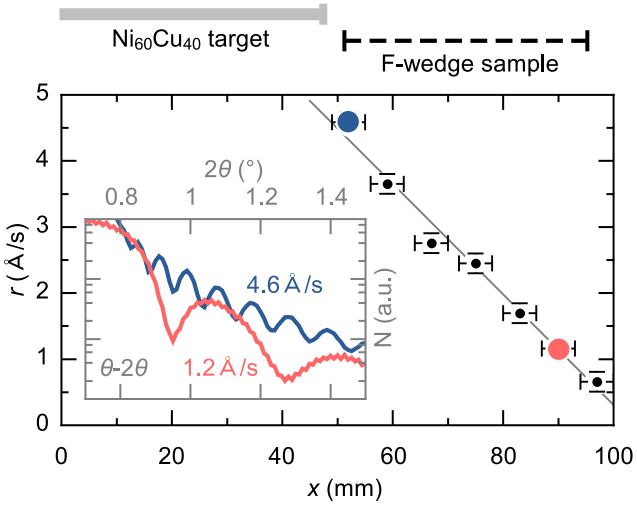

Figure 3.16 $Ni_{60}Cu_{40}$ rate r on the sample holder with respect to radial separation from the sputter target center x. Region of the target and substrate position indicated above the plot. Inset shows associated X-Ray reflectivity data. (adapted from [135])

Individual junctions were wire bonded and characterised in a liquid helium dipstick (sec. 2.4) at 4.2 K if not stated otherwise. The undefined magnetisation of the $Ni_{60}Cu_{40}$ layer at initial cooling to low temperatures leads to unstable electrical characteristics as expressed in non-Fraunhofer $I_c(B)$ and non-representative $I(V)$. However, it was possible to establish a measurement procedure that reproducibly resulted in defined $I_c(B)$ and $I(V)$ curves. The application of a damped oscillating magnetic field sweep along the junction width, starting at a maximum amplitude of 20 mT, at a temperature in the range of 10 K and 15 K restored Fraunhofer $I_c(B)$ characteristics (Fig. 3.17). It must be noted that a remanent magnetisation of the layer can provide a self field that offsets the $I_c(B)$ pattern along the axis of applied magnetic field. So the maximum value of the critical current I_c was not read at zero applied field but at the main lobe of the $I_c(B)$ curve.

Representative $I(V)$ for SIsFS junctions in the range of $d_s \leq 60$ nm

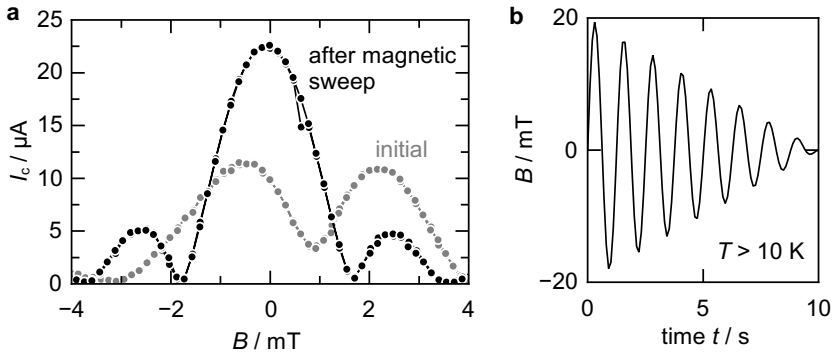

Figure 3.17 Measurement procedure to acquire I_c of JJs. [nr02id] **a** An initially distorted $I_c(B)$ curve becomes Fraunhofer-like after the application of **b** a damped oscillatory magnetic field sweep.

and $d_F \leq 9\,\text{nm}$ are presented in Fig. 3.18. For SIFS-type junctions, j_c is heavily reduced by the presence of the F-layer. On the other hand SIsFS with $d_s = 30\,\text{nm}$ show SIS-like behaviour with the same j_c, a strong hysteresis and a well pronounced signature of the superconducting gap voltage for all d_F. The only impact of a larger d_F is a rise in the subgap resistance. However, this effect completely vanishes at $d_s = 60\,\text{nm}$. For d_s from 10 nm to 20 nm a mixture between SIFS and SIS like characteristics is observed. Fraunhofer-like $I_c(B)$ dependence indicated a homogeneous current transport for all junctions and served as an indicator for a reference magnetisation state, as achieved by the measurement procedure described above. The $I(V)$ curves were recorded with an applied magnetic field B to compensate the magnetisation of the F-layer. It was chosen such that I_c is maximized. The normal resistance R_N was extracted as the average slope of the $I(V)$ curve between 3 mV and 4 mV. For F-wedge junctions with a size of $10 \times 10\,\text{um}^2$ R_N was constant for a given wafer, i.e. independent of d_F. However, R_N decreased as $0.4\,\Omega$, $0.25\,\Omega$ and $0.16\,\Omega$ for d_s increasing from 0 nm over 10 nm to 30 nm, respectively. Commonly, the I_cR_N product is shown as a characteristic quantity which also accounts for different junction sizes. In this thesis however, the critical current density $j_c = I_c/A$ (A: junction cross section) is presented

as a universal property of the junction stack. It is suited to compare different junctions and wafers, but a minor impact from the systematic variations in R_N has to be kept in mind.

The dependence of j_c on d_F for several sets of junctions with different d_s is shown in Fig. 3.19. A strong damping of j_c with d_F and a characteristic 0–π transition as evident for $d_s = 0\,\text{nm}$ (SIFS) prevails up to $d_s = 11\,\text{nm}$. However, the $I(V)$ dependence is shifted towards the upper right, i.e. j_c increases overall and the point of 0–π transition increases from $d_F = 5.8\,\text{nm}$ by about 1 nm. With d_s rising to 13 nm and 19 nm the critical current rises drastically and the 0–π transition can not be resolved anymore within the range of investigated d_F. In addition, the junction characteristics show instabilities and become sensitive to the history of magnetic treatment. Finally, for d_s of 30 nm and 60 nm the $j_c(d_F)$ level at a value which is defined by the j_c of the SIs part of the junction.

Error margins are not shown in the plot but will be discussed here. The determination of the critical current density j_c depends on the precision of current measurement and the fabrication tolerance of the junction area. However, the large dynamics and sharp cusps in j_c which become clearly visible on the logarithmic scale render both errors irrelevant. A comment on the precision d_F distinguishes between the comparability of data points and the absolute error of the physical quantity. The former does not rely on the d_F thickness calibration except the requisite of a monotonic and rather linear rate gradient across the junctions on the wafer. Given these properties consecutive junctions of an F-wedge wafer accurately represent a grading in d_F. All the F-wedge wafer were fabricated with the same deposition parameters for the F-layer. With an assumed positioning accuracy of $\pm 3\,\text{mm}$ of the wafer below the target, a possible d_F offset between junction sets from different wafers of $\pm 0.5\,\text{nm}$ is introduced. Finally, the determination of the thickness d_F from the junction position on the wafer introduces another error but this applies collectively for all wafers. The calibration is only relevant for the scaling of the x-axis of Fig. 3.19 and does not affect the relative positions of datapoints. So the calibration is not essential for conclusions based on the comparison of datasets.

The experimental results on SIsFS junctions nicely resemble the theoretically predicted $j_c(d_F)$ (sec. 3.4.1). An increase of d_s does enhance j_c

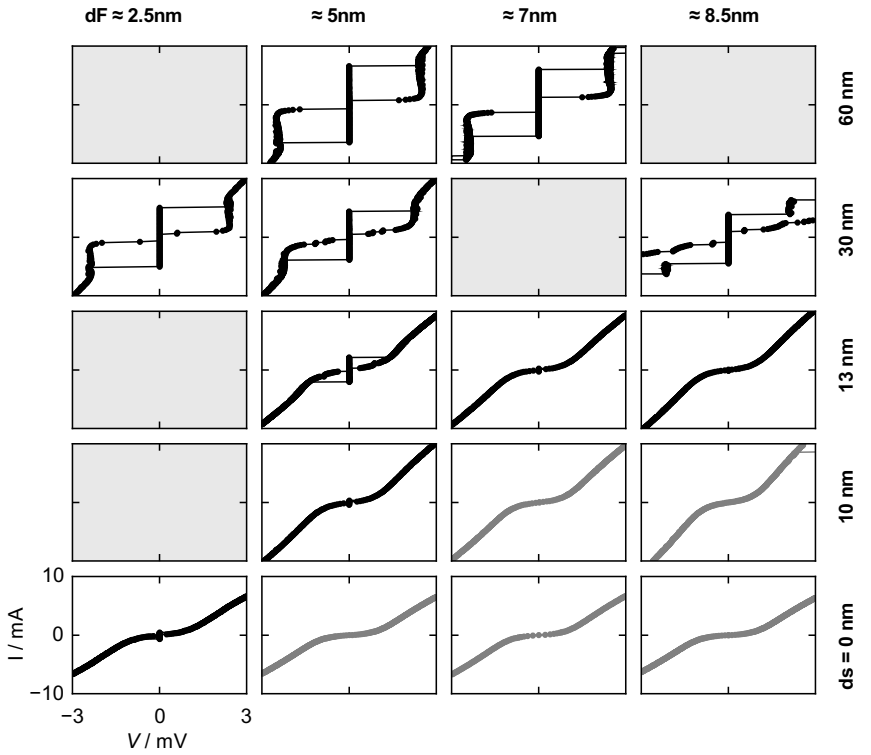

Figure 3.18 Current–voltage characteristics $I(V)$ with identical scales for SIsFS junctions with different layer thicknesses d_s (vertical) and d_F (horizontal). The real d_F of the junctions may vary by $\pm 0.5\,\mathrm{nm}$ around the indicated value. Some curves especially with large I_c are hysteretic (black), others are single-valued (gray). All junction areas are $10 \times 10\,\mu\mathrm{m}^2$. The j_c of the junctions are also shown in Fig. 3.19. [nr02$^{\mathrm{id}}$] [s18$^{\mathrm{id}}$] [s21$^{\mathrm{id}}$] [s16$^{\mathrm{id}}$] [s14$^{\mathrm{id}}$]

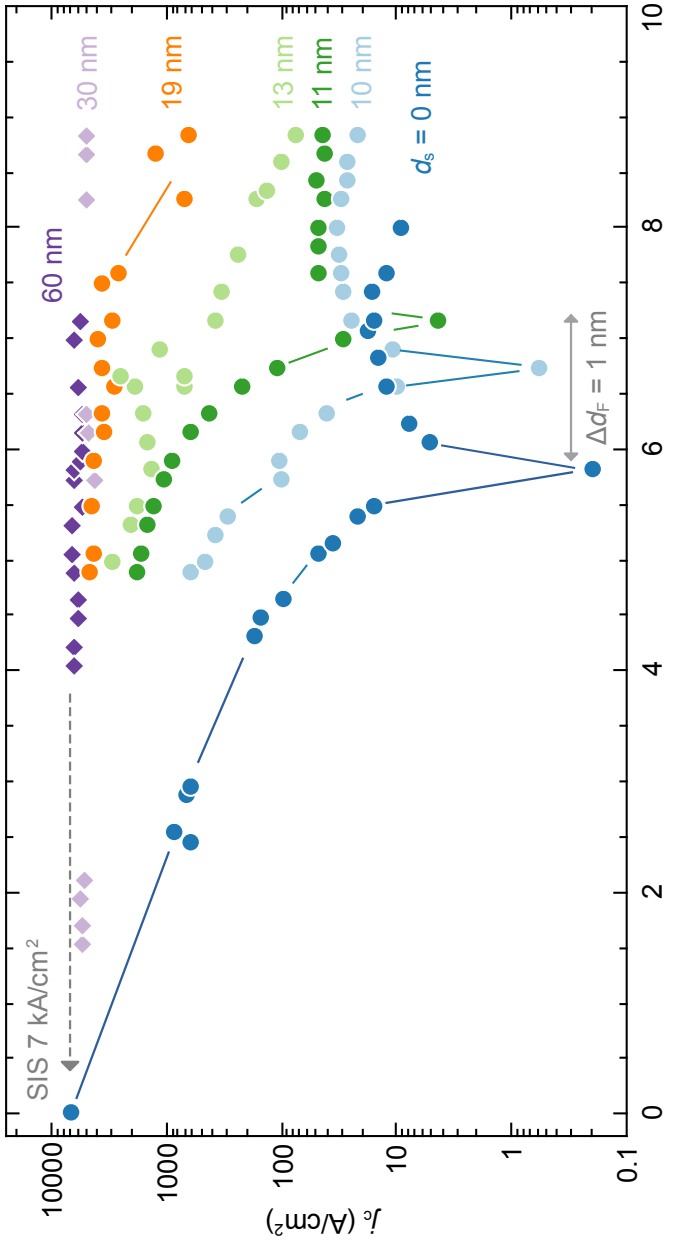

Figure 3.19 Critical current density j_c vs. d_F for sets of SIsFS junctions with different d_s (F-wedge). Up to $d_s = 11$ nm a 0–π transition is resolved in the measurement which shifts by $\Delta d_F = 1$ nm. Error margins are commented in the text. (adapted from [135]) [nr02id] [s18id] [s24id] [s21id] [s25id] [s16id] [s14id]

Table 3.2 Josephson junction parameters from publications (*calculated value)

T/K	A/um^2	j_c/A/cm^2	I_c/mA	R_N/mΩ	I_cR_N/μV	junction type
4.2	10×10	**7000**	–	300	***2100**	0-SIS [135]
–	–	**4500**	–	–	**1300**	0-SIS [125]
4.2	10×10	50	–	300	*15	π-SIsFS [135]
2	50×50	22	–	50	28.3	π-SIFS [97]
1.5	1000×1000	*0.01	–	$40 - 200$	≈ 18	π-SIFS [89]
–	10×10	***10000**	10 mA	0.1	*1	π-SFS [92]
–	10×10	**1000**	–	0.2	*0.2	π-SFS [94]
1.5	50×50	–	10 μA	0.01	10^{-4}	π-SFS [67]

for all d_F up to a limit that is defined by the SIs part of the junction. Also the clear shift of the 0–π transition towards larger d_F by the insertion of the s-layer follows theoretical models [143]. In these calculations, SInFS junctions are investigated, which also seem to be a suitable description for SIsFS junctions with d_s well below the superconducting coherence length. The junctions exhibit a significant shift of the 0–π transition towards larger d_F with the thickness of the n-layer d_n only for I-barriers with a certain resistance. Also the shift occurs rather abruptly with the emergence of a finite d_n and does not shift much further with increasing d_n. These findings are in good agreement to the experimental results in this thesis. However as a significant discrepancy to the predictions, a 0–π transition was not resolved for all $d_s > 11$ nm. The disappearance of this essential experimental signature is accompanied with suddenly arising distortions in the junction characteristics and a significant increase of j_c. It is possible that these effects obscure a transition which, according to theory, becomes increasingly narrow for larger d_s. An alternative explanation, excluding the possibility that the transition vanishes completely for all d_F, is a shift to $d_F > 9$ nm. However, no sign of an emerging adjacent transition dip is found in the measurements.

As mentioned earlier, a large I_cR_N product is desirable for applications. For a benchmark, π Josephson junction parameters of representative Nb-based Josephson junctions were extracted from publications and summarized in Tab. 3.2. Although not specified everywhere, the junction

temperature is expected to be at or below liquid helium temperature. Today SIS junctions reliably reach $I_cR_N = 1\,\text{mV}$ to $2\,\text{mV}$ with critical current densities of several $^{\text{kA}}/_{\text{cm}^2}$ in the laboratory and at the industrial scale. Despite the use of different ferromagnetic alloys as F-layer, e.g. NiCu, PdFe or PdNi, the performance of the ferromagnetic junctions was mainly governed by the layer sequence. Obviously the maximum I_cR_N product of π junctions with ferromagnetic layers is still 2 orders of magnitude smaller than for 0-SIS junctions. The reason is a tradeoff between j_c and R_N. Only individually both values can reach parameters in the range of 0-SIS junctions. π-SFS junctions can exhibit a large j_c at the cost of a vanishing R_N. Vice versa π-SIFS show a drastically decreased j_c at reasonable R_N. All the SIFS Josephson junctions yield a comparable value of I_cR_N which scarcely depends on the oxidisation conditions of the I-barrier due to its reciprocal impact on critical current and barrier resistance. The SIsFS approach decouples both parameters and allows to individually tailor R_N by means of the I-layer thickness and j_c by the s-layer thickness. This work demonstrates that the j_c in SIsFS junctions can be adjusted in the range between the corresponding SIFS and SIS junction for all d_F up to 9 nm.

3.4.3 s-Layer Thickness (s-wedge)

A finer investigation of the dependence of SIsFS junction properties on d_s is intended to further characterise the enormous difference of j_c between ferromagnetic SIFS and SIsFS junctions. Therefore a second batch of SIsFS wafers was fabricated, each exhibiting the same wedge of d_s and constant d_F. Series of junctions from such a wafer with variations in d_s are called s-wedge in the following (Fig. 3.20). The fabrication procedure deviated from the F-wedge only for the barrier of the wafers, i.e. the layers s, F and I. As s-layer a Nb wedge was statically deposited with a rate varying from $0.75\,^{\text{nm}}/_{\text{s}}$ to $4\,^{\text{nm}}/_{\text{s}}$ over 5 cm in the center of the wafer. A $Ni_{60}Cu_{40}$ layer with constant thickness was deposited dynamically with 2 rotations in

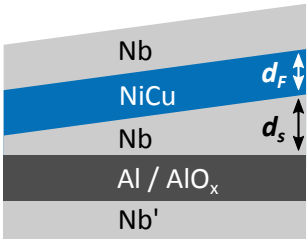

Figure 3.20 Layer sequence of s-wedge wafer

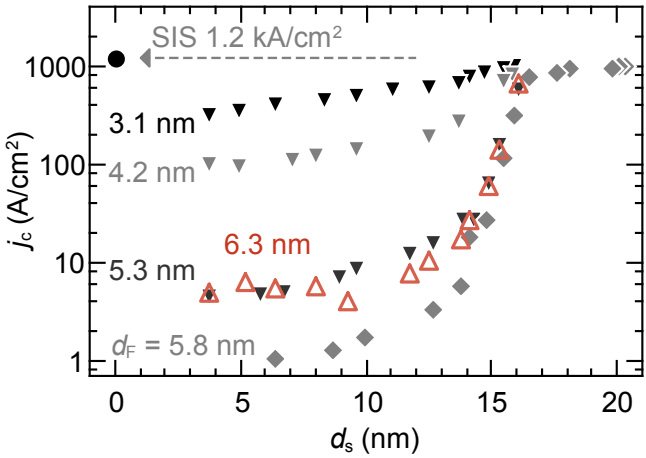

Figure 3.21 Critical current density j_c vs. d_s for sets of SIsFS junctions with different d_F (s-wedge). The I-barrier is fabricated by oxidisation of Al in pure oxygen (0.1 mbar / 30 min). (adapted from [135]) [s39id] [s36id] [s34id] [s29id] [s35id]

the deposition chamber. An enhancement of the I-barrier oxidisation to 10^{-1} mbar for 30 min reduced the maximum critical current of the junctions to $1.2\,^{\mathrm{kA}}/_{\mathrm{cm}^2}$. This facilitated the measurement of j_c over the large range of values with the same junction type and area. The majority of data was acquired from $50 \times 10\,\mu\mathrm{m}^2$ junctions.

Experimental $j_c(d_s)$ dependences in the range of $3\,\mathrm{nm} \leq d_s \leq 20\,\mathrm{nm}$ for various d_F between 3.1 nm and 6.3 nm are shown in Fig. 3.21. At $3\,\mathrm{nm} < d_s < 13\,\mathrm{nm}$ the curves are rather flat but their values strongly depend on d_F. Between $d_F = 3.1\,\mathrm{nm}$ and 5.8 nm the critical current density drops by two orders of magnitude and increases again at $d_F = 6.3\,\mathrm{nm}$. From $d_s = 13\,\mathrm{nm}$ to 16 nm the critical current density rises and converges for all curves at a collective limiting value, which persists for larger d_s and is defined by the j_c of the SIs part of the junction stack. The increase can be steep and reach up to two orders of magnitude within $\Delta d_s = 3\,\mathrm{nm}$.

Despite the different AlO_x oxidisation pressures and calibrations for the layer thickness of s-wedge and F-wedge junctions, the characteristic

features of the $j_c(d_s)$ dependence (Fig. 3.21) consistently fit to the $j_c(d_F)$ dependence (Fig. 3.19). Both sets of curves resemble shapes that can be inferred from each other. Both, the 0–π transition around $d_F = 6\,\text{nm}$ for $d_s < 10\,\text{nm}$ and the significant increase of j_c in the range $13\,\text{nm} < d_s < 20\,\text{nm}$ are well resolved. However, the maximum j_c of the sets of junctions is clearly limited by the SIs part of the stack. These conclusive experimental findings support the claim that the overall behaviour of the junctions is not affected by the change in the I-barrier thickness.

Contrary to expectations from F-wedge, where the 0–π transition significantly shifts towards larger d_F for d_s emerging up to 10 nm, in s-wedge no indication for such a shift can be found. Especially the s-wedge series with $d_F = 6.3\,\text{nm}$, directly above the d_F induced 0–π transition, should show a d_s induced transition by a characteristic dip. The experimental $j_c(d_s)$ curves for different d_F closely follow calculated curves which differ by the magnetic exchange energy h instead [137]. Close to the h induced 0–π transition an anomalous curve is produced by the calculations showing a minimum at finite d_s. In this regime the experimental data curve also exhibits signs for a shallow minimum. It is plausible that in experiments the parameter d_F has the same influence on the curves as the parameter h in the calculations. According to (1.45), the magnetic exchange energy and the layer thickness d_F have an equivalent effect on the parameter oscillation in the ferromagnet. Therefore variations of each quantity should equally allow to induce a 0–π transition of the junctions.

3.4.4 Superconductivity in s-Layer

In the preceding section a drastic impact of the s-layer on the electrical characteristics of SIsFS junctions has been revealed. To study superconductivity in these thin Nb interlayers, temperature measurements were performed. The temperature of the JJs was monitored by a sensor that was mounted in the vicinity of the junction. Temperatures above liquid helium (4.2 K) were set by placing the junction in the helium gas above the liquid helium surface. In the unperturbed gas the temperature rises with increasing height from the helium surface. Care was taken to ensure an equal height of junction and sensor within a few mm in order to avoid

errors in the temperature reading. A temperature change from 4.2 K to 10 K required to lift the junctions by about 10 cm.

Figure 3.22 shows $j_c(T)$ curves for various SIsFS junctions with d_s in the range between 12.5 nm and 22.5 nm from an s-wedge wafer with $d_F = 5.3$ nm. For comparison a SIS reference junction is also presented which follows the Ambegaokar-Baratoff relation. At lower temperatures all curves exhibit a convex curvature. In contrast to SIS however, the SIsFS curves develop a concave curvature at the temperatures where j_c drops to zero. In general, with falling d_s the $j_c(T)$ dependencies shift towards smaller temperatures and reduce in magnitude. Between 5 K and 6 K the contact of the sample holder with the liquid helium can create turbulence which make the temperature fluctuate. In this case, a collective thermalisation of sample and sensor is not possible leading to loops of erroneous datapoints. For clarity these are not shown which causes small discontinuities in the curves. A critical temperature $T_c = 8.4$ K is extracted from kinks to $j_c = 0$ in the measurements. It is attributed to the the top weaker electrode of the junction. Since the electrodes of all wafers were fabricated with the same properties, the feature can be taken as a common reference temperature. The small variance of T_c in the different measurements confirms that the curves can be compared directly without an individual offset correction for the temperature axis.

Another critical temperature $T_c{}^*$ is defined by a linear extrapolation of the falling curve to zero current. With decreasing d_s the value of j_c is reduced overall and $T_c{}^*$ becomes smaller (Fig. 3.23). Although $T_c{}^*$ can not be determined for $d_s \leq 14$ nm the data suggests a value below 4.2 K. These findings consistently fit to the $j_c(d_s)$ of the same junction (cp. Fig. 3.21). Around $d_s = 15$ nm the j_c changes significantly, having a constant maximum value for larger d_s and getting smaller for smaller d_s. It is plausible that $T_c{}^*$ is linked to the emergence of superconductivity in the s-layer as claimed by theory [138]. In this regard the SIsFS junctions behave similar to non-magnetic SIsIS and SInIS Josephson junctions [141].

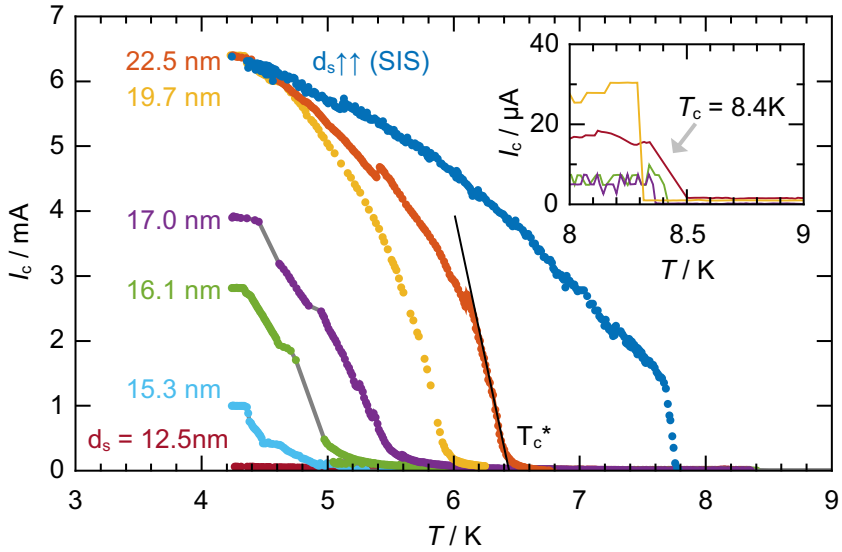

Figure 3.22 $I_c(T)$ for SIsFS junctions with different d_s and $d_F = 5.3\,nm$, the linear extrapolation of a curve to zero current defines T_c*; inset shows critical temperature T_c of the weaker electrode. [s34id]

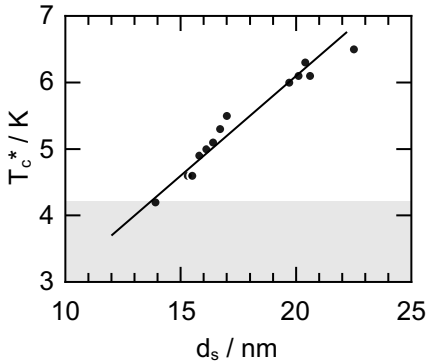

Figure 3.23 Critical temperature T_c* vs. s-layer thickness d_s of SIsFS junctions with d_F=5.3 nm. Line is a guide to the eye. Gray area not accessible with experimental setup.

3.4.5 Stepped 0–π Junctions

Further information about the occurrence of SIsFS π junctions was acquired from JJs with partially etched F-barriers. By the use of etching techniques the effective F-layer thickness of a junction can be reduced overall or partially for a certain area of the barrier [144]. In fabrication, a SIsFS layer stack with various d_F was deposited across the wafer resulting in several sets of junctions with the same F-wedge. The sets exhibited $d_s = 11\,\mathrm{nm}$ and an identical range of d_F. For some sets of junctions, sections of the Nb cap, which protects the barrier, were removed selectively by lithography and etching by RIE in pure SF_6 gas. The bare parts of the F-layer were subsequently exposed to an etching RF-plasma (50 W, 30 s, 25 sccm) in the load lock of the sputtering system and finally covered again with sputter deposited Nb. After completion of the wafer three different sets of junctions were investigated. One was non-etched, another semi-etched and a third fully-etched, e.g. the fractions of etched F-layer area are 0 %, 50 % and 100 %. At 50 % the border between the sections splits the junction width in half.

Fig. 3.24 compares $j_c(d_F)$ for non-etched (0 %) and fully-etched (100 %) junctions. The non-etched junctions represent a part of the $j_c(d_F)$ above the 0–π transition which is located at $d_F = 7\,\mathrm{nm}$ in agreement to Fig. 3.19. JJs with 100 % etching show a significant increase of j_c. If a reduction of the effective d_F by $-2\,\mathrm{nm}$ is assumed the data points readily fit to the branch of j_c below the 0–π transition. Another hint that etching of the F-layer can cause a crossing of the 0–π transition appears in the $I_c(B)$ curves for various etching fractions (Fig. 3.25). Junctions with deposited $d_F = 9\,\mathrm{nm}$ show a Fraunhofer shape, the same periodicity and equal critical current densities at 0 % and 100 %. The center of all $I_c(B)$ patterns is shifted on the magnetic axis due to a remanent magnetization of the barrier layer. A fundamentally different behaviour is observed for 50 % junctions. Compared to uniform barriers, these show a distinctive dip in the center of the $I_c(B)$ pattern and the periodicity of the lobes is doubled. Such a pattern is characteristic for a Josephson junction with 0 and π parts of symmetric geometry that exhibit the same absolute value of the critical current I_c [145]. The strong reduction of the critical current in the center of the pattern is caused by the cancellation of I_c from the 0–part and $-I_c$ from the π–part of the junction. These findings

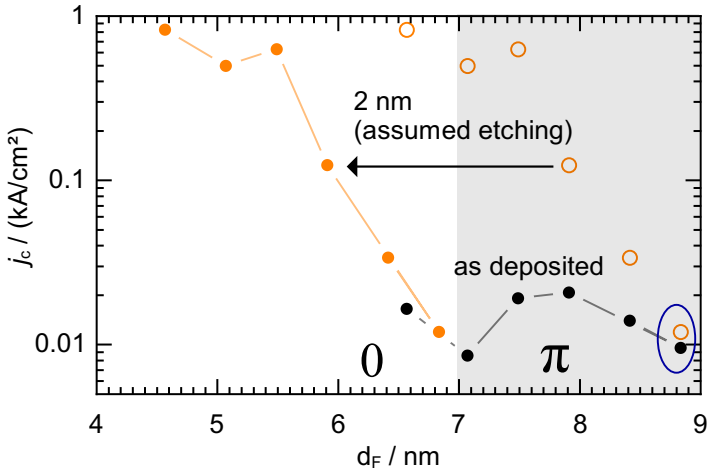

Figure 3.24 Critical current density j_c versus F-layer thickness d_F for SIsFS junctions with various etching of the F-layer. Junctions without etching are shown as (•), JJs with 100 % etching are plotted with d_F as deposited (○) and additionally with an assumed F-layer etching depth of -2 nm (●) suitably placing the datapoints on the falling branch before the 0–π transition. For the highlighted junctions $I_c(B)$ patterns are presented in Fig. 3.25. [s32id]

are another indicator that SIsFS junctions with $d_s = 11\,\mathrm{nm}$ undergo a transition from 0 to π at around $d_F = 7\,\mathrm{nm}$.

3.5 Contribution to State of Science

This thesis presents experiments that exceed previous works in various aspects. For most of the layer sequence, only isolated junctions have been published before. The systematic study of junction characteristics in dependence on different layer parameters resulted in novel insight. The following contributions are in particular beneficial and improve the state of science.

SIsFS First fabrication and systematic experimental characterisation of $\mathrm{Nb}\,|\,\mathrm{AlO_x}\,|\,\mathrm{Nb'}\,|\,\mathrm{Ni_{60}Cu_{40}}\,|\,\mathrm{Nb}$ junctions with well calibrated layer thickness and a broad range of s-layer and F-layer thickness. The junctions reveal a large dynamics in the critical current, caused by the s-layer thickness. The experimental data is in good agreement to previous theoretical predictions.

π junctions in SIsFS Although a drastic enhancement of the j_c of ferromagnetic Josephson junctions has been revealed, no signature of a π junction with extraordinary large j_c could be found.

Superconductivity in s-layer of SIsFS The considerable influence of the s-layer onto SIsFS junctions could be linked to the emergence of superconductivity in this layer with increasing d_s.

Si and Fe based Josephson barriers Investigation of Josephson junctions with $\mathrm{Si}_{1-\delta}\mathrm{Fe}_\delta$ based barriers for a range of Fe-layer thickness, Si-layer thickness, layer sequence and δ. The distribution of Fe in the Si matrix was found to have little impact. A strong suppression of superconducting correlations occurs in all cases, that were studied, for an accumulated Fe-layer thickness of 2 nm.

Combinatorial sputtering in planetary systems A novel combinatorial sputtering technique to create material libraries with orthogonal gradients in planetary sputtering systems was implemented.

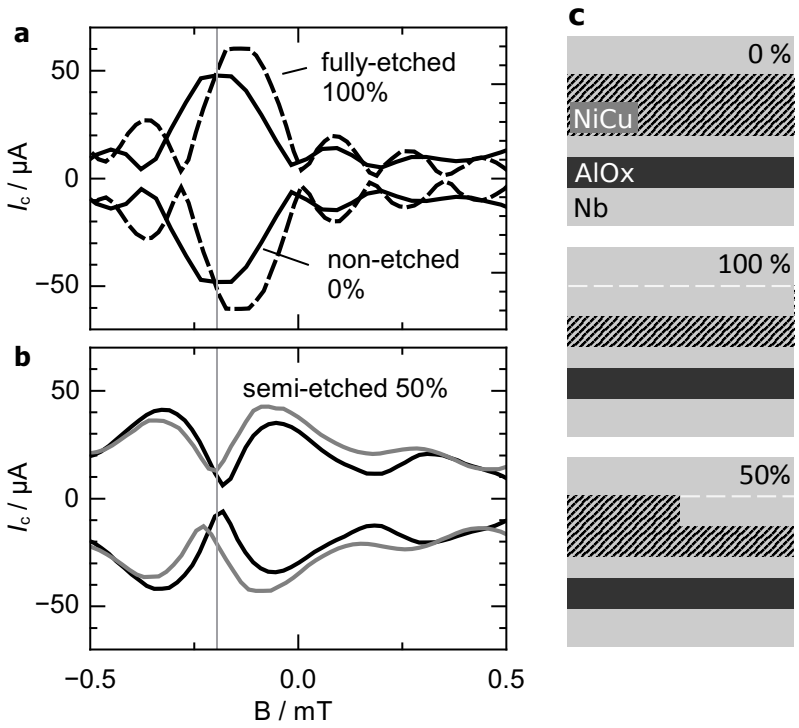

Figure 3.25 $I_c(B)$ dependence for SIsFS JJs with different fractions of etched F-layer area. **a** non-etched (—) and fully-etched (- - -) JJs show a Fraunhofer pattern and similar I_c. **b** two half-etched JJs yield a pattern which is distinctive for a junction with symmetric 0 and π parts. **c** sketch of the junction stack cross-section without (0 %) and with full etching (100 %) and semi-etched F-layer (50 %). [s32/0^{id}]

Independent adjustment of I_c and R_N The experimental data on ferromagnetic SIsFS junctions provides parameters for their integration into RSFQ circuits. They allow an independent modification of I_c and R_N. The results enhances the compatibility of ferromagnetic junctions to circuits and was impossible with existing SFS and SIFS junctions.

The fundamental research character of the presented experiments leads to only a small direct benefit for applications. However it could pave way to enhance the I_cR_N product of π Josephson junctions. Such junctions could enhance the operation parameters not only of conventional superconducting electronics but also in the implementation of solid state qubits. However, it most be noted that a feasible implementation for a quantum simulator or universal quantum computer is not available. The realisation of such a machine still requires to overcome enormous obstacles. A π junction with large j_c, as studied here, is only a minor aspect and might disqualify due to other shortcomings.

Conclusion

The presence of ferromagnetic material in the barrier of a Josephson junction significantly influences the correlations between the superconducting electrodes. In particular, it can lead to π Josephson junctions with an intrinsic phase slip of π across the junction. Provided that suitable electrical characteristics, comparable to conventional Josephson junctions, can be achieved such π devices could significantly increase the performance of superconducting electronic circuits and solid state quantum bits.

In this thesis, two distinct approaches to achieve thin film π Josephson junctions with large values of the critical current density j_c and the $I_c R_N$ product were experimentally investigated and discussed. It was shown that the critical current damping in a binary barrier, made from Si and Fe, is dominated by the absolute amount of Fe in the barrier and does not depend on its distribution along the surface normal direction. Using a newly implemented combinatorial sputtering technique, junctions with $Si_{1-\delta}Fe_\delta$ barriers were produced on one wafer, allowing an independent variation of barrier thickness and composition. Despite investigations of the critical current for a range of these barrier parameters, no indication for a π junction was found.

In a second study SIsFS junctions, comprising an AlO_x tunnel barrier (I) and a $Ni_{60}Cu_{40}$ ferromagnetic layer (F), were investigated. A comparison of existing π junctions in SFS and SIFS technology suggests that variations in the tunnel barrier transparency only modify j_c of the junctions, but do not change the value of $I_c R_N$. In contrast and in agreement to theory, a substantial enhancement of j_c at constant R_N by up to 3 orders of magnitude was observed in $Nb\,|\,AlO_x\,|\,Nb\,|\,Ni_{60}Cu_{40}\,|\,Nb$ (SIsFS) junctions where I-layer and F-layer are separated by a thin Nb layer of thickness d_s. A d_F-induced 0–π transition has been detected for samples with d_s up to 11 nm. With increasing d_s, the transition monotonously shifts from $d_F = 6$ nm to larger values by up to 1 nm and j_c is increased

overall. A maximum value of $j_c = 50\,\mathrm{A/cm^2}$ has unambiguously been detected for an SIsFS π junction. At $d_s > 13\,\mathrm{nm}$, the transition can not be resolved anymore and a drastic enhancement of j_c with increasing d_s has been observed. At $d_s = 30\,\mathrm{nm}$, SIS like behaviour and values of j_c are observed for d_F in the range between 2 nm and 9 nm. The drastic change in the junction behaviour is apparently linked to the evolution of superconductivity in the s-layer.

Scientific Vita

Nico Himmel, geb. Ruppelt

2005 – 2010	Dipl. Physics program at Christian-Albrechts-University of Kiel (CAU), Diploma thesis at the Institute of Experimental and Applied Physics (IEAP) "Scanning Tunneling Microscopy of Fe Thin Films, Magnetic Point Contacts and Organometallic Molecules"
2008 – 2009	Visiting student at University of Bath (UK)
12/2010 –	Member of the chair of Nanoelectronics (Prof. Kohlstedt), Technical faculty CAU

Publications

D. M. Heim, N. G. Pugach, M. Y. Kupriyanov, E. Goldobin, D. Koelle, R. Kleiner, N. Ruppelt, M. Weides, und H. Kohlstedt, "The effect of normal metal layers in ferromagnetic Josephson junctions", arXiv:1310.0567v2 [cond-mat.supr-con] (2014).
(submitted to New Journal of Physics)

N. Ruppelt, H. Sickinger, R. Menditto, E. Goldobin, D. Koelle, R. Kleiner, O. Vavra, und H. Kohlstedt. "Observation of 0–π transition in SIsFS Josephson junctions", Appl. Phys. Lett. **106**, 022602 (2015).

N. Ruppelt, O. Vavra, H. Sickinger, E. Goldobin, D. Koelle, R. Kleiner, und H. Kohlstedt, "Combinatorial sputtering in planetary type systems for alloy libraries with perpendicular gradients of layer thickness and composition realised by a timing approach", Appl. Phys. A **116**, 229–232 (2014).

E. Goldobin, H. Sickinger, M. Weides, N. Ruppelt, H. Kohlstedt, R. Kleiner, und D. Koelle, "Memory cell based on a φ Josephson junction", Applied Physics Letters **102**, 242602 (2013).

N. Néel, S. Schröder, N. Ruppelt, P. Ferriani, J. Kröger, R. Berndt, und S. Heinze, "Tunneling Anisotropic Magnetoresistance at the Single-Atom Limit", Phys. Rev. Lett. **110**, 037202 (2013).

M. Ziegler, N. Ruppelt, N. Néel, J. Kröger, und R. Berndt, „Control of spin-polarized current in a scanning tunneling microscope by single-atom transfer", Appl. Phys. Lett. **96**, 132505 (2010).

Presentations

N. Ruppelt, O. Vavra, H. Kohlstedt, H. Sickinger, R. Menditto, E. Goldobin, R. Kleiner, D. Kölle "Transitions in SIS'FS Junctions 0–π Transitions in SIS'FS Junctions", Poster, Bad Herrenalp (2013)

N. Ruppelt, O. Vavra, H. Kohlstedt, H. Sickinger, E. Goldobin, R. Kleiner, D. Kölle "Josephson Junctions with Si|FM (ferromagnet) barriers", Poster, International Summer School on Superconductivity – Theory, Experiments, and Phenomena, Cargése (2013)

N. Ruppelt, O. Vavra, H. Kohlstedt, H. Sickinger, E. Goldobin, R. Kleiner, D. Kölle "Towards π Josephson Junctions with Fe and Si based barriers", Talk, DPG-Frühjahrstagung Kondensierte Materie, Regensburg (2013)

N. Ruppelt, O. Vavra, H. Sickinger, E. Goldobin, R. Kleiner, D. Kölle, H. Kohlstedt "Combinatorial Sputtering for low-Tc Josephson Junctions", Talk, Kryoelektronische Bauelemente, Freudenstadt (2012)

Table of Wafers

The experimental data in this thesis has been acquired with physical Josephson junctions. They unique wafer id is mentioned in the figure captions as [sXX^{id}]. The samples are stored in the AG Nanoelektronik, Technische Fakultät, Christian-Albrechts-Universität zu Kiel, Kaiserstr. 2, 24143 Kiel. A list of the wafer ids of relevant wafers is printed together with the page(s) (*italic numbers*) of their occurrence in this thesis.

A Planar Josephson Junctions

A.1 Layout

All Josephson junctions were fabricated in overlap geometry [146]. The sketch below shows a junction in cross-sectional and top-view. Also the four point wiring of the superconducting terminals is indicated. Although it may seem that two Josephson junctions are measured in series the contact to the lower electrode occurs through a much larger barrier area than the actual junction. This inevitably leads to pinhole and edge currents so that a suitable electrical connection to the bottom electrode is formed. The actual junction is surrounded and insulated by an anodic oxide. The magnetic field $\boldsymbol{B}$ threads the junction in the direction which is indicated by the arrow. The microscope image shows a topview of a $50 \times 10\,\mathrm{um}^2$ junction.

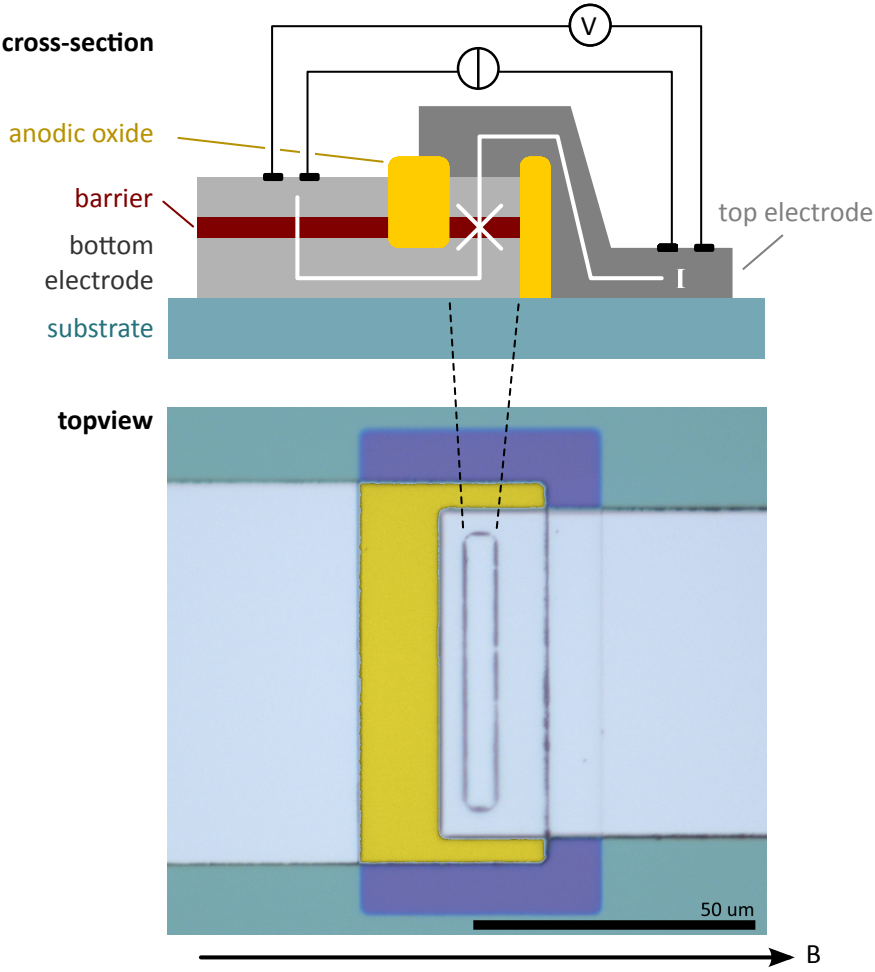

A.2 Recipe for SIsFS Junctions

The fabrication recipe for SIsFS junctions is listed below. The two batches of wafers differ by the steps 3a–5a (F-wedge) and 3b–5b (s-wedge). The wafers within a batch exhibit different s-layer thickness 4a (F-wedge) or F-layer thickness 5b (s-wedge).

Note: The process steps are the basis for all junctions in this thesis. To fabricate SIS junctions, the steps 4, 5 and 9 have to be omitted. Junctions with Fe and Si based barriers were prepared by replacing the steps 3–5.

	Step	Parameters
1	Lithography Trilayer	AZ5240E, image reversal
2	Sputter base electrode	Nb | Al' | Nb | Al' | Nb | Al' | Nb | Al Nb (360 W, 25 sccm Ar, 17 s) Al' (100 W, 40 sccm Ar, 60 s, 2 Rot) Al (100 W, 40 sccm Ar, 100 s, 3 Rot)
3a	Oxidisation	10^{-2} mbar (43 sccm O_2), 1800 s
4a	Sputter s-layer	Nb (4 s$\hat{=}$10 nm)
5a	Sputter F-wedge	$Ni_{60}Cu_{40}$ ($-15°$, 50 W, 20 sccm, 20 s)
3b	Oxidisation	10^{-1} mbar (80 sccm O_2), 1800 s
4b	Sputter s-wedge	Nb (10°, 600 W, 25 sccm, 5 s)
5b	Sputter F-layer	$Ni_{60}Cu_{40}$ (100 W, 20 sccm, 2 Rot , 60 s$\hat{=}$5.2 nm)
6	Sputter capping	1×Nb
7	Lift-off	
8	Lithography	AZ5240E
9	IBE + SIMS	etching down to AlO_x
10	Anodic oxidisation	ramp till 20 V at 10 V/s, further till 60 V at 1 V/s
11	Stripping	
12	Litho.	AZ5240E, image reversal
13	Ar cleaning	2 × 20 s, 200 W
14	Sputter top electrode	400 nm Nb

Essential steps of the tunnel junction fabrication process are sketched below. Each image shows the cross-section of the junction at a certain stage of the process. The numeric labels correspond to the fabrication steps, as defined in the table above.

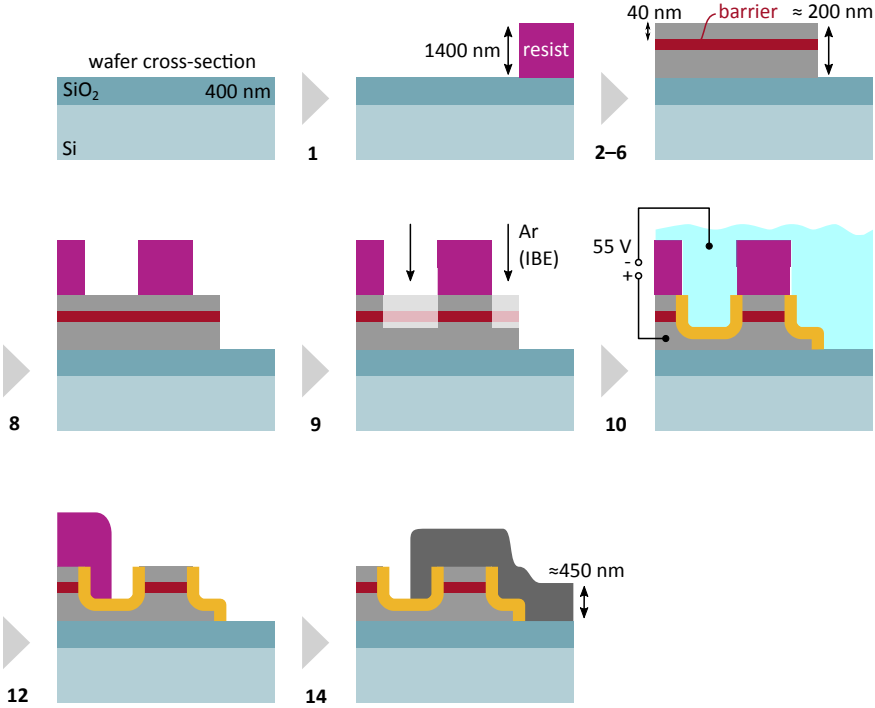

B Transmission Electron Microscopy – SiFe Alloy

Electron microscopy can image samples in real space and reveal crystallographic orientations in reciprocal space measurements. Furthermore chemical component analysis can be done with energy-dispersive X-Ray analysis (EDX). A $\mathrm{Nb}\,|\,\mathrm{AlO_x}\,|\,\mathrm{Si}_{1-\delta}\mathrm{Fe}_{\delta}\,|\,\mathrm{Nb}$ junction [FeSi5/F$^{\mathrm{id}}$] has been prepared to image the cross-sections in transmission. For preparation a slice is cut out of the chip and thinned down to a few 10 nm thickness by means of focused ion beam etching (FIB). The following electron microscopy data was acquired by V. Hrkac (AG Kienle, Technische Fakultät, CAU Kiel).

Cross-section The following scanning electron microscope picture resolves the atomic number of the atoms in brightness levels (Z-contrast). The wafer with atomically flat surface is located at the bottom, followed by the in-situ deposited trilayer and the metalization (wiring) on top.

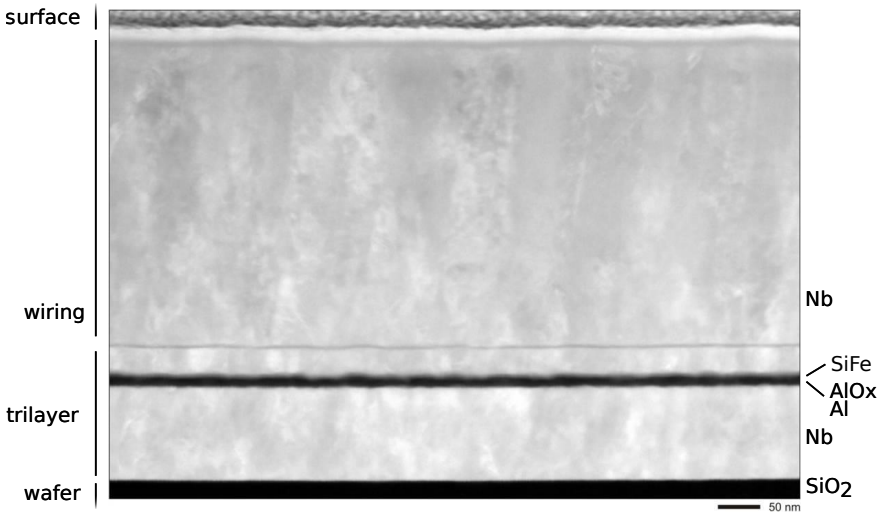

Barrier Cross-section A zoom into the barrier region in bright field mode shows a low roughness interface between $\mathrm{Al}\,|\,\mathrm{AlO_x}$ and $\mathrm{Si_{1-\delta}Fe_\delta}$. The Al layer exhibits a polycrystalline structure and nicely levels the surface roughness of the underlying Nb bottom electrode. The FeSi layer is amorphous and seems to be homogeneous in thickness and composition.

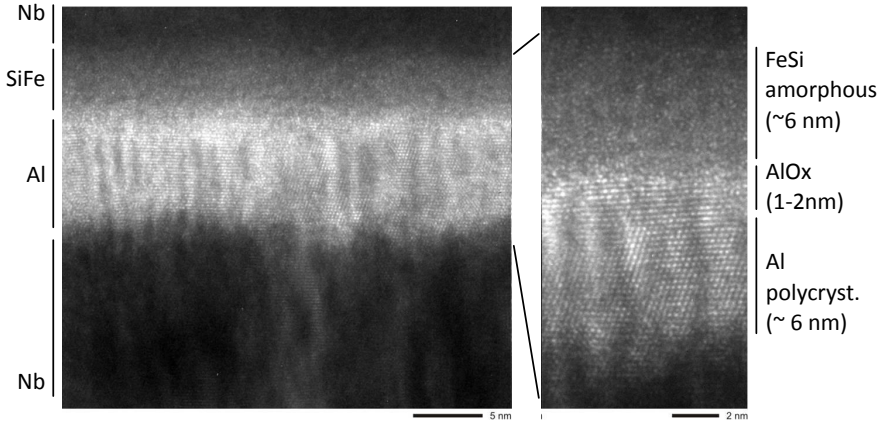

Elemental Composition Below an EDX linescan perpendicular to the barrier is shown. Starting in the upper electrode at 0 nm the coordinate spans the barrier region along the layer normal direction and reaches till the bottom electrode at 25 nm. The count contributions of the five elements Nb, Fe, Si, Al and O are displayed individually. As intended in the fabrication, the gap between the Nb electrodes is filled with a pure Al layer and a composite layer of Fe and Si which seem to be well mixed within the resolution of the measurement. However, no signal of oxygen contribution is resolved in the oxidised part of the Al layer. The equal EDX counts for Fe and Si translate into a layer composition of ⅓ Fe atoms and ⅔ Si atoms.

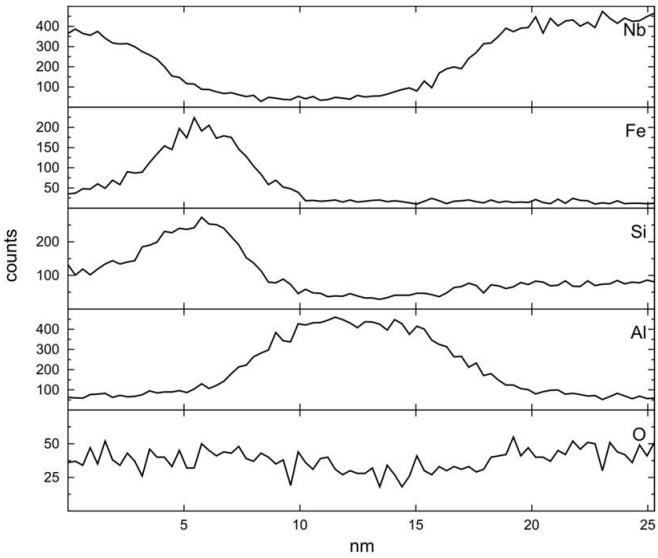

In the following a scanning TEM image of the same barrier is shown together with elemental maps of the barrier region which highlight the distribution of elements at the barrier. A large colour intensity indicates the presence of the specific element.

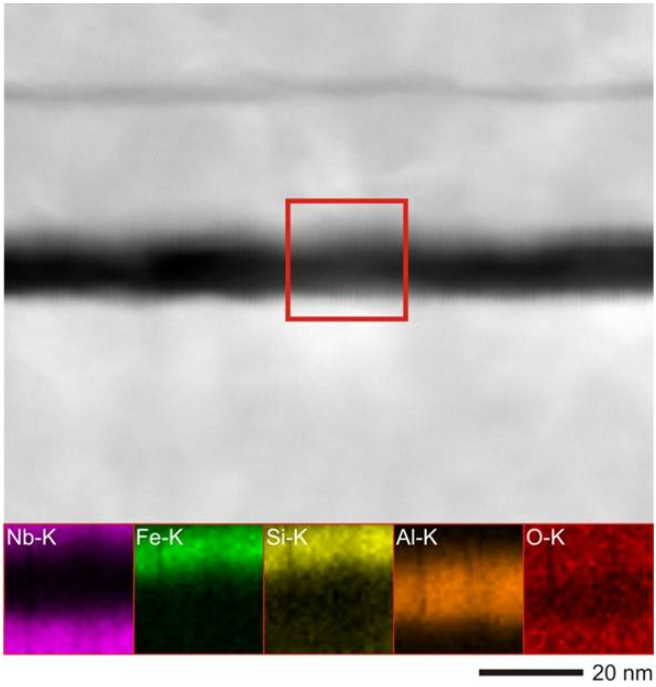
Nb-K
Fe-K
Si-K
Al-K
O-K
20 nm

C Timing Circuit for Combinatorial Sputtering

The deposition of a wedge with a timer controlled sputter source was achieved by an extension of the sputter system. An additional battery controlled timer circuit was triggered by the reference position switch of the sputter chamber arm. The timing unit then activated the targets power supply for an adjustable time period τ. For a rotation frequency of $5\,{}^{1}/_{\mathrm{min}}$ the sample holder was directly under the target position 46 after $\tau = 9.1\,\mathrm{s}$. A shift of the sample holder position at the moment of target shut down could be adjusted considering the relation $70\,{}^{\mathrm{ms}}/_{\mathrm{cm}}$. A schematics of the timing circuit is shown below:

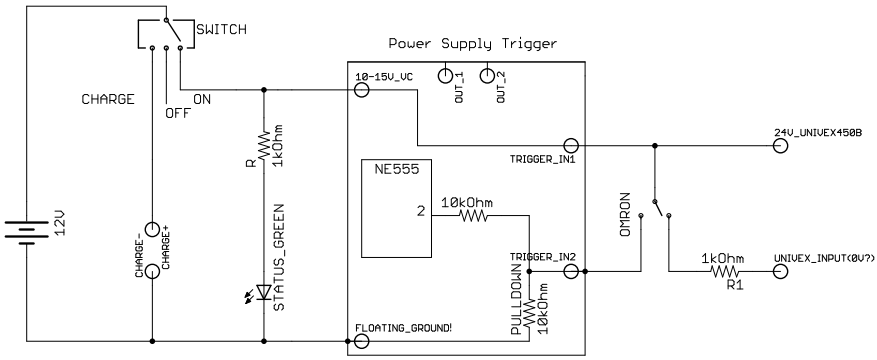

Bibliography

[1] E. Terzioglu and M. R. Beasley, IEEE Trans. Appl. Supercond. **8**, 48 (1998).

[2] L. B. Ioffe, V. B. Geshkenbein, M. V. Feigel'man, A. L. Fauchère, and G. Blatter, Nature **398**, 679 (1999).

[3] G. Blatter, V. B. Geshkenbein, and L. B. Ioffe, Phys. Rev. B **63**, 174511 (2001).

[4] T. Yamashita, K. Tanikawa, S. Takahashi, and S. Maekawa, Phys. Rev. Lett. **95**, 097001 (2005).

[5] A. V. Ustinov and V. K. Kaplunenko, J. Appl. Phys. **94**, 5405 (2003).

[6] O. Mielke, T. Ortlepp, P. Febvre, and F. Uhlmann, IEEE Trans. Appl. Supercond. **19**, 621 (2009).

[7] T. Ortlepp, O. Mielke, J. Kunert, and H. Toepfer, Physica C **470**, 1955 (2010).

[8] A. K. Feofanov et al., Nat. Phys. **6**, 593 (2010).

[9] V. V. Ryazanov et al., Physics Procedia **36**, 35 (2012).

[10] E. Goldobin et al., Appl. Phys. Lett. **102**, 242602 (2013).

[11] M. Maezawa, M. Aoyagi, H. Nakagawa, I. Kurosawa, and S. Takada, Appl. Phys. Lett. **66**, 2134 (1995).

[12] D. G. McDonald, R. L. Peterson, C. Hamilton, R. E. Harris, and R. L. Kautz, IEEE Trans. Electron Devices **27**, 1945 (1980).

[13] M. Tinkham, *Introduction to superconductivity*, Dover publications on physics, Dover Publ, Mineola, NY, 2nd ed. edition, 2004.

[14] K. Likharev, *Dynamics of Josephson Junctions and Circuits*, CRC Press, 1986.

[15] A. Barone and G. Paternò, *Physics and Applications of the Josephson Effect*, Wiley, New York a.o, 1982.

[16] G. Moore, Electronics **38**, 114 (1965).

[17] W. Arden et al., Int. Tech. Roadmap Semicond. , 14 (2010).

[18] A. Thomas, J. Phys. D: Appl. Phys. **46**, 093001 (2013).

[19] R. Waser, R. Dittmann, G. Staikov, and K. Szot, Adv. Mater. **21**, 2632 (2009).

[20] K. Likharev and V. Semenov, IEEE Trans. Appl. Supercond. **1**, 3 (1991).

[21] J. Clarke and F. K. Wilhelm, Nature **453**, 1031 (2008).

[22] J. E. Mooij et al., Science **285**, 1036 (1999).

[23] A. Feofanov, *Experiments on flux qubits with π-shifters*, PhD thesis, KIT Scientific Publishing, 2011.

[24] D. P. DiVincenzo and IBM, ArXivquant-Ph0002077 (2000).

[25] S. Lloyd, Science **273**, 1073 (1996).

[26] H. K. Onnes, Technical Report 120b, 122b, 124c, 1911.

[27] W. Meissner and R. Ochsenfeld, Naturwissenschaften **21**, 787 (1933).

[28] F. London and H. London, Proc. R. Soc. Lond. A **149**, 71 (1935).

[29] J. Bardeen, L. N. Cooper, and J. R. Schrieffer, Phys. Rev. **108**, 1175 (1957).

[30] V. Ginzburg and L. Landau, Zh Eksp Teor Fiz **20**, 1064 (1950).

[31] Suchitra Sebastian (University of Cambridge), Quantum oscillations as a probe of electronic structure (summer school on superconductivity, cargése), 2013.

[32] J. G. Bednorz and K. A. Müller, Z. Physik B - Condensed Matter **64**, 189 (1986).

[33] Y. Kamihara et al., J. Am. Chem. Soc. **128**, 10012 (2006).

[34] Y. Kamihara, T. Watanabe, M. Hirano, and H. Hosono, J. Am. Chem. Soc. **130**, 3296 (2008).

[35] P. J. Hirschfeld, M. M. Korshunov, and I. I. Mazin, Rep. Prog. Phys. **74**, 124508 (2011).

[36] L. Gorkov, Sov Phys JETP **9**, 1364 (1959).

[37] C. Kittel, *Einführung in die Festkörperphysik*, Oldenbourg Wissenschaftsverlag, München, auflage: unveränderte auflage edition, 2013.

[38] I. Giaever, Phys. Rev. Lett. **5**, 147 (1960).

[39] E. L. Wolf, *Principles of Electron Tunneling Spectroscopy: Second Edition*, Oxford University Press, USA, 2 edition, 2012.

[40] Manual: SR830 - DSP lock-in amplifier, 2011.

[41] W. L. McMillan and J. M. Rowell, Pp 561-613 Supercond. Vols 1 2 Parks R Ed N. Y. Marcel Dekker Inc 1969 (1969).

[42] B. D. Josephson, Phys. Lett. **1**, 251 (1962).

[43] V. Ambegaokar and A. Baratoff, Phys. Rev. Lett. **10**, 486 (1963).

[44] P. Seidel and J. Richter, phys. stat. sol. (b) **98**, 189 (1980).

[45] E. Houwman et al., IEEE Trans. Appl. Supercond. **3**, 2170 (1993).

[46] W. C. Stewart, Appl. Phys. Lett. **12**, 277 (2003).

[47] D. E. McCumber, J. Appl. Phys. **39**, 3113 (2003).

[48] C. S. Owen and D. J. Scalapino, Phys. Rev. **164**, 538 (1967).

[49] D. Olaya, P. D. Dresselhaus, and S. P. Benz, IEICE Trans. Electron. **E93.C**, 463 (2010).

[50] A. Gudkov, M. Kupriyanov, and A. Samus', J. Exp. Theor. Phys. **114**, 818 (2012).

[51] V. Shaternik et al., Mater. Res. Express **1**, 026001 (2014).

[52] Y. Xu, D. Ephron, and M. R. Beasley, Phys. Rev. B **52**, 2843 (1995).

[53] J. Wingbermühle, *Transportphänomene in magnetischen Tunnelkontakten unter besonderer Berücksichtigung der Ionenstrahlsputterdeposition*, Forschungszentrum Jülich, 2002.

[54] H. Knauer, J. Richter, and P. Seidel, phys. stat. sol. (a) **44**, 303 (1977).

[55] A. I. Larkin and K. A. Matveev, Zh Eksp Teor Fiz **93**, 1030 (1987).

[56] J. G. Simmons, J. Appl. Phys. **34**, 1793 (1963).

[57] W. F. Brinkman, R. C. Dynes, and J. M. Rowell, J. Appl. Phys. **41**, 1915 (1970).

[58] L. I. Glazman and K. A. Matveev, Zh Eksp Teor Fiz **94**, 343 (1988).

[59] C. H. Shang, J. Nowak, R. Jansen, and J. S. Moodera, Phys. Rev. B **58**, R2917 (1998).

[60] N. F. Mott, *Electronic processes in non-crystalline materials*, Clarendon Press„ Oxford :, 2d ed. edition, 1979.

[61] A. L. Efros and B. I. Shklovskii, J. Phys. C: Solid State Phys. **8**, L49 (1975).

[62] L. N. Bulaevskiĭ, V. V. Kuziĭ, and A. A. Sobyanin, JETP Lett. **25**, 290 (1977).

[63] T. S. Khaire, M. A. Khasawneh, W. P. Pratt, and N. O. Birge, Phys. Rev. Lett. **104**, 137002 (2010).

[64] L. Bergmann, C. Schaefer, and R. Kassing, *Lehrbuch der Experimentalphysik: Band 6 Festkörper*, Gruyter, Berlin, 2., überarb. a. edition, 2005.

[65] E. C. Stoner, Proceedings of the Royal Society of London. Series A, Mathematical and Physical Sciences **165**, 372 (1938).

[66] V. V. Ryazanov, V. A. Oboznov, A. V. Veretennikov, and A. Y. Rusanov, Phys. Rev. B **65**, 020501 (2001).

[67] S. M. Frolov, D. J. Van Harlingen, V. A. Oboznov, V. V. Bolginov, and V. V. Ryazanov, Phys. Rev. B **70**, 144505 (2004).

[68] D. A. Wollman, D. J. Van Harlingen, J. Giapintzakis, and D. M. Ginsberg, Phys. Rev. Lett. **74**, 797 (1995).

[69] S. M. Frolov, D. J. Van Harlingen, V. V. Bolginov, V. A. Oboznov, and V. V. Ryazanov, Phys. Rev. B **74**, 020503 (2006).

[70] M. Weides et al., Supercond. Sci. Technol. **23**, 095007 (2010).

[71] O. Mielke, T. Ortlepp, B. Dimov, and F. H. Uhlmann, J. Phys. Conf. Ser. **97**, 012196 (2008).

[72] A. I. Buzdin, Rev. Mod. Phys. **77**, 935 (2005).

[73] A. F. Andreev, Zh Eksperim Teor Fiz **Vol: 46**, 1823 (1964).

[74] C. W. J. Beenakker, Phys. Rev. B **46**, 12841 (1992).

[75] R. J. Soulen et al., Science **282**, 85 (1998).

[76] P. Fulde and R. A. Ferrell, Phys. Rev. **135**, A550 (1964).

[77] A. I. Larkin and Y. N. Ovchinniko, Sov. Phys. JETP **20**, 762 (1965), [Zh. Eksp. Teor. Fiz. **47**, 1136 (1964)].

[78] E. A. Demler, G. B. Arnold, and M. R. Beasley, Phys. Rev. B **55**, 15174 (1997).

[79] A. Buzdin, B. Bujicic, M. Y. Kupriyanov, and D. Parsons, JETP Lett. **74**, 124 (1992), Zh. Eksp. Teor. Fiz. 101,231-240 (January 1992).

[80] A. I. Buzdin, L. N. Bulaevskii, and S. V. Panyukov, JETP Lett **35**, 178 (1982).

[81] A. I. Buzdin and M. Y. Kupriyanov, JETP Lett **53**, 321 (1991).

[82] Y. S. Barash and I. V. Bobkova, Phys. Rev. B **65**, 144502 (2002).

[83] M. Fogelström, Phys. Rev. B **62**, 11812 (2000).

[84] O. Vávra et al., Phys. Rev. B **74**, 020502 (2006).

[85] E. Goldobin, A. Sterck, T. Gaber, D. Koelle, and R. Kleiner, Phys. Rev. Lett. **92**, 057005 (2004).

[86] D. A. Wollman, D. J. Van Harlingen, W. C. Lee, D. M. Ginsberg, and A. J. Leggett, Phys. Rev. Lett. **71**, 2134 (1993).

[87] D. J. Van Harlingen, Rev. Mod. Phys. **67**, 515 (1995).

[88] V. V. Ryazanov et al., Phys. Rev. Lett. **86**, 2427 (2001).

[89] T. Kontos et al., Phys. Rev. Lett. **89**, 137007 (2002).

[90] S. Piano, J. W. Robinson, G. Burnell, and M. G. Blamire, Eur. Phys. J. B **58**, 123 (2007).

[91] J. W. A. Robinson, S. Piano, G. Burnell, C. Bell, and M. G. Blamire, Phys. Rev. Lett. **97**, 177003 (2006).

[92] Y. Blum, A. Tsukernik, M. Karpovski, and A. Palevski, Phys. Rev. Lett. **89**, 187004 (2002).

[93] A. A. Bannykh et al., Phys. Rev. B **79**, 054501 (2009).

[94] V. A. Oboznov, V. V. Bol'ginov, A. K. Feofanov, V. V. Ryazanov, and A. I. Buzdin, Phys. Rev. Lett. **96**, 197003 (2006).

[95] M. Weides et al., Appl. Phys. Lett. **89**, 122511 (2006).

[96] T. S. Khaire, W. P. Pratt, and N. O. Birge, Phys. Rev. B **79**, 094523 (2009).

[97] G. Wild, C. Probst, A. Marx, and R. Gross, Eur. Phys. J. B **78**, 509 (2010).

[98] F. Born et al., Phys. Rev. B **74**, 140501 (2006).

[99] D. W. Umrath and u. A., Grundlagen der vakuumtechnik, 1997.

[100] R. E. Joynson, C. A. Neugebauer, and J. R. Rairden, J. Vac. Sci. Technol. **4**, 171 (1967).

[101] Y. Chiou, Thin Solid Films **8**, R37 (1971).

[102] T. Imamura and S. Hasuo, J. Appl. Phys. **66**, 2173 (1989).

[103] T. Imamura and S. Hasuo, Appl. Phys. Lett. **55**, 2550 (1989).

[104] J. Brentano, Proc. Phys. Soc. London **37**, 184 (1924).

[105] W. L. Bragg, Proc. Camb. Philos. Soc. **17**, 43 (1913).

[106] N. Ruppelt et al., Appl. Phys. A **116**, 229 (2014).

[107] K. Kennedy, T. Stefansky, G. Davy, V. F. Zackay, and E. R. Parker, J. Appl. Phys. **36**, 3808 (1965).

[108] R. B. van Dover, L. F. Schneemeyer, and R. M. Fleming, Nature **392**, 162 (1998).

[109] J. R. Dahn et al., Chem. Mater. **14**, 3519 (2002).

[110] W. Schroen, J. Appl. Phys. **39**, 2671 (1968).

[111] J. Matisoo, Proc. IEEE **55**, 172 (1967).

[112] R. B. Laibowitz, Appl. Phys. Lett. **20**, 254 (1972).

[113] M. Gurvitch, Appl. Phys. Lett. **42**, 472 (1983).

[114] H. A. Huggins and M. Gurvitch, J. Appl. Phys. **57**, 2103 (1985).

[115] S. Morohashi and S. Hasuo, J. Appl. Phys. **61**, 4835 (1987).

[116] C. C. Chang, M. Gurvitch, D. M. Hwang, and C. W. Blonder, J. Appl. Phys. **61**, 5089 (1987).

[117] T. Imamura, T. Shiota, and S. Hasuo, IEEE Trans. Appl. Supercond. **2**, 1 (1992).

[118] T. Imamura and S. Hasuo, Appl. Phys. Lett. **58**, 645 (1991).

[119] H. Kohlstedt, F. König, P. Henne, N. Thyssen, and P. Caputo, J. Appl. Phys. **80**, 5512 (1996).

[120] J. Kwo, Appl. Phys. Lett. **40**, 675 (1982).

[121] J. Kwo and M. Gurvitch, in *Advances in Cryogenic Engineering*, Vol 30, page 509, New York, 1984.

[122] A. Kleinsasser, R. Miller, and W. Mallison, IEEE Trans. Appl. Supercond. **5**, 26 (1995).

[123] T. Lehnert, K. Schuster, and K. H. Gundlach, Appl. Phys. Lett. **65**, 112 (1994).

[124] S. K. Tolpygo et al., IEEE Trans. Appl. Supercond. **17**, 946 (2007).

[125] D. Yohannes et al., IEEE Trans. Appl. Supercond. **15**, 90 (2005).

[126] F. Schmidl, M. Siegel, P. Seidel, and H.-J. Köhler, phys. stat. sol. (a) **97**, K87 (1986).

[127] P. Bradley, W. Ruby, D. Hebert, and T. Van Duzer, J. Appl. Phys. **66**, 5872 (1989).

[128] H. Kroger et al., IEEE Trans. Magn. **21**, 870 (1985).

[129] P. Lobotka, I. Vávra, š. Gaži, A. Plecenik, and J. Dérer, J. Low Temp. Phys. **106**, 381 (1997).

[130] H.-J. Köhler et al., phys. stat. sol. (a) **67**, 497 (1981).

[131] L. Smith, J. Thaxter, D. Jillie, and H. Kroger, IEEE Trans. Magn. **18**, 1571 (1982).

[132] F. Stromberg, S. Bedanta, C. Antoniak, W. Keune, and H. Wende, J. Phys. Condens. Matter **20**, 425205 (2008).

[133] A. V. Dvurechenskii, V. A. Dravin, and A. I. Yakimov, Phys. Status Solidi A **113**, 519 (1989).

[134] L. J. Van der Pauw, Philips Tech. Rev. **vol. 20**, 220 (1958).

[135] N. Ruppelt et al., Appl. Phys. Lett. **106**, 022602 (2015).

[136] T. I. Larkin et al., Appl. Phys. Lett. **100**, 222601 (2012).

[137] I. Vernik et al., IEEE Trans. Appl. Supercond. **23**, 1701208 (2013).

[138] S. V. Bakurskiy et al., Appl. Phys. Lett. **102**, 192603 (2013).

[139] S. V. Bakurskiy, N. V. Klenov, I. I. Soloviev, M. Y. Kupriyanov, and A. A. Golubov, Phys. Rev. B **88**, 144519 (2013).

[140] M. Kupriyanov, A. Brinkman, A. Golubov, M. Siegel, and H. Rogalla, Physica C: Superconductivity **326–327**, 16 (1999).

[141] D. Cassel et al., Phys. C Supercond. **350**, 276 (2001).

[142] V. V. Bol'ginov, V. S. Stolyarov, D. S. Sobanin, A. L. Karpovich, and V. V. Ryazanov, JETP Lett. **95**, 366 (2012).

[143] D. M. Heim et al., ArXiv13100567v2 Cond-Matsupr-Con (2014).

[144] M. Weides et al., Appl. Phys. A **89**, 613 (2007).

[145] M. Kemmler et al., Phys. Rev. B **81**, 054522 (2010).

[146] A. Barone, W. J. Johnson, and R. Vaglio, J. Appl. Phys. **46**, 3628 (1975).